EVALUATION OF THE RELATIONSHIP BETWEEN PHARMACOKINETICS AND TUMOR ACCUMULATION OF LIPOSOMAL DOXORUBICIN

by
Charlene M. Dawidczyk

A dissertation submitted to Johns Hopkins University in conformity with the requirements for the degree of Doctor of Philosophy

Baltimore, Maryland

August, 2015

ABSTRACT

The Enhanced Permeability and Retention (EPR) effect is widely known to allow for enhanced delivery of nanoparticles to tumors. This has been harnessed for delivery of chemotherapeutics to tumors in multiple FDA approved nanomedicines, including DOXIL®, a doxorubicin-loaded liposome. Nanomedicines enable the modulation of drug delivery parameters to tailor the pharmacokinetics. In this project, we quantitatively evaluate the EPR effect by analysis and comparison of the pharmacokinetics of DOXIL-like liposomes in tumor-bearing and tumor-free mice. Additionally, tumor accumulation is evaluated. We have modeled this system using a 2-compartment model for tumor-free mice and a 3-compartment model for tumor-bearing mice. This allows us to fit the model to our data in order to determine rate constants for liposomal distribution. The majority of data is compared with LS 174T colon adenocarcenoma cells with selective comparison to MDA-MB-231 breast adenocarcinoma and Capan-1 pancreatic adenocarcinoma. It is seen that LS 174T xenografts have the highest tumor accumulation, 20x higher at 24 h than Capan-1 xenografts.

Next, we evaluate the impact of altering a nanomedicine's physicochemical properties on the nanomedicine's pharmacokinetics and tumor accumulation. These predictions might be used to guide future development of nanomedicines.

Doing this, we find that increasing the nanomedicine's evasion of the mononuclear phagocyte system (MPS) will realize the highest increase the tumor accumulation at long time points.

Finally, we evaluate encapsulation of a near-infrared (NIR) imaging agent within liposomes for semi-quantitative evaluation of a liposomal platform. We examine liposome distribution and tumor accumulation over time in mice containing LS 174T subcutaneous xenografts and compare this data with the quantitative data we have gained from analogous doxorubicin-loaded liposomes. We find that this platform could be used for a more expedient and efficient nanoparticle evaluation for more expedient feedback to assist with design of nanomedicines.

ACKNOWLEDGEMENTS

I would like to thank my PhD advisor, Peter Searson, for his guidance and support throughout my time at Johns Hopkins University. From him, I have learned an immeasurable amount about experimental design, problem solving, and presentation of work and ideas. I am extremely fortunate to count him as a mentor.

I would also like to thank the staff members of the Department of Materials Science and Engineering and the Institute for NanoBioTechnology for their support, specifically Jeanine Majewski, Marge Weaver, Dot Reagle, Ada Simari, Ashanti Edwards and Mary Spiro. Additionally, I am grateful to my committee members: Martin Pomper, Hai-Quan Mao, Feilim MacGabhan, and Shawn Lupold.

My friends, especially members of the Searson research group, have provided insight, brainstorming sessions, and excellent collaborations. Thank you for this and for making my time in Baltimore genuinely one of my happiest.

To my family, thank you for inspiring me to achieve my best. My mom, Jenna, has gone above and beyond to encourage me to maximize my achievements. My mom and grandparents have believed in me for longer than I can remember. My brothers, Greydon and Dalton, have always been interested in my research and always know

how to make me laugh. To my husband, Tom, thank you for being there every step of the way in my time at Hopkins, for helping me through my defeats and for celebrating my victories. Thank you for motivating me to constantly learn more and for remaining unwavering in your confidence in me.

CONTENTS

LIST OF TABLES

LIST OF FIGURES

Chapter 1 : Introduction to Nanomedicines

1.1 Nanomedicines for Cancer Therapy

Cytotoxic small molecules such as alkylating agents (e.g. cisplatin), anti-metabolites (e.g. gemcitabine), anti-microtubule agents (e.g. paclitaxel, vincristine), topoisomerase inhibitors (e.g. topotecan), and cytotoxic inhibitors (e.g. doxorubicin) are involved in drug therapies for cancer. These target and kill highly proliferative cells, consequently they preferentially attack cancers cells. However, it also leads to increased cell death in other highly proliferative cells in bone marrow, the gastrointestinal tract, and hair follicles, resulting in the common side effects of compromised immune system; inflammation and ulceration of the GI tract; and hair loss. Incorporation of these drugs into a larger drug delivery system enables a reduction in rate at which the drug can escape circulation into the surrounding tissues. This provides the ability to reduce unwanted side effects by decoupling the design constraints of the nanomedicines.

Biocompatibility and stability in circulation will be important toward improved nanomedicines; however, an additional key goal in improving drug efficacy is increasing the amount of drug delivered to tumor tissues while minimizing the amount of drug delivered to healthy tissues. To bolster the efficiency of nanomedicines accumulation at the tumor site, extravasation from the vasculature to the tumor is increased with larger sized drugs. These drugs enter the tumor via

enhanced permeability and retention (EPR) effect or a targeting agent is added to the drug to provide active targeting. It is possible to further reduce a drug's toxicity by encapsulating it within a nanomedicines (e.g. liposomes) or by locally activating the drug at the tumor site (a prodrug).

1.1.1 The enhanced permeability and retention (EPR) effect

As solid tumors grow, the formation of new vessels is promoted by the up-regulation of angiogenic factors and the down-regulation of angiogenic inhibitors. Through this process, matrix metalloproteinases (MMPs) degrade basement membrane and extracellular matrix (ECM), and the smooth muscle cells are removed locally. Simultaneously, tumor cell proliferation causes the tumor microenvironment to expand, locally generating compressive forces.[1] These compressive forces lead to the contraction of blood vessels, contributing to an increased resistance to flow. Furthermore, the compressive forces on lymphatic vessels lead to poor lymphatic drainage and increased interstitial fluid pressure. This environment consists of both mechanical and biochemical factors that lead to irregular vasculature architecture, higher resistance to blood flow, poor perfusion, and higher permeability. This is known as the EPR effect and yields leakiness in tumor vasculature that is key for systemic delivery of anticancer drugs to a solid tumor.[2-4]

1.1.2 FDA-approved nanomedicines

The nanomedicines that are currently FDA-approved for treatment of solid tumors have exhibited both benefits and challenges. These allow for high drug loading, increased bioavailability, active targeting, and enhancing drug solubility.[5] However, much of the development of develop drug delivery systems remains empirical and a lack of standardization of pre-clinical studies remains a barrier to fully exploiting advances in nanotechnology and bioengineering for significant improvement in patient survival rates.

Currently, six nanomedicines have been approved by the FDA for treatment of solid tumors (Table 1-1): Brentuximab vedotin and Trastuzumab emtansine, Doxil, DaunoXome, Marqibo, and Abraxane.[5] These fall into three main categories: antibody-drug conjugates (ADCs), liposomes, and protein carriers.

ADCs include Brentuximab vedotin and Trastuzumab emtansine. Conceptually, these may be the simplest nanomedicines with an anticancer drug conjugated to the targeting molecule, an antibody. In each case, the anticancer drug, monomethyl auristan E (MMAE) and mertansine, respectively, is too potent to be used without the addition of a targeting moiety to guide it to the tumor site, consequently reducing the side effects. Brentuximab targets a glycosylated phosphoprotein, CD30, expressed by B cells, including B-cell lymphomas, some leukemias, and melanoma cancer stem cells. [6-8] Trastuzumab targets the human epidermal growth factor

receptor 2 (HER2) that is overexpressed in HER2 positive breast cancer. [9, 10] Each antibody has multiple sites for drug conjugation. MMAE is conjugated to Brentuximab via a valine-citrulline cleavable linker for brentuximab vedotin. For Trastuzumab emtansine, mertansine is conjugated to the Trastuzumab antibody via a covalent linkage that is enzymatically degraded in endosomes following cellular uptake. The small number of ADC's that have achieved FDA approval highlights how difficult is can be to translate even relatively simple nanomedicines to the clinic. [11]

Table 1-1. Summary of FDA-approved nanomedicines for treatment of solid tumors.
Six nanomedicines have currently been approved for treatment of solid tumors including two ADC's (Brentuximab vedotin and Trastuzumab emtansine), three liposomes (Doxil, DaunoXome, and Marqibo), and one protein carrier (Abraxane).

Platform	Class	Drug	d (nm)	Drug / carrier ratio	Key design feature(s)	Problem addressed
Brentuximab vedotin	ADC	monomethyl auristan E	~ 10	≤ 8	valine-citrulline linker cleaved by cathepsin in endosomes	monomethyl auristan E (MMAE) is too toxic to be used alone
Trastuzumab emtansine	ADC	mertansine	~ 10	≤ 8	non-cleavable linker; release of drug by proteolytic degradation of antibody in endosomes	mertansine is too toxic to be used alone
Doxil	liposome	doxorubicin	100	10,000 - 15,000	lipid encapsulation for high drug/carrier ratio, polyethylene glycol coating to evade MPS, crystallization of drug in liposome minimizes escape during circulation	drug toxicity and adverse cardiac side effects
DaunoXome	liposome	daunorubicin	50	~ 10,000	no polyethylene glycol coating, targeted by MPS resulting in slow release into circulation	drug toxicity and adverse cardiac side effects
Marqibo	liposome	vincristine	100	~ 10,000	no polyethylene glycol coating, targeted by MPS resulting in slow release into circulation	drug toxicity and adverse side effects
Abraxane	protein carrier	paclitaxel	130	>10,000	non-specific binding of paclitaxel to albumin	overcomes very low solubility of paclitaxel

FDA-approved liposomal nanomedicines include Doxil, DaunoXome, and Marqibo. A generic equivalent of Doxil was FDA approved in 2013, 3 years after the Doxil patent expired. Doxil encapsulates approximately 10,000 doxorubicin molecules within an approximately 100 nm diameter, pegylated liposome. [12] Encapsulation of the chemotherapeutic minimizes side effects including the cardiotoxicity associated with free doxorubicin. Doxorubicin within the liposomes forms a solid crystal because the concentration is greater than the solubility limit of doxorubicin.[12] Cholesterol is incorporated into the lipid bilayer in order to increase the bilayer cohesiveness and decrease the leakage of doxorubicin from the liposome. This leads to increased stability in circulation, with greater than 98% of circulating doxorubicin remaining within the liposome. [13-15] The coating of polyethylene glycol (PEG) increases the circulation half-time, hence the amount of accumulation in the tumor is increased by the EPR effect. [16, 17] The exact mechanism of uptake and release is not know, but there is evidence to suggest that the liposomes are endocytosed. [18]

The liposomal formulation of daunorubicin is DaunoXome[19-21], and the liposomal form of vincristine is Marqibo[22, 23]. In contrast to Doxil, neither of these liposomal formulations include pegylation.[19, 20, 23] They instead impart a tactic similar to slow infusion where they have promoted uptake by the mononuclear phagocyte system (MPS), allowing drug to be freed from the liposomes and slowly enter circulation.

The final FDA-approved nanomedicines is Abraxane, or nanoparticle albumin bound paclitaxel (or nab-paclitaxel). This consists of lyophilized human serum albumin non-specifically bound to pacitaxel.[24] Paclitaxel is typically administered with the toxic non-ionic solvent Cremophor to overcome the low solubility of paclitaxel; however, this can lead to a wide variety of allergic reactions. Abraxane provides an alternative to over come this solubility issue without the use of Cremophor. Upon entering circulation after injection, Abraxane particles dissociate into unbound paclitaxel or smaller albumin-paclitaxel complexes.[25] This provides a non-toxic platform for the solubilization of paclitaxel due to the abundunce of albumin already in circulation.[24]

1.1.3 The pharmacokinetics of nanomedicines

For each of the FDA-approved nanomedicines, their design is reflected in their pharmacokinetic behavior (Table 1-2). The ADCs, Brentuximab vedotin and Trastuzimab emtansine, have low clearance, 3-4 day elimination half-times, and moderate AUCs. [9, 26-29] The pegylated surface of Doxil facilitates extended evasion of the MPS and minimized uptake into healthy tissue, [14, 30-33] resulting in high AUC, low clearance, a small distribution volume, and a long elimination half-time. [12]

For liposomes that are not pegylated, DaunoXome and Marqibo, the aim is not to evade the MPS, and consequently these feature clearance rates about an order of

magnitude above ADCs and Doxil, along with low distribution volumes and short elimination half times (approximately 10 h). [19-21, 23] In this case, DaunoXome is administered at a higher dose than is Marqibo; this is reflected in a higher AUC for DaunoXome than Marqibo.

Table 1-2. Pharmacokinetics of FDA-approved nanomedicines and corresponding free drugs. Data is from human clinical trials, typically representing the range of mean or median values obrained from different doses. If unit conversion was necessary, an average body surface area of 1.7 m^2, weight of 60 kg, and blood volume of 5 L was used.

Drug	Dose mg^2/m	AUC (mg h/L)	CL (L/h)	V_d (L)	$t_{1/2}$ (h)	Refs
Brentuximab vedotin	90 - 110	3.2 - 4.9	0.071 - 0.075	8.2 - 10.2	106 - 144	[26, 29]
Trastuzumab emtansine	10 - 160	0.6 - 28	0.023 - 0.070	1.7 - 3.5	31 - 98	[9, 27, 28]
Doxil	25 - 80	600 - 4900	0.023 - 0.045	2.1 - 6.4	42 - 90	[14, 30-33]
DaunoXome	10 - 190	17 - 1700	0.40 - 0.94	2.9 - 4.1	2.8 - 8.3	[19-21]
Marqibo	2.0 - 2.25	5 - 15	0.36 - 0.38	2.6 - 2.9	9.6 - 12	[22, 23]
Abraxane	150 - 300	4 - 10	31 - 67	900 - 1700	11 - 26	[34, 35]
Doxorubicin	15 - 72	0.5 - 3.8	25 - 72	250 - 1800	9 - 29	[14, 36-38]
Daunorubicin	40 - 120	1 - 19	110 - 150	200 - 450	9 - 24	[19, 39]
Paclitaxel	170 - 330	6 - 40	15 - 50	160 - 530	7.2 - 7.6	[35]

Abraxane's clearance rate is relatively rapid, approximately two orders of magnitude larger than DaunoXome or Marqibo, but with an elimination half-time similar to DaunoXome and Marqibo, and a large distribution volume. [34, 35] These

pharmacokinetics are actually similar to free paclitaxel and other free drugs: low AUC, high clearance rate, high distribution volume, and short elimination half-time.

It is expected that increasing the elimination half-time will enable increased tumor accumulation via the EPR effect. However, this increased tumor accumulation may not directly correlate with improved clinical efficacy because other processes such as transport, uptake, drug release, and delivery to the optimum cellular compartment are all downstream of extravasation by the EPR effect.

1.1.4 Tumor accumulation and targeting efficiency

In preclinical studies, a drug's efficacy is determined from the drug's effect on tumor size or from the fraction of animals that survive treatment (Figure 1-1). These parameters are useful for determining the potential therapeutic benefit of a drug delivery system, but the many factors between the administration and the effect of a drug remain largely a black box. One additional parameter that is important for evaluating a drug delivery system's potential is its ability to reach the tumor site. This parameter, tumor accumulation or targeting efficiency, can be analyzed by evaluation of the fraction of the initial dose that reaches the tumor site (%ID). Unfortunately, this parameter is reported relatively rarely in the literature in spite of its importance.

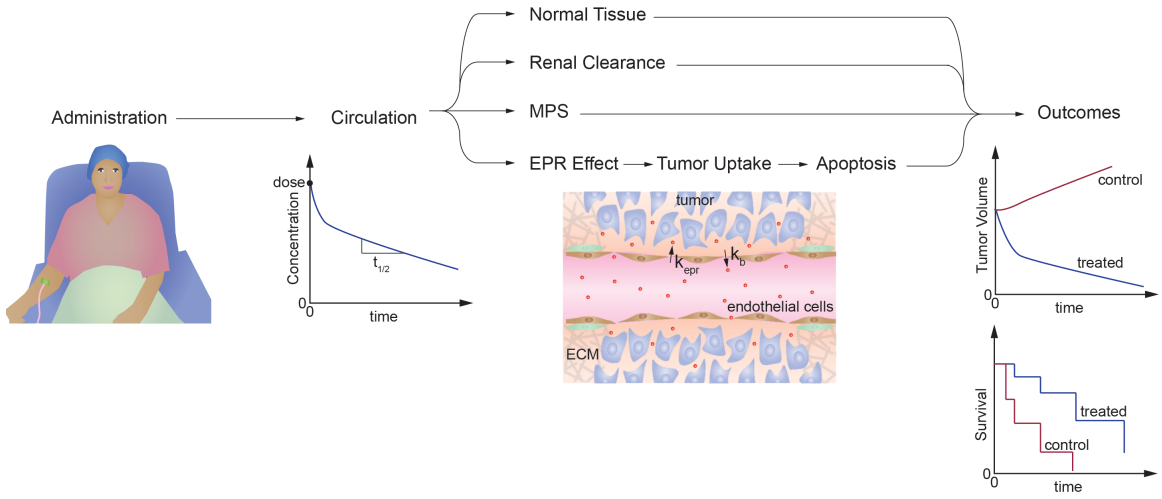

Figure 1-1. Path of drug evaluation.
The outcomes of a drug, namely tumor size and patient survival, are primarily used to evaluate the drug's potential. Unfortunately, the drug's accumulation in the tumor largely remains unknown for many drug delivery systems, making this element along the path to nanoparticle efficacy largely a scientific "black box."

To evaluate the impact of tumor accumulation, we evaluated 73 studies that reported tumor accumulation.[11] For this comparison, only studies that quantitatively report the accumulation of nanoparticles in a tumor were selected. The majority of these studies normalized tumor accumulation to tumor volume by reporting %ID/g or %ID/cc. While these values are important for understanding the concentration of a drug in the tumor, they do not reveal how much of the initial dose actually arrived at its preferred destination, the tumor. These 71 studies encompassed both passive targeting of a nanoparticle and active targeting through the addition of a targeting moiety to the surface of the nanoparticle.

1.1.5 Targeting moieties

The addition of active targeting to a nanoparticle provides a method to minimize uptake in normal tissue while increasing accumulation in the tumor. Strategies to actively target a tumor include the targeting of surface membrane proteins that are frequently upregulated in the cells within a tumor. [40, 41] This strategy is widely used; however, the heterogeneity in tumor cell expression levels and populations can pose difficulties. Standard targeting moieties include antibodies [42-44], antibody fragments [45], aptamers [46, 47], or small molecules (Figure 1-2).

Several factors can impact the efficacy of a targeting moiety added to a nanomedicine. For example, accumulation of any delivery system—active or passive—at the tumor site will be impacted by the concentration in circulation.

Clearance by the MPS or uptake in normal tissue are processes that will decrease the circulating concentration of a drug delivery system and in turn decrease the accumulation in the tumor. The addition of active targeting will provide an additional sink for a drug delivery system because it will be further drawn to its target. These targets are generally expressed in high levels on tumor cells but low levels on other cell types in the vascular system, but because the surface area of the vasculature is so much greater than the tumor, active binding in healthy tissue may still be significant, even if the target is expressed in relatively low levels in healthy tissues.[48]

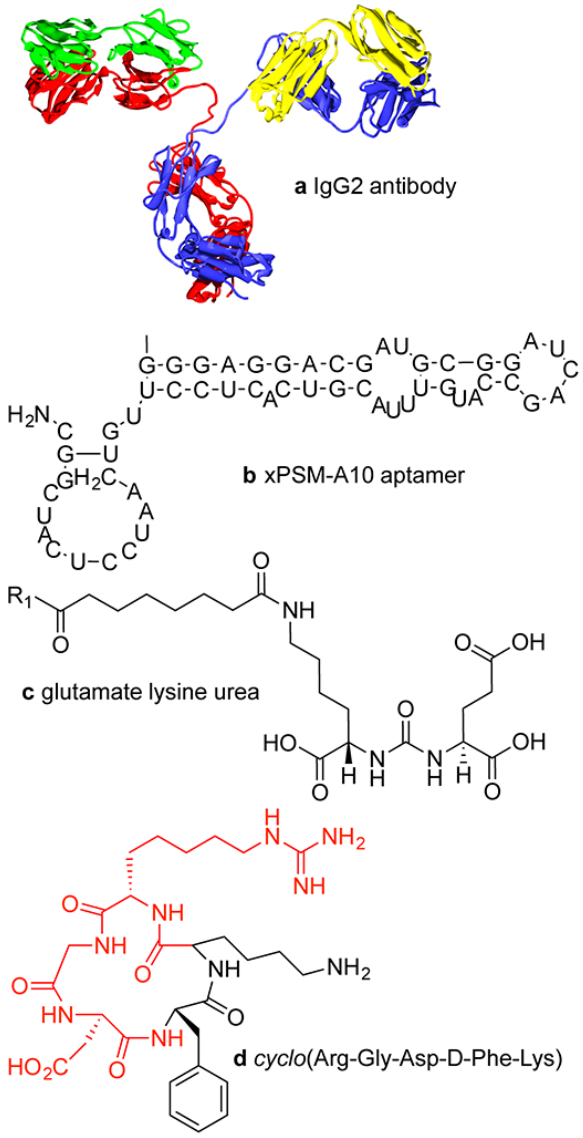

Figure 1-2. Examples of targeting molecules.
(a) Antibodies (approximately 150 kDa or 15 x 5 nm) have two antigen binding sites. (b) xPSM-A-10 (18..5 kDa)is an aptamer with a binding affinity of about 10^{-8} M^{-1} for the extracellular portion of prostate-specific membrane antigen (PSMA) [49] (c) The glutamate lysine urea small molecule targets PSMA (473 Da) [50] (d) The RGD peptide sequence (604 Da) binds to cell surface integrins that are upregulated in many tumor types.

1.1.6 Tumor accumulation of nanomedicines

Pre-clinical trials of nanomedicines are usually designed to assess efficacy by measuring changes in tumor size and/or survival rates following administration in an animal model and not to optimize the design of the delivery platform. Tumor size and/or survival rate data do not provide insight into how modifications to the physico-chemical properties of the delivery platform influence steps in the delivery process (e.g. distribution, clearance, and tumor accumulation). Optimization of the delivery platform is key to minimizing dose and side effects while maintaining efficacy.

To assess the difficulties in comparing delivery platforms and developing design rules we analyzed 74 pre-clinical studies of nanomedicine delivery systems of both passive (Table1-5) and active (Table 1-6) nanomedicine systems. Our initial selection criterion was that studies must report values of tumor accumulation as percent of initial administered dose (%ID) at two or more time points. However, we were only able to find 7 studies that satisfied this criterion and hence broadened the requirements to reported values of tumor accumulation as percent of initial administered dose per gram of tumor (% ID/g) (the importance of these units is discussed below). Despite the importance of pharmacokinetics and tumor accumulation in assessing the efficiency of delivery systems, very few pre-clinical studies report quantitative results that can be used to develop design rules for

nanomedicines. Analysis of these pre-clinical studies highlights the need for guidelines to improve the overall impact of research in this field.

In general, nanomedicines accumulation in a tumor tends to increase immediately after injection followed by decreasing at later times.[11] For example, radiolabeled liposomes increased in the tumor over the first 24 h to 11.3 %ID/g followed by a decrease to 6.1 %ID/g at 72 h.[51] Quantum dot tumor accumulation similarly increased to 13 %ID/g over the first 24 h and then dropped to 11 %ID/g at 42 h.[52] However, this trend is not realized across the board. Pegylated micelles were seen to increase to almost 18 %ID/g over the first 6 h, but at 24 h this has decreased to 2 %ID/g.[53] Additionally, the variation in tumor accumulation is often much smaller. Gold nanoparticles with the addition of active targeting via RGD peptide conjugation were seen to reach 3.65 %ID/g within the first hour, but by 24 h post-injection, this had dropped slightly to 1.94 %ID/g.[54]

1.1.7 Variations in experimental protocol

In reviewing the 73 studies where quantitative tumor accumulation was reported (Table 1-5 and 1-6), it became painfully obvious that variations in experimental protocol across the field hindered our ability to make comparisons across the studies (Table 1-4). Typically, each nanomedicine is evaluated for clinical efficacy in its desired application, but the details of this application, and consequently the evaluation often vary. Unfortunately, determination of the impact of a

nanomedicine's physicochemical properties is stunted by our inability to make comparisons across different studies.

Variations that affect this include both inconsistencies in experimental procedure and in reporting of values.[11] These problems and their solutions are discussed briefly in Table 1-3, and in more detail in the following section, *1.2 Suggested Protocol for Nanomedicine Benchmarking*.

In short, it is uncommon to report the total tumor accumulation of a nanomedicines (in %ID or mg). This is compounded by a lack of consistent explanation of the tumor size, making it impossible to calculate this value from the normalized %ID/g. Both values are important and should be given. While %ID/g describes the concentration of the drug in the tumor and is ostensibly a way to account for differences in tumor size, it is considerably more useful if the tumor mass is also reported. For example, a tumor accumulation of 10 %ID/g is 10 % of the initial dose for a 1 g tumor but 1 % of the initial dose for a 0.1 g tumor. These differences are significant in terms of the efficiency of delivery and minimizing unwanted side effects in normal tissue. In some cases tumor characteristics such as tumor diameter or approximate tumor volume are reported, however, these parameters can only be used to estimate the absolute percentage of the initial dose.

Table 1-3. Limitations to pre-clinical studies of nanomedicines that hinder platform assessment.

Problem	Solution
Total tumor accumulation (%ID) is not always reported	Report tumor accumulation as %ID (and %ID/g)
Inconsistent reporting of tumor size/weight	Report tumor size/weight
Inconsistent reporting of dose	Report dose as total number of nanoparticles injectedalong with other parameters such as drug loading, drug concentration (and/or drug amount), and activity of dose (gamma counter)
Inconsistent reporting of physico-chemical properties	Report standard physico-chemical **p**roperties (e.g. size, zeta potential, surface coating, stability under physiological conditions)
Tumor accumulation reported at different time points	Report tumor accumulation at standard time points (e.g. 1 h and 24 h post-injection). Detailed pharmacokinetics (concentration in blood and tumor) at multiple time points is preferred.
Variation in tumor characteristics (type, size, vascularization, etc.)	• Standardize tumor type and size (e.g. C26 or 4T1; 1 cm diameter) • More difficult for active targeting depending on target molecule
Variation in controls used in active targeting	Report control studies for delivery system with no targeting ligand and any differences in physico-chemical properties. Report other control studies as necessary
Variation in animal models (mouse, rat, etc.) and differences in drug concentration compared to humans	Use mouse xenograft model for initial pre-clinical studies
Different detection methods used to assess tumor accumulation	Perform validation using other method(s)

Additionally, the time point of evaluation should be noted. The time of maximum tumor accumulation will likely vary with varied physicochemical platforms, but

introduction of a standardized time point for comparison will bring us closer to direct comparison of platforms. Even with this, variations in tumor model, including tumor type and animal will prevent cross-platform evaluation. To truly facilitate evaluation of the effect of a nanomedicine's physicochemical properties on its ability to target a tumor, a standardized protocol must be introduced.

1.2 Suggested Protocol for Nanomedicine Benchmarking

The ability to compare studies of different drug delivery platforms will accelerate progress in the field and ultimately will increase the value of time and money invested in nanomedicines research. Variations in experimental design has already impacted our ability to make cross-platform comparisons, and this problem will only magnify as time continues without the introduction of a standardized protocol to facilitate the benchmarking of nanomedicines. The following is an examination of variables that will impact the outcome, and consequently the comparison, or platform evaluation, including animal model, tumor size, dose, and the measured variables for physico-chemical properties, pharmacokinetics, and tumor accumulation. This protocol (Table 1-4), proposes a method that could be applied for benchmarking pre-clinical studies of drug delivery platforms and is discussed in more detail in the following pages.

Table 1-4. Protocol for benchmarking nanomedicines for the treatment of solid tumors.
Standardization of experimental procedures and corresponding reporting metrics will enable direct comparison and contribute to the development of design rules that will accelerate progress in the field.

	Guideline	Reporting
Animal model	LS 174T subcutaneous xenografts grown to 8-10 mm in athymic nu/nu mouse	weight (g), diameter (mm)
Physicochemical properties	size, shape, composition, surface chemistry, zeta potential collected	diameter (nm), shape, composition, surface chemistry, zeta potential
Dose	10^{13} NP	number of NP
Pharmacokinetics	6, 24, 48 h	% ID, mg of drug
Tumor accumulation	6, 24, 48 h	% ID, % ID/g

This protocol calls for quantitative measurement of the concentration of the drug delivery system in blood and the tumor in athymic Nu/Nu mice with subcutaneously xenografted LS 174T cells approximately 8-10 mm in diameter. These measurements should be taken at a minimum of three time points (6 h, 24 h, and 48 h post-injection). Tumor accumulation should be reported as both %ID and %ID/g. The dose administered to the mice should be 10^{13} particles per mouse with 7 mice to be used per time point. By enacting this protocol across pre-clinical trials of nanomedicines, it will be possible to compare the impact of altering physico-chemical properties on the deliverability of the nanomedicines.

1.2.1 Evaluation of animal model for establishing tumor uptake

Rodents are often used in cancer research for therapy development, carcinogen identification, and to evaluate tumor growth and metastasis mechanism. In particular, there are models of primary tumors for most organs in mice, including human tumor xenografts in immunocompromised mice, genetically engineered mice (GEM), and environmentally-induced tumors in mice.[55, 56] Difficulties using mice for this application will include their low total blood volume, approximately 2 mL, that makes it problematic to extract sufficiently large blood samples from a single animal at multiple time points; however, one main benefit of mice is their relative inexpensive cost, making them ideal for benchmarking across laboratories.

The state-of the-art in animal models currently is GEM. Unfortunately, these are quite expensive, technically challenging, and time consuming. They are and will continue to be important for recapitulation of many aspects of the tumor microenvironment; however, they are not ideal for this type of cross-laboratory benchmarking. For this application, it is important to have a relatively straightforward, inexpensive, and quick option. In spite of their shortcomings, subcutaneous xenografts with immortalized cell lines fill this need and should be used.

In terms of cell line for the xenograft, one of the biggest hurdles in nanomedicines benchmarking is the wide variety of cell lines currently used. Of 68 studies of

quantitative tumor accumulation in mouse xenografts, 35 different cell lines were used to form the xenografts.[11] Commonly used cell lines included C26, 4T1, KB, and LS 174T. C26 colon carcinoma cells are also known to induce cachexia in mice, reducing body mass by as much as 20%.[57] This will introduce additional levels in variation in experiments, making C26 not suitable for benchmarking. KB cell lines are widely used in cancer research; however, this cell line has been contaminated by HeLa cells[58] and are no longer suitable for benchmarking. 4T1 is a highly invasive animal breast cancer model that is used both in subcutaneous and orthotopic xenografts that readily metastasize.[59, 60] While this is excellent for physiologic relevance, it poses significant problems toward the quantification of tumor accumulation, making this also unsuitable for benchmarking. LS174T human colorectal adenocarcinoma cell lines grow readily in nude mice and have been used previously in studies of the EPR effect, making this cell line suitable for cross-platform benchmarking.[61]

The final aspect of the mouse model to consider is the size of the subcutaneous LS 174T xenografts. It is important that these grow large enough that they are well vascularized (≥ 1 mm^3)[62] yet not so large that a necrotic core compromises the result. A tumor's ability to self-vascularize will impact the point that it reaches necrosis. For this experiment, LS 174T subcutaneous xenografts should be approximately 0.2 g in weight, about 8-10 mm in diameter. The mass of the tumor should be documented and reported.

1.2.2 Physicochemical properties of the nanomedicines

It is critical to establish the physic-chemical properties that must be reported since the goal of this is to elucidate the relationship between these properties and a drug delivery platform's ability to accumulate in a tumor. Physico-chemical evaluation should include information on nanomedicines size, shape, surface chemistry, and aggregation state.[63-65] These parameters are all known to influence pharmacokinetics, uptake, and trafficking of nanoparticles.[66-71]

1.2.3 Nanomedicine dose

Standardization of dose for pre-clinical platforms is quite difficult, in large part because of inconsistencies in standard practices for dose reporting metrics for different types of nanomedicines. Dose may be based on the amount of drug administered (e.g. weight of drug per body weight or surface area) or may be reported as the number of nanoparticles administered. Rarely is the drug loaded to the nanoparticle at a 1:1 ratio, so information on drug loading (number of drug molecules per nanoparticle carrier) is important but often unmentioned. Furthermore, radio-labeling is a common method for imaging and determination of biodistribution. In fact, this was the predominate method used for quantification of tumor accumulation in our recent metastudy.[11] However, data from this are truly only useful for benchmarking if there is a quantitative calibration between

radioactivity units (e.g. Curies or Bequerels) to dose as absolute amount of nanomedicines.

In analyzing the dose used for quantitative studies of tumor accumulation,[11] the range of dose was quite large (10^{11} – 10^{16} particles/mouse) but most were in the middle, around 10^{13} particles/mouse. Normalized to body weight, this dose is within the range of doses of FDA-approved nanomedicines for humans. Consequently, a dose of 10^{13} particles/mouse should be used and reported both as number of particles, mass of drug, and mass of drug normalized to the mass of animal.

1.2.4 Evaluation of pharmacokinetics and tumor accumulation

Pre-clinical trials of nanomedicines sometimes include pharmacokinetics and biodistribution properties of the nanomedicine. The clearance rate, area under the curve, distribution volume, and elimination half-time are pharmacokinetic parameters that will provide insight into the nanoparticles stability in circulation, uptake in healthy tissues, and propensity for clearance by the kidneys and the MPS. Inclusion of full biodistribution, including accumulation in organs such as liver and spleen, will provide further information with regard to nanoparticle toxicity.

Comprehensive biodistribution and pharmacokinetic curves are immensely valuble but time consuming and expensive, and therefore unrealistic for benchmarking

experiments. Tumor accumulation is one parameter that, while not widely reported, combines aspects of pharmacokinetics with extravasation by the EPR effect. This makes it, along with concentration in blood, an ideal parameter for benchmarking.

Time points of measurements should be minimized to minimize cost and maximize accessibility of benchmarking experiments; however it is important to include time points that are relevant for a variety of nanomedicines. Measurements shortly after administration, at 6 h, will provide insight for systems where maintenance of circulating concentration is not required, for example imaging applications. Measurements at 24 h will allow for insight at a slightly later time point when the concentration in circulation will have slightly dropped. Finally a 48 h time point will allow for examination of tumor accumulation at a time when circulating drug will be quite low, resulting in a concentration gradient that will drive unbound particles out of the tumor back into circulation. This will provide information about retention of the nanoparticle in the tumor. Measurements of amount of nanomedicine in circulation and tumor at 6 h, 24 h, and 48 h will therefore provide a large amount of insight into the nanoparticle behavior.

1.2.5 Protocol for pre-clinical nanomedicine benchmarking

Animal model. 4-6 week old immunodeficient, athymic Nu/Nu female mice are maintained according to federal guidelines, including the Principles of Laboratory

Animal Care in addition to regulations of the institution's Committee on the Use and Care of Animals, and housed in a specific pathogen-free animal facility.

Tumor preparation. LS 174T human colorectal carcinoma cell line is purchased from the American Type Culture Collection (Manassas, VA) and maintained *in vitro* at 37 ˚C, 5% CO_2 in Eagle's Minimum Essential Medium with 10% fetal bovine serum and 1% penicillin/streptomycin. Cells should not be used above passage 15. Immediately prior to xenograft inoculation in the mice, cells are harvested with trypsin-EDTA solution, washed in PBS, and resuspended at a concentration of 5 x 10^6 cells in a 100 μL solution of 50 % growth media and 50% growth factor reduced Matrigel. Each 100 μL suspension of cells is injected subcutaneously into one flank of each mouse. Tumors are grown to reach a diameter of 8 – 10 mm in diameter, approximately 1.5-2 weeks.

Physico-chemical properties. Average particle size, shape, composition, surface chemistry, and zeta potential should be reported for each drug delivery system.

Drug administration. Dose of injection is 10^{13} nanoparticles and should be injectected in a volume of less than 200 μL into the lateral tail vein of the mouse. Dose should additionally be reported in other relevant metrics to the nanoparticle system (drug/radiolabel loading, total drug administered, etc,)

Biodistribution and tumor accumulation. Nanomedicine concentration in both blood and tumor should be quantitatively evaluated at 6 h, 24 h, and 48 h. Each group should include a minimum of seven mice. Concentration in blood and should be reported as absolute amount %ID and amount (mg). In addition, tumor accumulation should be normalized to the weight of the tumor and reported as %ID/g tumor.

Table 1-5. Quantitative studies of passively targeted nanoparticles.

Nanoparticle Type	Size	Cargo	Composition	Tumor type	Tumor size/ weight	Dose	Targeting Efficiency	Method	Ref
Block copolymer micelles	30 nm	Adriamycin	PEG-P(Asp)	Colon 26 xenografts in mice	100 mm^3	10 mg/kg	4 ± 0.4 %ID/g @ 1 hr, 5 ± 1 %ID/g @ 4 hr, 9.5 ± 1 %ID/g @ 24 hr, 9 ± 0.5 %ID/g @ 48 hr	LSC-1000	[72]
Block copolymer micelles	58 nm	^{111}In	PEG-e-caprolactone-p-SCN-Bn-DTPA-^{111}In	MDA-MB-231 xenografts in female nude mice	150 mm^3	250 mg/kg	9 ± 2 %ID/g @ 48 hr	MicroSPECT, CT, gamma counter	[73]
Carbon nanotubes	41.6 nm	SWNT	SWNT+C_{18}-PMH-mPEG	4T1 xenografts in Balb/c mice	20-50 mm^3	200µL of 0.35 mg/mL	30 %ID/g @ 100 hr	Raman scattering	[74]
Composite nanodevices	5 nm	Gold	PAA dendrimers + gold nanoparticles, positively charged surface	B16F10 xenografts in male mice, MatLyLu xenografts in mice	500 mm^3	16 mg/kg	2 ± 0.1 %ID/g @ 5 min, 6 ± 0.1 %ID/g @ 1 hr, 6.5 ± 1.5 %ID/g @ 24 hr, 3 ± 0.2 %ID/g @ 96 hr	Neutron irradiation	[75]
Coordination Polymer	100-200 nm	Oxaliplatin, FITC	PIMA-GA-DACH-platinum	4T1 xenografts in mice	50 mm^3	5mg/kg and 15 mg/kg	0.02 %ID/g for 5 mg/kg dose, 0.05 %ID/g for 15 mg/kg dose	ICP-MS	[76]
Core-crosslinked micelles	45.8 nm	Boron	acetal-PEG-b-PLA-MA + polymerizable carborane crosslinker	Colon 26 xenografts in mice	100 mm^3	0.2 mg boron atoms/kg	Crosslinked: 5.4 %ID/g, noncrosslinked: 1.4 %ID/g	ICP-MS	[77]

Core-crosslinked polymeric micelles	24 ± 8 nm	D-glucosamine, NIRF, ^{111}In	Proprietary	A431 xenografts in mice	8-12 mm in diameter	10 µCi/mouse, 1.3 x 10^{12} particles/mouse	2.75 ± 1 %ID/g @ 4 hr, 2.62 ± 0.8 %ID/g @ 24 hr	Gamma counter	[78]
Core-crosslinked polymeric micelles	24 ± 8.9 nm	Triethoxysilane, NIRFSi, ^{111}In	Block copolymer PEG + triethoxysilane hydrophobic block	CT-26 xenografts in female nude mice	8-10 mm in diameter	1 mg/mouse, 195 µCi	8.5 ± 1 %ID/g @ 24 hr, 8.5 ± 2 %ID/g @ 48 hr (SE)	SPECT, NIRF	[79]
Core-crosslinked polymeric micelles	68 ± 7 nm	^{3}H-acetate	mPEG5k + mPEG-b-p(HEMAm-Lac$_n$)	14C xenografts in mice		200 µL of 10 mg/mL micelles	Crosslinked: 5 %ID/g @ 1 hr, 6 %ID/g @ 4 hr, 7 %ID/g @24 hrs, 6 %ID/g @ 48 hr. Non-crosslinked: 3 %ID/g @ 1 hr, 2.5 %ID/g @ 4 hr, 1 %ID/g @ 24 hr, 0 %ID/g @ 48 hr	Gamma counter	[80]
Core-crosslinked polymeric micelles and long-circulating liposomes	70-100 nm	Dexamethasone	DPPC + chol + DSPE-PEG2k	B16F10 xenografts in male mice	100 mm^3	1 x 10^6 cpm	10 %ID/g for micelles, 5 %ID/g for LC-liposomes @ 24 hr and 48 hr	Liquid scintillation counter	[81]
Core-shell nanoparticles	50 nm	Polypyrrole	Core-shell silica and polypyrrole	4T1 xenografts in Balb/c mice	60-70 mm^3	10 mg/kg	5 %ID/g @ 1 hr, 5 %ID/g @ 6 hr, 4 %ID/g @ 24 hr	ICP-AES	[82]
Graphene	50 nm	Iron oxide nanoparticles, ^{125}I	RGO-IONP-PEG	4T1 xenografts in mice	50 mm^3	4 mg/kg	5 %ID/g @ 48 hr	PET	[83]
Graphene	50 nm	HPPH, ^{64}Cu	Graphene-PEG-HPPH	4T1 xenografts in nude mice	100 mm^3	3.7 MBq	3 %ID/g @ 24 hr	PET	[84]

Hybrid nanoparticles	100 ± 11 nm and 210 ± 23 nm	^{125}I	Fe_3O_4 core, poly(PEGMA) brushes	Colon26 xenografts in mice	7 mm in diameter		21 % ID/g for high MW dendrimer, 3 % ID/g for low MW dendrimer @ 24 h	Gamma counter	[85]
Liposomes		^{111}In, DTPA	Pegylated, proprietary	KB xenografts in mice	varied	10-20 µCi	mean: 7.2 ± 6.6 %ID/g @ 24 hr, tumor size dependence: ≤0.1 g, 15.1 ± 10.8 %ID/g, 0.1-1 g, 5.9 ± 2.2 %ID/g, ≥1 g, 3 ± 1.3 %ID/g	Gamma counter	[86]
Liposomes	80 nm	^{188}Re, BMEDA	DSPC + chol + DSPE-PEG2k	orthotopic Fischer344/F98 glioma tumor-bearing rats	50-100 mm^3	14.8 MBq	0.28 ± 0.09 %ID/g @ 1 hr, 0.75 ± 0.08 %ID/g @ 4 hr, 1.95 ± 0.35 %ID/g @ 24 hr, 1.37 ± 0.39 %ID/g @ 48 hr, 1.09 ± 0.08 %ID/g @ 72 hr (SD)	Gamma counter	[87]
Liposomes	80 nm	Iohexol and gadoteridol	DPPC + chol + DSPE-PEG2k	VX2 xenografts in NZ white rabbits	5000-10000 mm^3	1785 mg/kg iohexol, 40 mg/kg gadoteridol	0.7 ± 0.1 %ID @ 24 hr, 0.9 ± 0.3 %ID @ 48 hr, 0.9 ± 0.3 %ID @ 72 hr (SD)	CT quantitative imaging	[88]
Liposomes	83 nm	BMEDA, ^{188}Re, 5-FU	Pegylated, proprietary	CT26-luc xenografts in mice	100 mm^3	2.96 MBq, 100 µL liposomes, 0.44 µmol phospholipid	4.98 ± 0.57 %ID/g @ 1 hr, 5.67 ± 0.46 &ID/g @ 4 hr, 5.40 ± 0.42 %ID/g @ 16 hr, 5.46 ± 0.37 %ID/g @ 24 hr, 3.53 ± 0.26 %ID/g @ 48 hr, 1.98 ± 0.19 %ID/g @ 72 hr (SEM)	Gamma counter	[89]
Liposomes	83 nm	^{188}Re, BMEDA	Pegylated, proprietary	LS-174T xenografts in mice	50-70 mm^3	2.59 MBq, 100 µL liposomes, 0.7 µmol phospholipid	2.61 ± 0.6 %ID/g @ 1 hr, 4.26 ± 0.7 %ID/g @ 4 hr, 11.27 ± 0.99 %ID/g @ 24 hr, 7.05 ± 0.56 %ID/g @ 48 hr, 6.07 ± 0.35 %ID/g @ 72 hr (SE)	Gamma counter	[51]

Liposomes	90 nm	Doxorubicin, ^{186}Re	Doxil	HNSCC xenografts in nude rats	1 g	555 MBq/kg	0.36 ± 0.33 %ID/tumor @ 120 hrs (SD)	Gamma counter, microSPECT, CT	[90]
Liposomes	100 nm	Copper-doxorubicin complex	Doxil	Bilateral Met1 xenografts in mice	≥100 mm^3	6 mg doxorubicin/kg	10 %ID/g	ICP-MS	[91]
Liposomes	100 nm	^{64}Cu	HSPC + chol + DSPE-PEG2k-OMe/6-BAT-PEG-lipid	DMBA-induced tumors in hamsters	2 mm in diameter		3.5 ± 1.4 %ID/cc @ 24 hr	PET	[92]
Liposomes	110 nm	^{177}Lu	DTPA/PEG	Colon 26 xenografts in mice	562 ± 142 mm^3, 20 g	3.7 MBq	0.61 ± 0.32 %ID/g @ 1 hr, 1.53 ± 0.6 %ID/g @ 4 hr, 3.97 ± 1.75 %ID/g @ 24 hr, 4.68 ± 1.55 %ID/g @ 48 hr, 3.23 ± 1.7 %ID/g @ 72 hr (SD)	Gamma counter	[93]
Mesoporous silica nanoparticles	400 nm	^{165}Ho	MCM-41 + ^{165}Ho	A549-luciferase orthotopic injection in mice		150 µCi	4.5 ± 3.9 %ID/g @ 24 hr, 58.8 ± 34.7 %ID/g @ 1 week	Gamma counter	[94]
Micelles	30 nm	β-lapachone	PEG-PLA	A549 orthotopic lung cancer in mice	200 mm^3	30-50 mg/kg	1.8 ± 0.2 %ID/g @ 2 hr, 1.9 ± 0.2 %ID/g @ 24 hr (SE)	IC liquid scintillation counter	[95]
Micelles	43 ± 24 nm	Etoposide, ^{99m}Tc	Polysorbate 20	Dalton's lymphoma xenografts in Balb/c mice	1 cm^3	100 µCi	10.5 ± 2 %ID @ 1 hr, 5.5 ± 2 %ID @ 6 hr, 5 ± 1 %ID @ 24 hr (SD)	Gamma ray spectrometry	[96]
Micelles	100 nm	Thiostrepton	Amphiphilic lipid-PEG	MDA-MB-231 and HepG2 xenografts in mice	0.25 g	1.8 mg thiostrepton/ animal	16 ± 4 %ID @ 4 hr, 35 ± 2 %ID @ 24 hr (SEM)	LC/MS	[97]

Micelles	110 nm	IFF, ^{111}In	PEG-PDLLA	AR42J xenografts in mice	1 cm^3	100 µL of micelle solution	1 %ID/g up to 120 mins	Gamma counter	[98]
Micelles	192 ± 13 nm	Camptothecin	PEG-poly(benzyl aspartate)	C26 xenografts in mice	100 mm^3	2.5 mg/kg	1.3 %ID/g @ 24 hr	HPLC	[99]
Nanoparticles	1.9 nm	Gold	Gold, proprietary	EMT-6 xenografts in mice	5 mm in diameter	0.01 mL/g of 270 mg Au/cm^3	4.2 ± 0.25 %ID/g @ 20 mins, 2.5 ± 0.1 %ID/g @ 1 hr, 3 ± 0.1 %ID/g @ 5.5 hr, 3.2 ± 0.5 %ID/g @ 11 hr, 2.7 ± 0.1 %ID/g @ 24 hr	Graphite furnace atomic absorption	[100]
Nanoparticles	50 nm	Iron oxide	Iron oxide + PEG-poly(4-vinylbenzylphosphonate)	C-26 xenografts in mice	>100 mm^3	84 mg Fe/kg	1 %ID/g @ 5 mins, 5 %ID/g @ 1 hr, 17 %ID/g @ 4 hr, 17 %ID/g @ 24 hr, 15 %ID/g @ 48 hr, 14 %ID/g @ 96 hr	ICP-MS	[101]
Nanorods	13x47 nm	Gold	Gold, PEG	MDA-MB-435 xenografts in mice		20 mg Au/kg	7 %ID/g @ 72 hr	ICP-MS	[102]
Nanorods	24 x 7 nm	Gold	Gold+mPEG-SH	A431 xenografts in mice	8-10 mm in diameter	2 x 10^{11} particles/µL	1.35 ± 0.29 %ID/g @ 24 hr	Neutron activation analysis	[103]
Nanoshells	120 nm	Gold	Colloidal silica + gold + SH-PEG	A431 xenografts in mice	8-10 mm in diameter	2.74 x 10^8 particles/µL	0.118 ± 0.027 %ID/g @ 24 hr	Neutron activation analysis	[103]
Phospholipid microbubbles	1 µm	Doxorubicin	DPPC + DPPG + DPPE-PEG2k	DSL6A xenografts in Lewis rats	5-8 mm in diameter	140 µg doxorubicin	0.9 ± 1 %ID/g	HPLC	[104]

Polyelectrolyte complex micelles	50-80 nm	siRNA	VEGF siRNA-PEG/PEI	PC3 xenografts in female nude mice	50 mm^3	3 nmol siRNA	0.3 ± 0.01 %ID/g @ 4 hr, 0.5 ± 0.1 %ID/g @ 24 hr (SD)	PCR, fluorescence measurements	[105]
Polymeric micelles	30 nm	Aluminum chloride phthalocyanine	NIPAM + N-vinyl-2-pyrrolidone	EMT-6 xenografts in male mice	25 mm^3	2 µmol/kg of drug	1 %ID/g @ 1 hr, 1 %ID/g @ 24 hr, 2 %ID/g @ 48 hr	Fluorescence spectroscopy	[106]
Polymeric micelles	42 nm	Gadolinium	PEG-b-poly(L-lysine)	Colon 26 xenografts in mice	50-100 mm^3	0.05 mmol Gd/kg	6.1 ± 0.3 %ID/g @ 24 hr	ICP	[107]
Quantum dots	14-28 nm	^{64}Cu	CdSe/ZnS + PEG	U87MG xenografts in mice	100 mm^3	25 µg QDs	5 ± 1 %ID/g @ 1 hr, 12.5 ± 5 %ID/g @ 17 hr, 13.5 ± 4 %ID/g @ 24 hr, 11 ± 3 %ID/g @ 42 hr	PET, ICP-MS	[52]
SWNTs	200 nm	$PMHC_{18}$	SWNT-PEG-$PMHC_{18}$	4T1 xenografts in Balb/c mice	50-100 mm^3	200 µL of 0.5 mg/mL solution	17 %ID/g for 100%-2kPEG-$PMHC_{18}$ @ 48 hr	Raman spectroscopy	[108]

Table 1-6. Quantitative studies of actively targeted nanoparticles.

NP Type	Size	Cargo	Targeting	Composition	Dose	Tumor type	Tumor size/weight	Targeting Efficiency	Method	Ref
Graphene	27.0 ± 0.9 nm with Ab	^{64}Cu	aCD105 antibody	PEG	5-10 MBq (= 135-270 µCi)	4T1 xenografts in mice	5-8 mm in diameter	4.5 ± 0.6 %ID/g with Ab, 2.7 ± 0.3 %ID/g blocked, ~2.5% @ 24h (SD)	PET, gamma counter	[109]
Graphene	64 nm	^{111}In	aHER2 (trastuzumab)		10 µg (5 MBq, 135 µCi)	231/H2N xenografts in mice	500 µL	15.0 ± 3.7 %ID/g without blocking, 1.45 ± 0.04 %ID/g with blocking, 0.11 ± 0.04 %ID/g NP-IgG @72h (SD)	Gamma counter	[110]
Graphene	22.3 ± 3.2 nm	^{64}Cu	aCD105 antibody	PEG	5-10 MBq	4T1 xenografts in mice	6-8 mm in diameter	4 .5 ± 0.4 %ID/g RGO-TRC105, 2.5 ± 0.2 %ID/g RGO-TRC105 blocked, 1.6 %ID/g RGO @24h	Gamma counter	[111]
Hollow nanoshells	34.4 nm without Ab; 37.0 nm with Ab	^{111}In	aEGFR C225 Antibody	Gold	10 µCi/mouse ($7.3x10^{10}$ particles/mL in 0.13 mL)	A431 xenografts in mice	4-6 mm in diameter	6.81 ± 2.64 %ID/g C225-HauNS, 4.60 ± 1.31 %ID/g CTRL IgG-HAuNS @ 24h (SD)	Gamma counter	[112]
Hollow nanospheres	43.5 ± 2.3 nm	^{111}In	α-melanocyte-stimulating hormone analog	Gold, pegylated	$2x10^{12}$ particles/mouse (40 µCi/mouse in 0.2mL)	B16/F10 xenografts in mice	4-6 mm in diameter	12.6 ± 3.1 %ID/g targeted, 4.3 ± 1.2 %ID/g nontargeted @ 4 hr (SD)	Gamma counter, microPET	[113]

Hollow nanospheres	45 nm	si-RNA, ^{64}Cu	Folate	Gold, PEG	0.25 µmol SiRNA/kg	HeLa xenografts in mice	<1.2 cm	5.26 ± 1.25 %ID/g F-NP, 1.11 ± 0.5 %ID/g NP CTRL @ 6 hr (SD)	Gamma counter	[114]
Liposomes	~120 nm	^{64}Cu	Somastatin peptide analog TATE TATE-mal to thiol-PEGlipid	DSPE, DSPE-PEG, chol	10 mg lipid/kg	NCI-H727 xenografts in female mice	< 0.5 g	1.7 ± 0.1 %ID/g @ 1h TATE, 2.7 ± 0.2 %ID/g @ 8h TATE 5.1 ± 0.3 %ID/g @ 24h TATE, 5.0 ± 0.4 %ID/g @ 48h TATE, 1.9 ± 0.1 %ID/g @ 1h CTRL, 3.0 ± 0.2 %ID/g @ 8h CTRL 5.9 ± 0.2 %ID/g @ 24h CTRL, 6.2 ± 0.2 %ID/g @ 48h CTRL (SE)	Gamma counter, PET	[115]
Liposomes	110-120 nm	^{111}In	scFv	Pegylated, POPC, DMPE-DTPA, DSPE-mPEG2000, DSPE-mPEG2000-mal	18.5-37 MBq (0.5-1 mCi)	M28 epithelial and VAMT1 sarcomoid xenografts in mice	3-5 mm in diameter	3.24 ± 0.24 %ID/g @ 24h M28, 4.01 ± 0.39 %ID/g @ 48h M28, 0.97 ± 0.48 %ID/g @ 48h M28 CTRL, 3.86 ± 0.23 %ID/g @ 24h VAMT1, 4.69 ± 0.72 %ID/g @ 48h VAMT1, 0.4 ± 0.42 %ID/g @ 48h VAMT CTRL (SD)	Gamma counter	[116]
Liposomes and Micelles	97 ±2 nm; 20 ± 24 nm	^{111}In	Somatostatin analogue tyrosine-3-octreotide	POPC, Lyso-PG, DSPE-PEG200, DMPE-DTPA	12.5 µg liposome/kg rat; <3 µg micelle/kg rat	AR42J xenografts in rats	20-120 mm^3	~2.5 %ID/g @ 1h, 4h, liposome and micelle; ~0.75 %ID/g all blocked	Gamma camera	[117]
Mesoporous Silica	80 nm	Doxorubicin and ^{64}Cu	aCD105 antibody	PEG	5-10 MBq	4T1 xenografts in mice	5-8 mm in diameter	5.4 ± 0.4 %ID/g silica-TRC105, 2.6 ± 0.2 %ID/g silica @5h (SD)	Gamma counter	[118]
Micelles	60 nm and 15 nm	^{111}In	hEGF Fab	PEG-PCL block copolymer	250 mg/kg (5-7 MBq/mouse)	MDA-MB-468 xenografts in female nude mice	5-10 mm in diameter	2.0 %ID/g 15 nm no hEGF, 0.5 %ID/g 15 nm with hEGF, 4.1 %ID/g 60 nm no hEGF, 0.7 %ID/g, 60 nm, with hEGF	Gamma counter	[119]

Micelles	128 ±10 nm	Paclitaxel, ^{125}I	RGD peptide	PLA-PEG	15 mg/kg	MDA-MB-435 xenografts in mice	Tumor weight=a^2b /2 in mg 300 mm^3	3.53 ± 0.14 %ID/g PLA-PEG-RGD, 0.84 ± 0.09 %ID/g PLA-PEG (SD)	Gamma counter	[120]
Micelles	14 nm	Doxorubicin, ^{125}I	Gelatinase binding peptides	DSPE, CTT2-PEG3400-DSPE	200 µg/mouse	OV-90 xenografts in male mice	65-200 mm^2	~14 %ID/g @ 1.5h, 17.6 %ID/g @ 6h, ~2 %ID/g @24h	Gamma counter	[53]
Micelles	23 nm	^{111}In, Cy7dye-like molecules	EphB4-binding peptide	Core-crosslinked, polymeric, proprietary	$1x10^{14}$ micelles/mouse	PC-3M prostate (EHB4+) and A549 lung (EHB4-) xenografts in mice	5-6 mm in diameter	2.87 %ID/g PC3-M, 1.42 %ID/g PC-3M blocked, 1.37 %ID/g A549 @ 24h	Gamma counter,	[121]
Micelles	25 nm	^{111}In	Annexin A5 protein	Core-crosslinked polymeric	$5x10^{13}$ NP/ mouse	EL4 lymphoma and MDA-MB-468 breast xenograft, pretreated with cyclophosphamide and etoposide for apoptosis, in mice	5-6 mm in diameter	8.01 %ID/g pretreated for apoptosis, 3.2 %ID/g untreated @ 48h	Gamma counter	[122]
Micelles	35 nm	^{125}I	Cyclic RGD	PEG-PLA	35 µCi	U87MG xenografts in mice	0.4-0.6 cm in diameter	1.4 ± 0.086 %ID/g not blocked, 0.44 ± 0.087 %ID/g blocked @ 24 hr (SD)	Gamma counter	[123]
Micelles	80 ± 6 nm	Paclitaxel, ^{111}In	Folate	LDP micelles, pegylated	10 mg/kg mouse	KB xenografts in mice	$w^2*l/2$ 500 mm^3	5 ± 0.4 %ID/g @ 5 min NP-folate, 10 ± 2 %ID/g @ 3 day NP-folate, 5 ± 0.5 %ID/g @ 5 min NP-CTRL, 1 ± 0.3 %ID/g @ 3 day NP-CTRL (SD)	Scintillation counter	[124]

Micelles	65 nm	Doxorubicin and ^{64}Cu	cRGD peptide	Block copolymer, H40-P(LG-Hyd-DOX)-6-PEG	5-10 MBq	U87MG xenografts in mice	6-8 mm in diameter	4.1 ± 0.5 %ID/g @ 30 min NP-cRGD, 5.7 ± 1.2 %ID/g @ 4 h NP-cRGD, 3.7 ± 0.8 %ID/g @ 16 h NP-cRGD, 3.1 ± 0.2 %ID/g @ 24 h NP-cRGD, 2.5 %ID/g @ 24 h NP-CTRL (SD)	Gamma counter	[125]
Nano tripods	20 nm	^{64}Cu	cRGD	Gold, PEG, Platinum	200 pmol/kg	U87MG xenografts in mice	150-200 mm^3	7.9 %ID/g Au-PEG-RGD, 2.6% ID/g Au-PEG, 3.8% ID/g blocked (SE)	PET	[126]
Nanoemulsions	120 nm	Aclacinomycin A (ACM)	Folate	DSPE-PEG2k, chol, vitamin E, pegylated	5 mg ACM/kg	KB xenografts in mice, folate deficient diet	~600 mm^3	0.1 %ID/g without folate, 0.2 %ID/g with folate	HPLC	[127]
Nanoparticles	21.7 ± 0.07 nm	^{99m}Tc	Cyclic RGD	Gold	3.7 MBq	C6 xenografts in mice	0.1-0.3 g	3.48 ± 0.21 %ID/g @ 0.5h, 3.65 ± 0.19 %ID/g @ 1h, 2.49 ± 0.13 @ 3h, 1.94 ± 0.13 %ID/g @ 24h, 1.46±0.23 %ID/g @ 1h blocked (SD)	Well-type scintillation detector	[54]
Nanoparticles	85 ± 9 nm	^{111}In	Folate	PEG, gadolinium	10 mg/kg mouse	KB xenografts in mice	0.82 ± 0.2 g	5 %ID/tumor with folate @ 5 h, 7 %ID/tumor with folate @ 8 h, 4 %ID/organ without folate @ 5 hr, 9 %ID/organ without folate @ 8 hr (SD)	Gamma counter	[128]
Nanoparticles	7 nm	Cy5+PEG+^{124}I	cRGD peptide	Silica, pegylated	20 µCi/mouse	M21 xenografts in mice	200 mm^3	1.5 %ID/g with RGDY, 1 %ID/g no RGDY @ 4 hr	Gamma counter	[129]
Nanoparticles	30 nm	siRNA	EPPT peptide	PEG, iron oxide	10 mg/kg Fe	BT-20 xenografts mice	~0.5 cm in diameter	20 %ID/g	Gamma counter	[130]

Nanoparticles	16 mm (TEM), 115 nm (DLS)	^{198}Au	BBN peptide	Gold	100 µL of 3 mg/mL	PC-3 xenografts in mice	~125 mg	0.48 %ID	Scintigraphic radio-counting methods	[131]
Nanoparticles	80 nm		Transferrin	PEG, gold	4.5x10^{11} particles	neuro2A xenografts in mice		2-3 %ID (no difference with and without transferrin) @24h	ICP-MS	[132]
Nanoparticles	20, 200 nm	^{64}Cu, NIR dye	Aptamer to nucleolin	Silica, PEG	30 µCi	4T1 xenografts in mice		14.6 %ID/g NP-Apt, 6.2 %ID/g NP-nonspecific Ctrl (20nm)	PET, gamma counter	[133]
Nanoparticles	54.2 ± 1.9 nm with Ab	^{111}In	aHER2 (trastuzumab)	PEG, gold	10-12 MBq (=650-863 µg Au)	MDA-MB-361 xenografts in mice		1.23 ± 0.20 %ID/g, 2.20 ± 0.23 without Ab, 1.22 ± 0.27 %ID/g blocked @ 48h (SE)	Gamma counter, ICP-MS	[134]
Polymer nanocarriers	10 nm	Dye (DY-670 or DY-676)	RGD and NGR peptides	p(HPMA-co-Ma-GG-DY-750-co-Ma-GG-AP)	2.5 nmol dye/mouse	BxPC3 (poorly leaky) and CT26 (highly leaky) xenografts in mice	~8 mm in diameter	~6 %ID/g CT26 @ 24, 48, 72 h ~3 %ID/g BxPC3 @24, 48, 72 h	FMT and micro-CT	[135]
Quantum Dots	10-20 nm		RGD or RAD peptides	InAs/InP/ZnS QD, pegylated	200 pmol/mouse	U87MG xenografts in mice	200-500 mm^3	10.7 ± 1.5 %ID/g QD-RGD, 2.9 ± 0.3 %ID/g QD-PEG, 4.0 ± 0.5 %ID/g QD-RAD (SD)	IVIS Fluor (semi-quantitative)	[136]
Shell Cross-linked Nanoparticles	20 ± 3 nm	^{64}Cu	Folate	TETA-labeled folate functionalized PAA/PMA shell crosslinked nanoparticles + ^{64}Cu	370-440 kBq (3-5 mg/kg mouse)	KB xenografts in mice	10-100 mg for biodistribution, 0.3-0.6 g for autoradiography	3.4 ± 1.2 %ID/g with folate @ 10 min, 2.3 ± 0.7 %ID/g with folate @ 1 h, 5.9 ± 2.8 %ID/g with folate @ 4 h, 2.9 ± 3.1 %ID/g with folate @ 24 h, 2.2 ± 0.3 %ID/g without folate @ 10 min, 3.2 ± 0.7 %ID/g without folate @ 1 h, 6.0 ± 1.9 %ID/g without folate @ 4 h, 5.6 ± 0.9 %ID/g without folate @ 24 h (SD)	Gamma counter	[137]

SPIO micelles	75 ± 11 nm	^{3}H	cRGD peptide	PEG-PLA copolymer micelle	6 mg Fe/kg mouse	A549 xenografts in mice	200-400 mm^3	1.3 ± 0.3 %ID/g cRGD-SPPM, 0.6 ± 0.3 %ID/g cRGD-free SPPM @ 1 hr (SD)	Liquid scintillation counter	[138]
SPIONS	10 nm bare SPIO, 68 ± 2 nm with cRGD	^{64}Cu, doxorubicin	Cyclo(RGDfC) peptides	SPIONS	5-10 MBq	U87MG xenografts in mice	6-8 mm in diameter ≈ 200 mm^3	5.4 ± 2.1 %ID/g cRGD-SPIO, 2.5%ID/g cRGD-free SPIO @ 24 hr (SD)	PET, gamma counter	[139]
SPIONS	20 nm	^{111}In	aChL6	Dextran, PEG	20-25 µCi	HBT 3477 xenografts in mice	100-350 mm^3	9 %ID/g, 0.5 %ID/g without Ab @ 48h	WBAR, gamma counter	[140]

Chapter 2 : Quantification of the Enhanced Permeability and Retention Effect

2.1 Introduction

The field of nanomedicine has made great strides over the past 60 years (Figure 2-1). Liposomes, spherical vesicles consisting of at least one lipid bilayer, were initially discovered in 1965. [141, 142] Gabizon and Barenholz did a large amount of work optimizing liposomal doxorubicin for treatment of solid tumors.[12] The chemotherapeutic drug doxorubicin is loaded into the liposome with an ammonium sulfate gradient to form an encapsulated doxorubicin crystal precipitate.[15] Only thirty years after initial reports of liposomes, Doxil was FDA-approved in 1995 for AIDS-related Kaposi's sarcoma, with metastatic ovarian carcinoma and multiple myeloma later also approved for Doxil treatment.

Doxil is approximately 100 nm in diameter. Its lipid bilayer is composed of 60 % dual-acyl chain lipids and 40 % cholesterol. The addition of polyethylene glycol (PEG) on the head group of a portion of the lipids facilitates the evasion of the mononuclear phagocyte system (MPS). Modifying the liposome surface to include PEG increases the elimination half-life and consequently the time that the drug is

available for tumor uptake, hence the overall tumor accumulation is increased. [143]

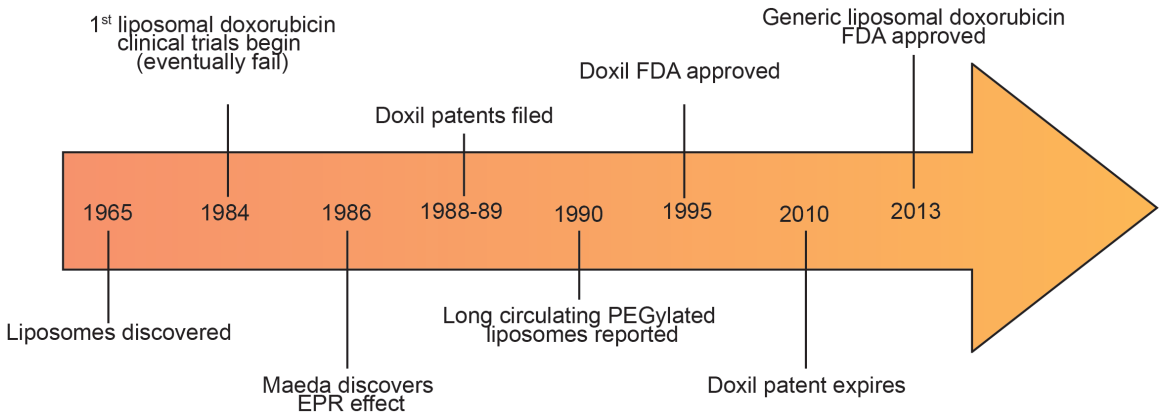

Figure 2-1. Timeline of Doxil creation and FDA-approval.
Liposomes were initially discovered in 1965.[141, 142] Just under 20 years after that, the first liposomal trials began using doxorubicin encapsulated within a liposome. In 1986, Maeda discovered the mechanism of the EPR effect.[4] Pegylation of liposomes for evasion of the MPS was first reported in 1990.[143] Five years after that, Doxil achieved FDA approval and was able to enjoy 15 years on the market prior to its patent expiring. However, a generic was not FDA-approved until 3 years later, in 2013.

The systemic delivery of a drug to a solid tumor involves several steps that occur in series and ultimately determine drug efficacy and survival. Extravasation from circulation at the tumor site is a critical step in the delivery process since it determines tumor accumulation (percentage of initial dose in the tumor, %ID) and yet it effectively remains "back box." Striking evidence in support of this "back box"

argument is that in classic pharmacokinetics, tumor accumulation is bundled into the other clearance pathways for analysis, i.e. the rate constant for clearance (k_{el}) includes tumor accumulation along with clearance by the kidneys, clearance by the mononuclear phagocyte system (MPS), and any other mechanisms. [144]

The accumulation of nanomedicines in a tumor is modulated by the enhanced permeability and retention (EPR) effect. In the tumor, leaky, underdeveloped vasculature enables passively enhanced permeability while underdeveloped lymphatic systems reduce clearance from the tumor, which enables enhanced retention.[4] Combined, these lead to an increase in accumulation of macromolecules and nanomedicines in the tumor.[4]

Encapsulation of doxorubicin within a pegylated liposome increases the drug's elimination half life from about 10 h for free doxorubicin to about 45 h for Doxil.[14] This increased time in circulation provides a longer reservoir with which to feed the tumor. The further benefit of encapsulating the doxorubicin is a decreased cardiotoxicity seen in patients due to the lipids providing a protective boundary between the doxorubicin and the endothelium.[145]

In 2010, the patent on Doxil expired, yet it was not until 2013 before a generic drug received approval. In this gap, there was significant discussion on the reason for this delay, and it was generally believed that a lack of understanding of the interaction between the physico-chemical properties of Doxil and its ability to target

a tumor contributed to the inability to quickly replicate Doxil.[12, 146] Improving our knowledge of the link between the properties of Doxil and their effect on its ability to reach the tumor site will facilitate a greater knowledge of nanoparticle-tumor interactions and the EPR effect. The first step towards accomplishing this is to establish the baseline for Doxil behavior in systems both with and without tumor presence.

In drug development, information about accumulation at the tumor site remains sparse.[11] While some studies do provide this information, they are limited; however, information about a drug's ability to reach the tumor is important to understanding its ability to affect and kill the cells within this tumor. While this information would provide excellent feedback for drug development, it remains largely a "black box".

To shed light on how a nanomedicine accumulates in a tumor, we will focus on a single drug delivery system: pegylated liposomes. While selection of a single platform limits the number of comparisons that we can make in terms of varying physicochemical properties, it maximizes the scope of the project in terms of the number of questions that we can address. The rationale for selecting liposomes is: (1) liposomal doxorubicin (Doxil) is an FDA-approved nanomedicine, (2) liposomes can be functionalized with various moieties, and (3) liposomes can be loaded with other cargo (genes, contrast agent, etc.) for *in vivo* imaging (Chapter 4).[16, 147-156]

In this section, we aim to establish an understanding of how liposomal doxorubicin accumulates in a tumor. To accomplish this, the pharmacokinetics are first evaluated in tumor-free mice to establish a baseline understanding of the nanoparticle's behavior *in vivo*. Then, upon introduction of a subcutaneous tumor both pharmacokinetics and tumor accumulation are evaluated. Further, we apply a pharmacokinetic model of the drug's movement between the vascular and tumor compartments, and we optimize this model to our data in order to determine rate constants that describe the drug's behavior, hence quantifying the effect of the tumor. Finally, we aim to establish and compare tumor accumulation in 3 different tumor types. This will facilitate an understanding of the impact of tumor type on tumor accumulation and nanoparticle efficacy. Establishing this baseline information in Doxil will provide a quantitative foundation for assessing and designing new platforms, and will contribute to more efficient use of resources for research and development.

2.1.1 Doxil physicochemical properties

Doxil is known to consist of spherical vesicles just under 100 nm in diameter.[12] The dual acyl chain, zwitterionic hydrogenated soy phosphatidylcholine lipid makes up 90% w/w of the lipid composition with the remaining 10% w/w from the pegylated dual acyl chain N-(carbonyl-methoxypolyethylene glycol 2000)-1,2-distearoyl-sn-glycero-3-phosphoethanolamine. The methoxy-PEG group on the latter lipid yields a very slightly negative zeta potential.[12] The lipid bilayer is

made of 60% lipids, with the remaining 40% w/w composed of cholesterol to increase liposome cohesion. Doxorubicin is loaded via an ammonium sulfate gradient to form long crystals within the liposome.

2.2 Materials and Methods

2.2.1 Cell culture

All cells were cultured according to the cell culture guidelines put forth in American Type Cell Culture's (ATCC's) corresponding protocols. LS 174T colorectal adenocarcinoma cells were obtained from ATCC. LS 174T cells were grown in Eagle's Minimum Essential Medium (EMEM) (Quality Biological) with 10% fetal bovine serum (FBS) (Life Technologies) and 1% penicillin streptomycin (P/S) (Life Technologies). Capan-1 pancreatic adenocarcinoma cells were purchased from ATCC and grown in Dulbecco's Modified Eagle Medium (DMEM) (Life Technologies) with 20% FBS and 1% P/S. MDA-MB-231 breast adenocarcinoma cells were obtained from ATCC and grown in DMEM with 10% FBS and 1% P/S. Cells were maintained in a humidified incubator at 5% CO_2 and 37°C.

2.2.2 Animal models

All experiments were approved by and performed in accordance with the guidelines and regulations of the Animal Care and Use Committee for Johns Hopkins University. Athymic nu/nu mice 4-6 weeks old were purchased from Charles River.

2.2.3 Xenograft

Approximately 5 million cells were suspended in 100 μL of 50% growth media and 50% growth-factor-reduced Matrigel (Corning). Cell suspensions were maintained on ice until subcutaneous inoculation in the right flank of a mouse. Xenografts were grown to 8-10 mm in diameter or approximately 0.2 g in weight.

2.2.4 Drug administration

Liposomal doxorubicin (Avanti Polar Lipids) was injected at 6 mg/kg via lateral tail vein injection.

2.2.5 Plasma and tumor collection

At 6 time points post injection (5 min, 30 min, 1 h, 6 h, 24 h, 48 h) mice were anesthetized with a lethal dose of isoflurane for sample collection. After the mouse was asleep but its heart was still beating, blood was collected via cardiac puncture and immediately centrifuged to separate and collect the plasma samples. Mice were returned to an isoflurane chamber for at least 2 min to ensure euthanization. Tumors were surgically removed promptly after mice were sacrificed and then homogenized in 300 μL mouse plasma (Innovative Research) for 30 m using a cordless pestle motor (VWR). Cell matter was then removed via centrifugation.

2.2.6 Preparation for HPLC

To plasma samples (100 μL from the mouse blood and then entire amount from the tumor), 1 μL of daunorubicin was added as a standard control and 10 μL of Triton-X was added to burst the liposomes and free the doxorubicin for chemical evaluation. Acetonitrile was then added and vials were vigorously rocked for 10 min. Samples were then centrifuged for 10 min at 8000 rpm and the supernatant was extracted. This supernatant was subsequently dried under flow of argon in a water bath at 37 °C. When the sample appears dry, it is placed in a vacuum chamber for 3 h – overnight to confirm removal of liquid. The sample is then resuspended in 30% methanol, 70% water for running on the HPLC. These samples are run at 1 mL/min using 70% methanol and 30% water with 0.1% formic acid through a C18 BDS Hypersil column. The output from these experiments will be the doxorubicin concentration in blood and the tumor. The workflow for measurement and analysis is outlined in Figure 2-2.

2.2.7 Statistical analysis

Statistical significance was determined using a Student's t-test. *** $P \leq 0.001$, ** $P \leq 0.01$. * $P \leq 0.05$.

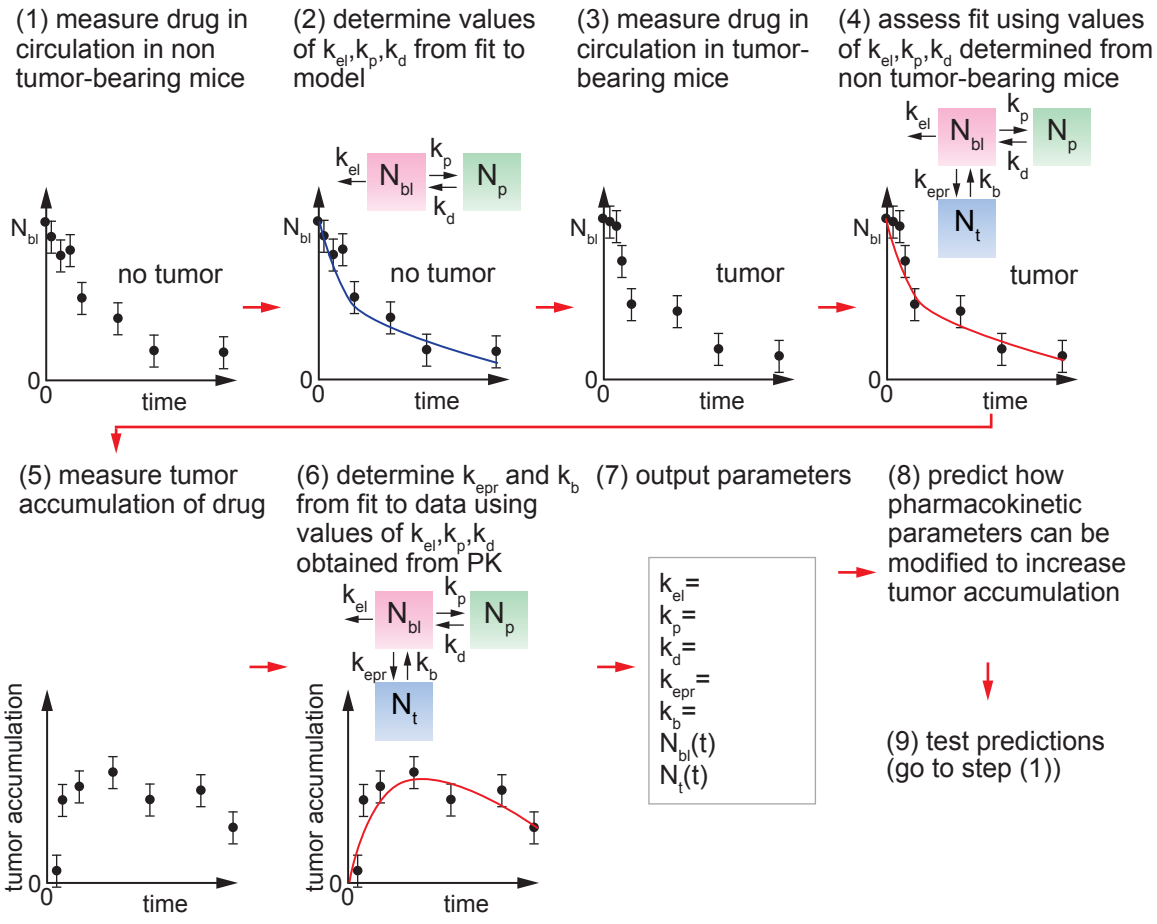

Figure 2-2. Workflow in analysis of tumor accumulation.
(1-2) Data for amount of drug in blood (N_{bl}) in non tumor-bearing mice are fit to obtain values of k_{el}, k_p, and k_d. (3-4) Data for drug concentration in blood in tumor bearing mice are fit using the same values of k_{el}, k_p, and k_d to verify that tumor accumulation does not significantly change the clearance rate. Differences are only expected for very high values of tumor accumulation. If the clearance rate varies significantly, then the data are fit to give a revised value for k_{el}. (5-6) These values of k_{el}, k_p, and k_d are then used to fit to the data for tumor accumulation (N_t) in tumor-bearing mice to obtain values for k_{epr} and k_b. The rate constants for k_{epr} and k_b describe the kinetics of tumor uptake by the EPR effect. (7-9) The values for the rate constants may then used to make quantitative comparisons between experiments or to make predictions of how changing pharmacokinetic parameters will change tumor accumulation.

2.3 Model

The time-dependent concentration of a drug in circulation is often analyzed using a two-compartment pharmacokinetic model, with a central compartment (vasculature and highly perfused tissue) and a peripheral tissue compartment.[157] This model works well when a drug is intraveneously injected and subsequently follows a bi-exponential decay.[157] The first order distribution rate constants between the two compartments, k_p and k_d, in addition to an elimination rate constant, k_{el}, describe the drug behavior (Figure 2-2). The rate constant k_{el} represents all elimination pathways and includes clearance by the kidneys and the mononuclear phagocyte system (MPS).

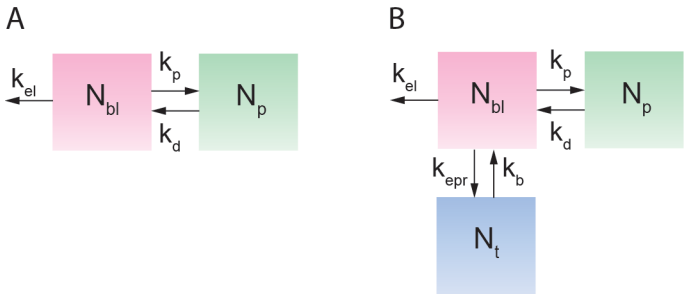

Figure 2-3. Schematic illustrations of pharmacokinetic models.
(a) Two compartment pharmacokinetic model with first order rate constants describing exchange between vascular (blood) compartment and peripheral tissue (k_p and k_d) and elimination (k_{el}). (b) Three compartment model with an additional tumor compartment. To account for exchange into and out of this tumor compartment, the first order rate constants k_{epr} and k_b are defined, respectively.

Evaluation of a mass balance for each compartment yields the following base equations for this system:

$$V_b \frac{dc_b}{dt} = V_p k_d c_p - V_b k_p c_b - V_b k_{el} c_b \qquad \textbf{Equation 2-1}$$

$$V_p \frac{dc_p}{dt} = V_b k_p c_b - V_p k_d c_p \qquad \textbf{Equation 2-2}$$

where V_b is the volume of blood (typically 5-6 L), V_p is the volume of the peripheral compartment, c_b is the concentration in blood, c_p is the concentration in the peripheral compartment, k_p is the rate constant for transport from the blood into the peripheral tissue, k_d is the rate constant for transport from the peripheral tissue back into circulation, and k_{el} is the rate constant for elimination.

These are represented by the second order differential equation:

$$\frac{d^2 c_b}{dt^2} + A\frac{dc_b}{dt} + Bc_b = 0 \qquad \textbf{Equation 2-3}$$

The solutions to equation2-3 is of the form:

$$C_b(t) = Ae^{-\alpha t} + Be^{-\beta t} \qquad \textbf{Equation 2-4}$$

where *A* and *B* describe the y-intercept for the distribution and elimination phases, respectively, and α and β describe the half lives of distribution and elimination, respectively. From mass balance, A+B is equal to the initial dose (at time equals 0). The parameters A, B, α, and β can then be determined by the shape of the curve. By solving the mass balance equations, it is possible to relate these terms to the physiologically relevant term k_{el}, k_p, and k_d:

$$A + B = Dose \qquad \textbf{Equation 2-5}$$

$$k_d = \frac{A\beta + B\alpha}{A + B} \qquad \textbf{Equation 2-6}$$

$$\alpha\beta = k_{el}k_d \qquad \textbf{Equation 2-7}$$

$$\alpha + \beta = k_d + k_{el} + k_p \qquad \textbf{Equation 2-8}$$

In applying pharmacokinetic models to drug delivery to solid tumors, conventional models include accumulation in the tumor in the elimination rate constant. To evaluate tumor accumulation we have developed a three-compartment model with the addition of a tumor compartment (Figure 2-3B) that will allow for quantitative evaluation of the EPR effect on pharmacokinetics. [158]

The rate equations for the three-compartment model (Figure 2-3b) are:

$$V_b \frac{dc_b}{dt} = V_p k_d c_p - V_b k_p c_b + V_t k_b c_t - V_b k_{epr} c_b - V_b k_{el} c_b$$ **Equation 2-9**

$$V_p \frac{dc_p}{dt} = V_b k_p c_b - V_p k_d c_p$$ **Equation 2-10**

$$V_t \frac{dc_t}{dt} = V_b k_{epr} c_b - V_t k_b c_t$$ **Equation 2-11**

where V_t is the tumor volume, c_t is the concentration in the tumor, k_{epr} is the rate constant for transport into the tumor compartment from the blood, and k_b represents transport from the tumor compartment back into circulation. The drug concentration in the blood and the tumor compartments are represented by the third order differential equations:

$$\frac{d^3 c_b}{dt^3} + A\frac{d^2 c_b}{dt^2} + B\frac{dc_b}{dt} + C c_b = 0$$ **Equation 2-12**

$$\frac{d^3 c_t}{dt^3} + A\frac{d^2 c_t}{dt^2} + B\frac{dc_t}{dt} + C c_t = 0$$ **Equation 2-13**

The general solutions to the concentration in blood (Equation 2-14) and in the tumor (Equation 2-15) are of the form:

$$c_b(t) = Ae^{-\alpha t} + Be^{-\beta t} + Ce^{-\gamma t}$$ **Equation 2-14**

$$c_t(t) = Ae^{-\alpha t} + Be^{-\beta t} + Ce^{-\gamma t}$$ **Equation 2-15**

Similarly, the sum of the constants *A*, *B*, and *C* in the blood are constrained to the initial dose of drug, and using the differential equations from the mass balance, we can relate A, B, and C back to the rate constants.

$$A = k_p + k_d + k_{el} + k_{epr} + k_b$$ **Equation 2-16**

$$B = k_b k_p + k_b k_{el} + k_{epr} k_d + k_d k_b + k_d k_{el}$$ **Equation 2-17**

$$C = k_b k_d k_{el}$$ **Equation 2-18**

Further evaluation of this solution yields the complex solutions for α, β, and γ:

$$\alpha = Q - \frac{1}{Q} - \frac{A}{3}$$ **Equation 2-19**

$$\beta = \frac{-\frac{A^2}{9} + \frac{B}{3}}{2Q} - \frac{A}{3} - \frac{Q}{2} - \frac{\sqrt{3}\left(\frac{-\frac{A^2}{9} + \frac{B}{3}}{Q} + Q\right)i}{2}$$ **Equation 2-20**

$$\gamma = \frac{-\frac{A^2}{9}+\frac{B}{3}}{2Q} - \frac{A}{3} - \frac{Q}{2} + \frac{\sqrt{3}\left(\frac{-\frac{A^2}{9}+\frac{B}{3}}{Q}+Q\right)i}{2}$$ **Equation 2-21**

where the term Q is:

$$Q = \left[\frac{AB}{6} - \frac{C}{2} + \sqrt{\left(-\frac{A^2}{9}+\frac{B}{3}\right)^3 + \left(\frac{A^3}{27} - \frac{AB}{6} + \frac{C}{2}\right)^2} - \frac{A^3}{27}\right]^{1/3}$$ **Equation 2-22**

2.3.1 Analysis of *in vivo* data

In order to elucidate rate constants describing drug distribution and tumor accumulation, we first utilize the two-compartment model for tumor-free mice to obtain values for k_p, k_d and k_{el}. It can be assumed that k_p, k_d, and k_{el} remain constant for experiments in tumor-bearing mice on administration of the same drug at the same concentration. Using this assumption, there are two unknown rate constants for tumor bearing mice: k_{epr} and k_b. Fits of experimental data to the mass balance equations were performed using Matlab. The rate constants were determined by an error minimization method. For each data point, the error was determined to be the difference between the experimentally obtained value and the predicted value and was then normalized to the average experimental value for both pharmacokinetic

and tumor accumulation data. The normalized error for all data points, including both pharmacokinetic and tumor accumulation data, was then added together to yield a total normalized error. For iterative values of k_{epr} and k_b, we determined the total normalized error, and the instance of minimum error provides the best fit and yields rate constants to evaluate liposome distribution.

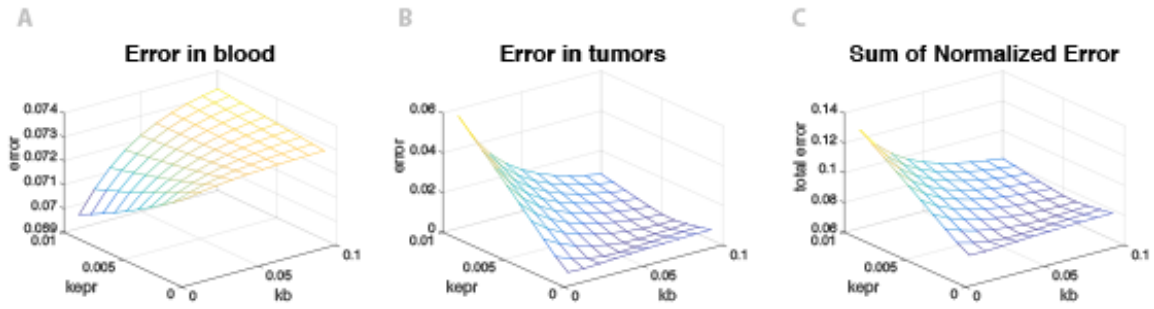

Figure 2-4. Optimization of fit to 3-compartment model.
To optimize fit of the 3-compartment model to our data, the error for fits over a course of rate constants are normalized to concentration in (a) blood or (b) tumor. These values are summed to get the total normalized error that is minimized to provide the best values for k_{epr} and k_b.

2.4 Results

2.4.3 Tumor-free model

To determine a baseline for liposome pharmacokinetics, we first perform a standard 2-compartment pharmacokinetics model on a tumor free mouse. For this evaluation, the primary compartment is the vasculature and the second compartment is the peripheral tissue.[157] Evaluation of concentration in blood (Figure 2-5) at the selected time points (5 min, 30 min, 2 h, 6 h, 24 h, and 48 h) and fitting to these enables determination of kinetic rate constants, k_{el} = 0.01 h^{-1}, k_p = 17.6 h^{-1}, and k_d = 16.3 h^{-1}.

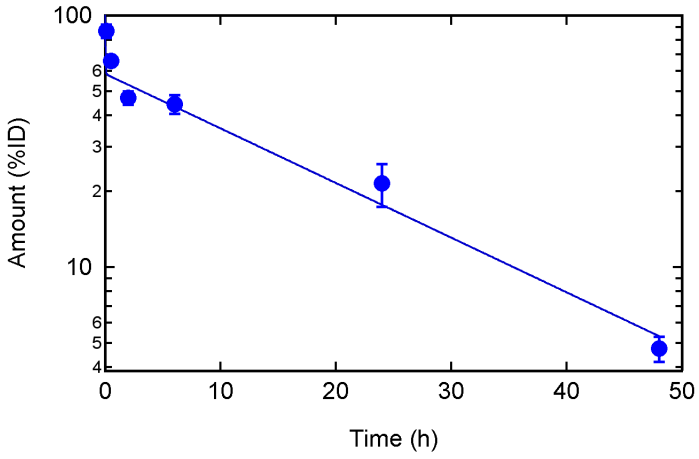

Figure 2-5. Pharmacokinetics of liposomal doxorubicin in tumor-free mice.
Concentration of doxorubicin-loaded liposomes in blood following tail-vein administration in non-tumor-bearing mice. The solid line is a fit to the data using the 2-compartment model from which we can extract the rate constants k_{el}, k_p, and k_d. n = 10 mice per time point. Data represents mean ± SE.

2.4.4 Tumor-bearing model

To next evaluate the EPR effect, pharmacokinetics and tumor accumulation are evaluated in a tumor-bearing mouse. The same time points are repeated in mice with LS 174T colorectal adenocarcinoma subcutaneous xenografts, and the concentration of doxorubicin in the blood (Figure 2-6A) and tumor (Figure 2-6B) are reported. To model the tumor-bearing mouse, a third, tumor, compartment is introduced into the model, and drug extravasation into this tumor compartment is described by the rate constant k_{epr} while intravasation from the tumor back into circulation is described by the rate constant k_b. The rate constants k_{el}, k_p, and k_d are held constant to allow determination of k_{epr} and k_b from simultaneous optimization of the model to both the pharmacokinetic and tumor accumulation data.

Measurements of accumulation of liposomal doxorubicin in the resected tumors show a maximum accumulation of 0.84 ± 0.23 %ID (1.8 ± 0.43 %ID/g) at 24 h. At longer times, we see the doxorubicin in the tumor decrease as the amount in the blood decreases, and hence the driving force for extravasation is increased. Based on the curve determined by optimization of fit, the maximum tumor accumulation is at approximately 15 h. By this point, the liposomal doxorubicin in circulation has reduced to 20 %ID.

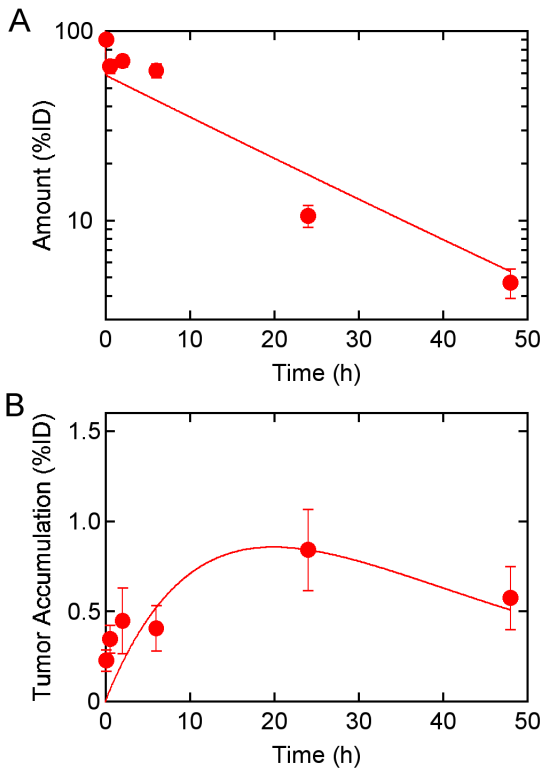

Figure 2-6. Pharmacokinetics and tumor accumulation of liposomal doxorubicin in LS 174T xenografts.
Concentration of doxorubicin-loaded liposomes in (a) blood and (b) tumors following tail-vein administration in tumor-bearing mice. The solid line is a fit to the data using the 3-compartment model. Using the rate constants k_{el}, k_p, and k_d extracted from the non-tumor-bearing mice we can use these fits to determine values for the rate constants k_{epr} and k_b. n = 7-9 mice per time point. Data represents mean ± SE.

Comparison of the liposomal doxorubicin in circulation between the LS 174T bearing and tumor free mice reveals that the impact of the tumor is not sufficient to decrease the amount in circulation (Figure 2-7). The tumor represents only a small portion of the overall volume in circulation, and consequently, the pull from that volume is not noticeable on the overall pharmacokinetics of the drug. If the tumor in question grows to a size large enough to have an effect on the overall drug pharmacokinetics, it may further alter this model.

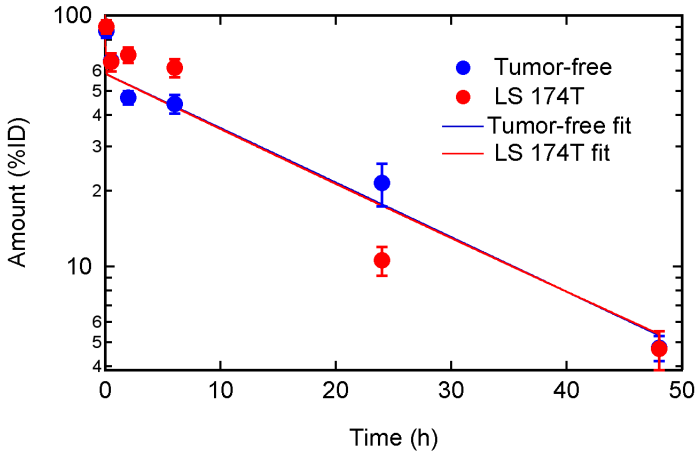

Figure 2-7. Concentration in blood comparing tumor-free and LS 174T-bearing mice. Concentration in blood of doxorubicin-loaded liposomes in (blue) tumor-free and (red) LS 174T tumor-bearing mice. The solid lines are fits to the data. The rate constants k_{el}, k_p, and k_d are determined from fits to the tumor-free mice and held constant in fits to the LS 174T tumor-bearing mice. The values for k_{epr} and k_b. found for the LS 174T tumor-bearing mice are insufficiently large to alter the pharmacokinetics of liposomal doxorubicin in a quantifiable manner. n = 10 mice per time point for tumor-free mice, and n = 7-9 mice per time point. Data represents mean ± SE.

The rate constants determined for liposomal doxorubicin in athymic mice are found in Table 2-1. These first order rate constants are determined in experiments of both tumor-bearing and tumor-free mice. To determine k_p, k_d, and k_{el}, tumor-free mice are used and pharmacokinetic data is fit to a 2-compartment model. This yields the rate constants k_p = 17.6 h^{-1}, k_e = 16.3 h^{-1}, and k_{el} = 0.1 h^{-1}. Then, introduction of subcutaneous LS 174T xenografts into athymic mice and fit to a 3-compartment model using tumor accumulation data facilitates fits to k_{epr} and k_b. This yields the rate constants k_b = 0.068 h^{-1}, k_{epr} = 0.003 h^{-1}.

Table 2-1. Rate constants for pharmacokinetic modeling of liposomal doxorubicin.
The first order rate constants for modeling liposomal doxorubicin in mice. All values are in h^{-1}. The elimination rate constant, k_{el}, and the rate constants that describe movement between the vascular and peripheral compartments, k_p and k_d, are determined with fits to data obtained in tumor-free mice. These are then held constant to model data from LS 174T tumor-bearing mice to determine values for the rate constant to describe movement into the tumor compartment from the circulation and back, k_{epr} and k_b, respectively.

		LS 174T
	Tumor-free	Tumor-bearing
k_p	14	
k_d	19.9	
k_{el}	0.1	
k_{epr}	-	0.002
k_b	-	0.05

2.4.5 Comparison of tumor type

To further elucidate the impact of the EPR effect, three tumor types were compared to determine the variation in tumor accumulation after administration of the same dose of liposomal doxorubicin. Mice with subcutaneous breast adenocarcinomas (MDA-MB-231) and mice with subcutaneous pancreatic adenocarcinomas (Capan-1) were compared with the LS 174T colorectal adenocarcinoma data at 6 h and 24 h (Figure 2-8). The highest tumor accumulation occurs in the LS 174T xenograft (0.84% ± 0.23), almost a 20-fold increase over the Capan-1 pancreatic adenocarcinoma xenograft (0.04% ± 0.01) at 24 h. The maximum tumor accumulation seen in MDA-MB-231 is moderate (0.18% ± 0.06). Of note is that the difference in total tumor accumulation (%ID) at 24 h for all 3 tumor types is

statistically significant. Comparing tumor accumulation normalized to tumor weight (%ID/g) yields statistical significance between LS 174T and Capan-1 xenografts along with MDA-MB-231 and Capan-1 at 24 h. The difference between LS 174T and MDA-MB-231 tumor accumulation is not statistically significant when normalized to tumor weight.

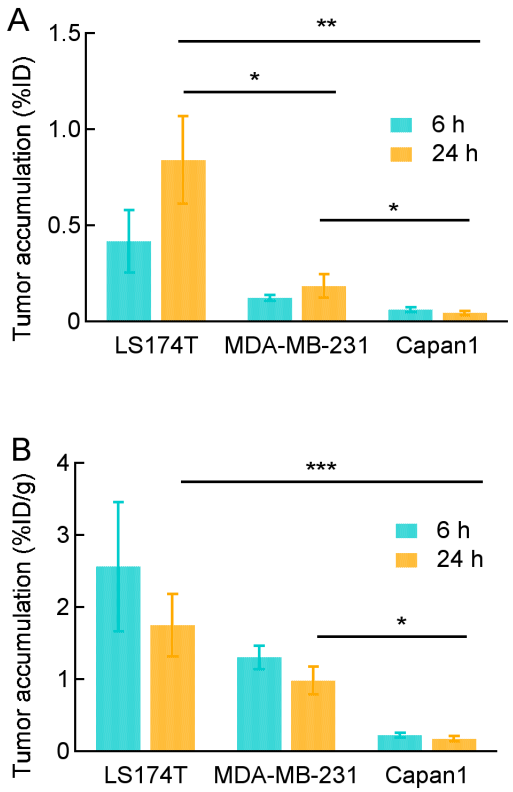

Figure 2-8. Comparison of tumor accumulation for different tumor types.
Tumor accumulation in subcutaneous xenografts at 6 and 24 h post injection of doxorubicin-loaded liposomes from three different cell lines is compared and reported as (a) total accumulation, %ID, and (b) accumulation normalized to tumor weight, %ID/g. n=7-9 mice. Data represent mean ± SE. Statistical significance was determined using a Student's t-test. *** $p \leq 0.001$, ** $p \leq 0.01$, * $p \leq 0.05$.

With the decrease in tumor accumulation for the Capan-1 and MDA-MB-231, it becomes obvious that the rate constant for modeling Doxil extravasation to the tumor, k_{epr}, will be lower. While this study does not encapsulate sufficient time points to determine all pharmacokinetic parameters to full accuracy for Capan-1 and MDA-MB-231, it is possible to hone in on the rate constant for extravasation to the tumor, k_{epr}, and to determine its magnitude by fitting to the data.

For this fit, two strategies were tried. The first fixed the ratio of k_{epr} to k_b and allowed k_{epr} to decrease. This strategy unfortunately did not appear to match the data as the fit initially increased too slowly while at longer times the fit had too high of tumor accumulation as compared with the data. The second strategy fixed k_b to the value obtained from the LS 174T data and solely optimized k_{epr}. This appeared to provide excellent fits to the experimental data for both Capan-1 and MDA-MB-231 (Figure 2-9). The rate constants decrease from k_{epr}=0.003 h^{-1} for LS 174T to k_{epr}=0.00054 h^{-1} for MDA-MB-231 and k_{epr}=0.00022 h^{-1} for Capan-1. Over an order of magnitude of variation can be seen between k_{epr} for tumors that have high and low efficacy of nanoparticle delivery, demonstrating that variations in tumor type can have significant impact on a nanomedicine's ability to extravasate into the tumor.

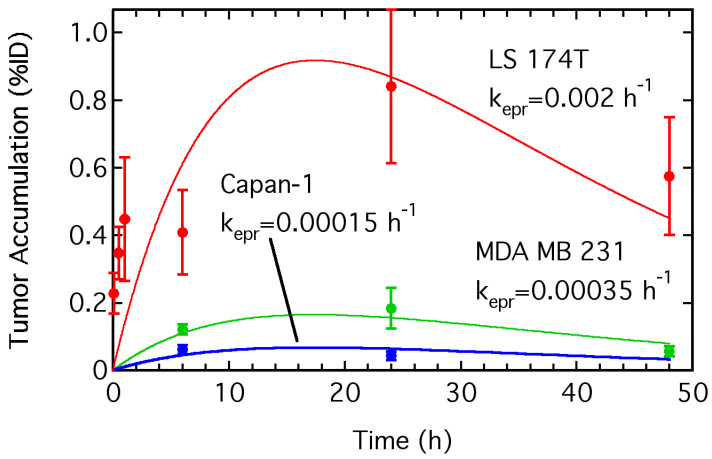

Figure 2-9. Approximation of k_{epr} with tumor type variation.
Tumor accumulation in subcutaneous xenografts of doxorubicin-loaded liposomes in subcuctaneous xenografts of (red) LS 174T colorectal adenocarcinoma, (green) MDA MB 231 breast adenocarcinoma, and (blue) Capan-1 pancreatic adenocarcinoma. Corresponding rate constants that describe the impact of the EPR effect for each cell type are included. n=7-9 mice. Data represent mean ± SE.

2.4.6 Discussion

Tumor accumulation is mediated by the EPR effect, however, the leakiness of the tumor vasculature is dependent on the tumor type. We have shown a 20-fold difference in tumor accumulation of doxorubicin-loaded liposomes in different tumor types. This implies that the kinetics of tumor accumulation are modulated by the tumor-specific vascular architecture. Therefore, elucidating the relationships between vascular structure, the EPR effect, and tumor accumulation will be key to improved treatment of solid tumors, and could contribute to advancing individualized care.

These results highlight two important points. (1) The large differences in tumor accumulation provide evidence that drug accumulation (for the same drug and same size tumor) is tumor specific. (2) Comparison of drug delivery systems can only be made if pre-clinical trials are performed under identical conditions: i.e. drug delivery system A in tumor X cannot be compared to drug delivery system B in tumor Y. In addition, the numerical value of tumor accumulation in units of %ID/g has become synonymous with the delivery efficiency of a delivery platform. Our results show that this dogma can be very misleading unless differences in tumor type can be accounted for.

2.5 Conclusions

To validate our model for tumor accumulation we have performed a preliminary study measuring the concentration in blood and tumor accumulation in subcutaneous LS174T xenografts (8 - 10 mm) in Nu/Nu mice using following administration of Doxil at 6 time points (5 min, 30 min, 1 h, 6, h, 24 h, and 48 h) at a dose of 0.15 mg (6 mg/kg). Comparison of the amount of the drug in circulation between tumor-bearing mice and non-tumor bearing mice shows that tumor accumulation is not sufficiently large to decrease the amount in circulation (Figure 2-7). Measurements of accumulation of Doxil in the resected tumors show a progressive increase to a maximum of 0.84 %ID (1.8 %ID/g) followed by a decrease at longer times (Figure 2-6). To analyze the data, we first fit the drug concentration in blood in animals with no tumor to obtain values for k_{el}, k_p, and k_d. These values are then used to fit to the data for tumor accumulation in tumor bearing mice to

obtain values for k_{epr} and k_b using a non-linear least squares fit. The rate constants for k_{epr} and k_b describe the kinetics of tumor uptake by the EPR effect.

Chapter 3 : Evaluation of the Impact of Pharmacokinetic Parameters on the EPR Effect

3.1 Introduction

Chemotherapeutics are inherently toxic and hence treatment is invariably a balance between inducing cancer cell death and minimizing the adverse side effects associated with drug accumulation in normal tissue and other organs.[159, 160] Combination products and nanotechnology provide the possibility of creating delivery systems where the design constraints are decoupled, allowing new approaches for reducing the unwanted side effects of systemic delivery, increasing tumor accumulation, and improving efficacy.[161-166] The development and translation of new nanomedicines is extremely challenging and hence progress in the field has been relatively slow. Of the 6 FDA-approved nanomedicines for treatment of solid tumors, two are antibody-drug conjugates, 3 are liposomal formations of anti-cancer drugs, and one is a protein-drug complex.[5] Unfortunately, while drug delivery systems are evaluated for clinical efficacy, pre-clinical trials often omit optimization of the platform itself.

As a specific example of how pre-clinical trials are designed to assess efficacy and not optimize the delivery platform, pharmacokinetic models for data analysis (Figure 2-3) lump tumor accumulation into the rate constant for clearance (k_{el}), which includes clearance by the kidneys, clearance by the MPS, and any other clearance mechanisms.[167] Tumor accumulation is an important parameter in developing a delivery platform for two reasons: (1) it can be optimized by tuning physico-chemical properties, and (2) by optimizing tumor accumulation it is possible to decrease the dose and minimize unwanted side effects due to uptake in normal tissue. These considerations are not applicable for small molecule therapeutics since the intrinsic properties of the molecule itself determine pharmacokinetic properties and cannot usually be tuned independently. Many small molecule chemotherapeutics are extremely toxic and are taken up in normal tissues as evidenced by large distribution volumes.[168] A recently developed model introduces a tumor' compartment, allowing for quantitative analysis of tumor accumulation.[169]

Building a knowledge base is key to advancing a scientific field since it enables the development of design rules that, in turn, accelerate the translation of new technologies. In Chapter 2, we have (1) determined the kinetics of accumulation of Doxil, an FDA-approved liposomal nanomedicine, in LS174T tumors, (2) applied a 3-compartent model to model to quantitatively assess tumor accumulation by defining a "tumor compartment", and (3) shown that tumor accumulation of Doxil is dependent on tumor type in a murine model. The development of nanomedicines

has been largely empirical, and hence there is a lack of robust design rules that can be used to develop and optimize new platforms. In order to address this knowledge gap, we aim to predict the impact that variations in physico-chemical properties of nanomedicines will have on the model used for tumor accumulation, and hence the impact these variation will have on efficiency of nanomedicine delivery to the tumor.

The accumulation of a drug delivery system in a solid tumor is mediated by the EPR effect, which describes the increased permeability of the tumor vasculature and increased retention associated poor lymphatic drainage.[2, 3, 61, 162, 170-176] In a growing solid tumor, the combination of hypoxic environment and inflammatory response leads to the formation of new vessels, local removal of smooth muscle cells, and degradation of basement membrane and extracellular matrix (ECM).[62, 177] At the same time, the proliferation of tumor cells causes expansion of the microenvironment and generates local compressive forces.[1] Expansion increases the average spacing between vessels, reducing the supply of nutrients, and creating hypoxic regions in the tumor. The compressive forces generated by tumor growth lead to contraction of blood vessels, increased resistance to blood flow, poor lymphatic drainage, and increased interstitial fluid pressure.[1]

Accumulation of a drug or nanomedicine in a solid tumor by the EPR effect is dependent on the time-dependent concentration in blood, and hence requires knowledge of the pharmacokinetics. The standard two compartment model (central and peripheral compartments) combines tumor accumulation with clearance by the

kidneys and the MPS (Figure 2-3A).[144] To distinguish tumor accumulation by the EPR effect from other elimination pathways, a model has been developed incorporating a tumor compartment and define rate constants specifying drug accumulation and removal from the tumor (Figure 2-3B). [158] Drug extravasation into the tumor by the EPR effect is described by the rate constant k_{epr}, and intravasation from the tumor back into circulation is described by k_b. The rate constant k_{el} describes elimination by the kidneys, MPS, and any mechanisms other than tumor uptake. The amount of drug is defined in the different compartments: N_{bl}, N_p, and N_t represent the amount (in mg) of drug in blood, peripheral tissue, and tumor tissue, respectively. This model has been used to analyze data from human clinical trials of Doxil, a liposomal formation of doxorubicin, and free doxorubicin. From fits to pharmacokinetic data, k_p, k_d, and k_{el} are extracted, and then extrapolation of different values of k_{epr} and k_b determine their influence on tumor accumulation.[158] This work shows how tumor accumulation can be analyzed quantitatively.

3.1.2 Design rules for drug delivery systems

Over the past 10 years there have been more than 17,000 publications with the word "nanomedicine(s)" in the title or abstract, and around 8,000 with both "nanomedicine(s)" and "cancer". Despite the large number of pre-clinical trials of drug delivery systems, surprisingly few report quantitative data that that would be useful in developing design rules. In a recent meta-study we reviewed 74 pre-

clinical trials of drug delivery platforms that reported quantitative values of tumor accumulation[11] and showed how the variability in experimental design significantly limits the ability to make the comparisons necessary to develop design rules. Specific problems include: variability in the tumor model, inconsistent reporting of tumor size/weight, inconsistent reporting of dose, inconsistent reporting of physico-chemical properties, tumor accumulation reported at different time points, and variability in controls (especially for active targeting). This variability inhibits the development of specific design rules for nanomedicine development.

Several groups have used intravital microscopy to image extravasation of fluorescently labeled dextrans from the tumor vasculature.[61, 171, 175, 178, 179] These studies are limited to the tumor periphery due to the poor depth of penetration and hence do not provide insight into extravasation and uptake throughout the tumor. Nonetheless, an important observation from these studies is that the cut-off size for extravasation from the tumor vasculature in animal models varies from 200 nm to 1.2 μm depending on the tumor type.[61, 171, 175] Based on these studies, a diameter of about 200 nm is often considered an upper limit for successful drug delivery.[162, 176] We note that this is one of the few design rules to emerge from basic nanomedicine research. In the most sophisticated of these intravital microscopy studies, the Chilkoti group used a model with a tumor compartment for semi-quantitative analysis of the extravasation and tumor uptake of fluorescently labeled dextrans.[180] In summary, the kinetics of the EPR effect

are poorly understood despite being key to systemic delivery of drugs (and contrast agents) to solid tumors.

In this chapter, we aim to use this model to determine how variations in physicochemical properties of the nanomedicines might impact the rate constants , k_p, k_{epr}, and k_{el}, and hence how these will ultimately affect the tumor accumulation in the model. This can improve the design of nanomedicine optimization by providing insight into the physicochemical properties that may be smarter to focus on optimizing. This section will provide quantitative tools and mathematical models necessary to accelerate the development and translation of drug delivery systems.

3.2 Methods

3.2.1 Model

The pharmacokinetics and tumor accumulation are evaluated using the 3-compartment model described in Chapter 2. In short, the drug is administered into the vascular compartment and travels between that compartment, a peripheral tissue compartment, and a tumor compartment (Figure 2-3). The drug exchange between the vascular and peripheral tissue compartment is described by the rate constants k_p and k_d while the drug exchange between the vascular and tumor compartments is described by the rate constants k_{epr} and k_b. The rate constant of elimination, k_{el}, encompasses all clearance pathways including the MPS and renal clearance.

3.2.1 Data used for initial fits

Current pharmacokinetic parameters are determined for pegylated, doxorubicin-loaded liposomes and free doxorubicin. We have optimized the parameters k_p, k_d, k_{epr}, k_b and k_{el} in athymic nu/nu mice with subcutaneous LS 174T tumors in Chapter 2 and will use these values as a starting point for evaluation of the change in each value.

To additionally address how this might impact human patients, this will additionally be compared with data from human clinical trials.[14] This data was obtained for Doxil in 1994 in patients suffering from a range of tumor types, including pancreatic cancer, ovarian cancer, mesothelioma, soft tissue sarcoma, breast cancer, and non-small cell lung carcinoma.[14] This study reports values describing the shape of the pharmacokinetic curve that are then used to obtain k_b, k_p, and k_{el} for Doxil. Tumor accumulation is not reported in humans, so these values are estimated using the k_{epr} and k_b determined in murine data.

3.2.1 Evaluation of altering pharmacokinetic parameters.

In this section, we hone in on the rate constants k_p, k_{epr}, k_b and k_{el}. Each rate constant is decreased by the same factors: 1 (no change), 2, 5, and 10 and the pharmacokinetics and tumor accumulation are compared. For each parameter, the

physical significance is discussed to determine the impact of changing the nanomedicine at various time points.

3.3 Results

3.3.1 Impact of altering k_p

By altering the drive for a medicine to accumulate in the peripheral, healthy tissues, not only will more of the drug will be available for delivery to the tumor, less chemotherapeutics will reach and harm the healthy tissues. This decrease in drug that arrives at healthy tissues could be accomplished by increasing the size of a medicine, for example through incorporation of a drug into a nanoparticle, or changing the medicine's charge or surface properties. To model this, we evaluated a reduction in k_p, the rate constant into the peripheral compartment.

Evaluation of this decrease in humans with respect to free doxorubicin in circulation from Gabizon [14] can be seen in Figure 3-1. Initially, this leads to increased drug in circulation; however, at a point the amount in circulation decreases due to higher availability for elimination pathways. In parallel with this, the reduction in peripheral rate constant initially leads to increased accumulation in the tumor, but as the concentration gradient moves to drive the drug out of the tumor, the amount in the tumor is reduced.

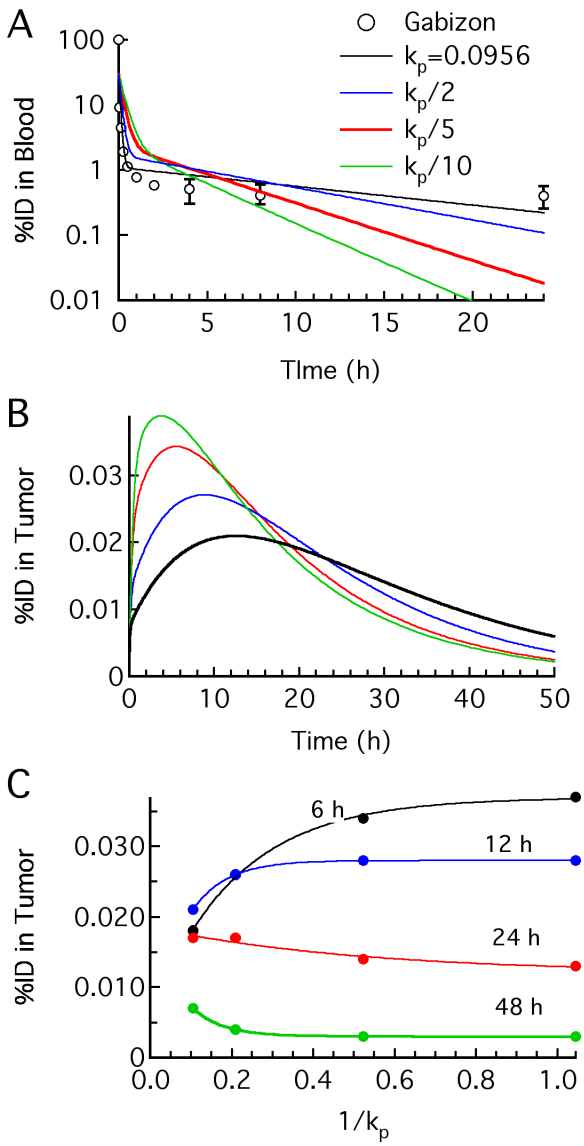

Figure 3-1. Impact of altering k_p for free doxorubicin in humans.
Reducing the rate constant for extravasation into peripheral tissues, k_p, initially increases the amount in (a) blood and (b) tumor. At longer time points, the concentration in blood and tumor for decreased k_p is also reduced. (c) Tumor accumulation change with respect to change in k_p highlighted at 6 h, 12 h, 24 h, and 48 h.

Decreasing k_p for doxorubicin may be best compared with doxorubicin encapsulated in an unpegylated liposome, for example Myocet. The pharmacokinetics of Myocet has been compared with doxorubicin in humans, and compared with free doxorubicin, Myocet sees a shorter distribution phase with a steeper elimination half life. [181] These trends are both indicative of a decrease in k_p that we have anticipated due to the increase in size. While there may be additional interactions at play here, these general trends are confirmation of the effects of altering the rate constant k_p. If these trends hold true, we may expect that the amount of Myocet, and consequently the amount of doxorubicin, in the tumor will be higher up until shortly after the time where the amount Myocet in blood would dip below the amount of free doxorubicin. This appears to happen around the fourth day post-injection in the case of Myocet [181], seemingly providing 4 days of sustainably higher chemotherapeutic delivery to the tumor.

To evaluate a further decrease in peripheral tissue, we assessed the impact of further reducing the uptake in peripheral tissue in a nanoparticle. For nanoparticles, uptake in peripheral tissue is already low and renal clearance reduced due to the increase in size. In this instance, the general trends mimic the reduction seen in the free doxorubicin: initial increase in distribution in circulation and the tumor followed by subsequent drop off. This can be seen for data both from human clinical trials (Figure 3-2) and from fits to the murine data (Figure 3-3).

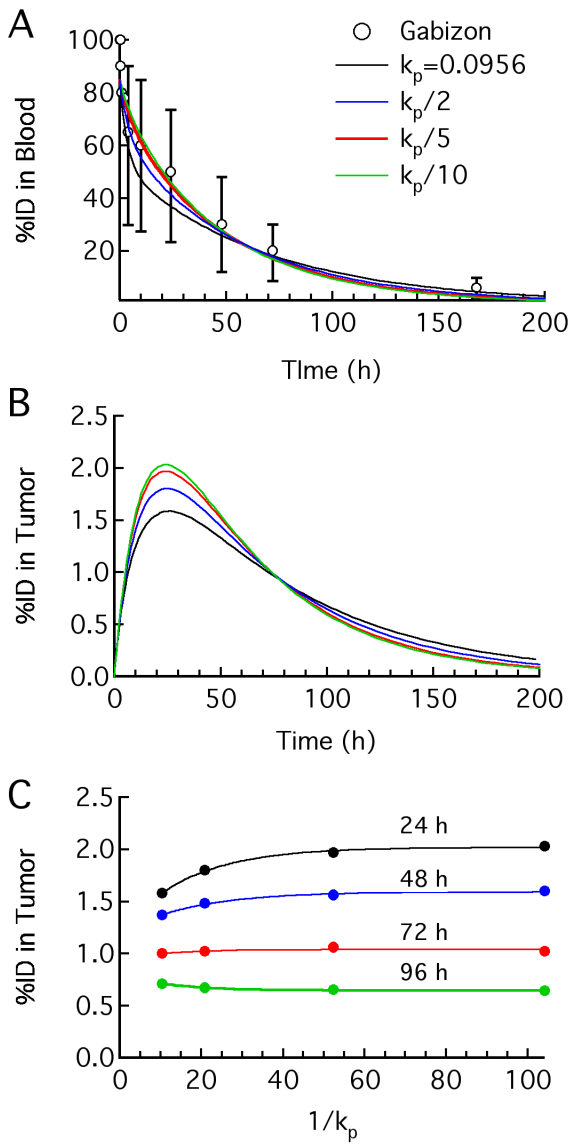

Figure 3-2. Impact of altering k_p for liposomal doxorubicin in humans.
Similar to free doxorubicin, reducing the rate constant for extravasation into peripheral tissues, k_p,, initially increases, yet at longer time points decreases, the amount in (a) blood and (b) tumor. (c) Tumor accumulation change with respect to change in k_p highlighted at 24 h, 48 h, 72 h, and 96 h.

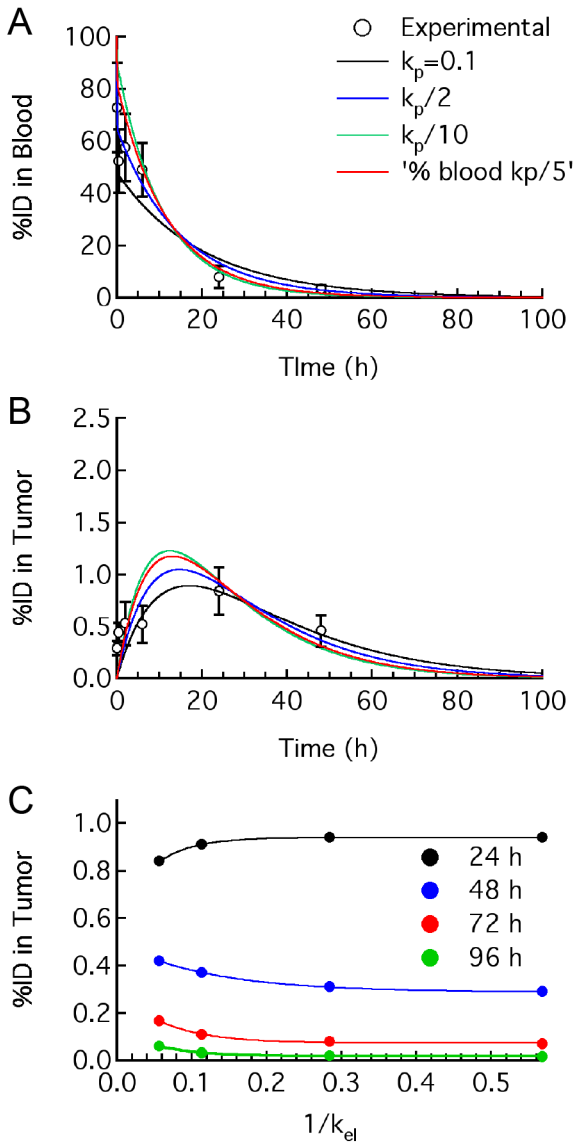

Figure 3-3. Impact of altering k_p for liposomal doxorubicin in mice.
In mice, reducing the rate constant for extravasation into peripheral tissues, k_p,, yields similar results as in humans. The amount in (a) blood and (b) tumor initially increases with and at longer times decreases with respect to the initial. (c) Tumor accumulation change with respect to change in k_p highlighted at 24 h, 48 h, 72 h, and 96 h.

3.3.2 Impact of altering k_b

When a targeting ligand is added to a nanoparticle, the alteration in the nanoparticle's behavior will depend on the mechanism of the targeting ligand itself. Many targeting ligands seek out and adhere to elements in the tumor itself. In this instance, the addition of targeting may not alter the extravasation into the tumor. Instead, the addition of targeting will reduce the release back into circulation because the nanomedicine will have bound to the tumor.

To model this, we focus on decreasing the rate constant for modeling kinetics from the tumor compartment back into the vasculature, k_b. The result of these fits to data from human clinical trials can be seen in Figure 3-4. If the targeting ability could reduce this rate constant by a factor of 5, then the tumor accumulation in the tumor 24 h is increased by a factor of 1.2, at 48 h is increased by a factor of 2.7, and this trend continues even at longer times.

To compare the model for human trials to data derived from murine experiments, we also applied this to the experimental data from experiments in mice (Figure 3-5). The trends seen here mimic those from human data. With addition of targeting to a nanomedicine, the amount of nanomedicine in blood over time is not significantly altered, yet the amount in the tumor is substantially increased.

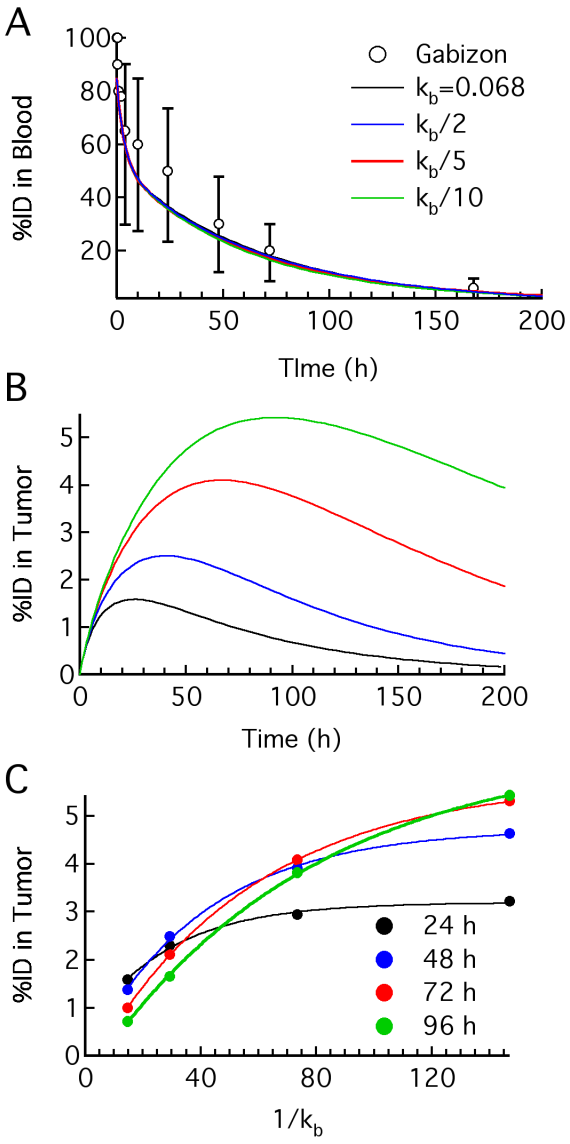

Figure 3-4. Impact of altering k_b for liposomal doxorubicin in humans.
(a) Decreasing the rate constant for transport from the tumor back into circulation has minimal effect on the amount of liposome in circulation. (b) Tumor accumulation is increased compared with decreasing k_b, especially at longer time points when compared with no change in k_b. (c) Tumor accumulation change with respect to change in k_b highlighted at 24 h, 48 h, 72 h, and 96 h.

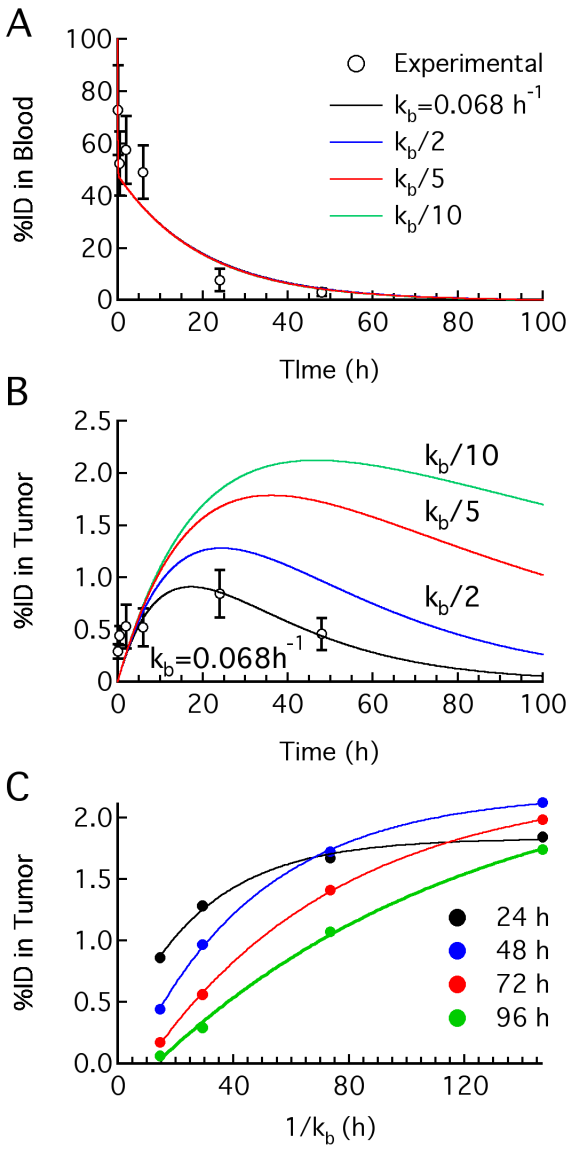

Figure 3-5. Impact of altering k_b for liposomal doxorubicin in mice.
(a) As with fits to human data, decreasing the rate constant for transport from the tumor back into circulation has minimal effect on the amount of liposome in circulation. (b) Tumor accumulation is increased compared with decreasing k_b. (c) Tumor accumulation change with respect to change in k_b highlighted at 24 h, 48 h, 72 h, and 96 h.

3.3.3 Impact of altering k_{el}

Evasion of elimination pathways will increase the drug available in circulation and consequently the amount of drug delivered to the tumor. One method to reduce the elimination pathways is avoidance of renal clearance; this is a primary draw of nanoparticles themselves since particles in circulation greater than approximately 8 nm have been shown to evade clearance via the kidneys.[182, 183] It is an important caveat, however, that this is both a benefit and a curse of nanomedicine. Ultimately, removal of nanomedicines from the body is desirable since nanoparticles remaining in the body for long-term periods of time is not ideal.

Additional reduction in elimination is achieved through reduction in elimination via the MPS. This is often accomplished through altering surface properties of a nanomedicines. Pegylation, for example, is known as a "stealth" coating for this very reason. To evaluate the effect of additional reduction in this clearance, we model a reduction in the elimination rate constant, k_{el}. The effect that this reduction would have had on the human clinical trial data can be seen in Figure 3-6. This does not impact the distribution phase of the pharmacokinetics in a significant manner, but it does increase the amount of drug in circulation in circulation during the elimination phase. For example, with a 5-fold reduction in this elimination rate constant, the amount of liposomal doxorubicin expected in the tumor increases by 1.2-fold at 24 h and 1.5-fold at 48 h.

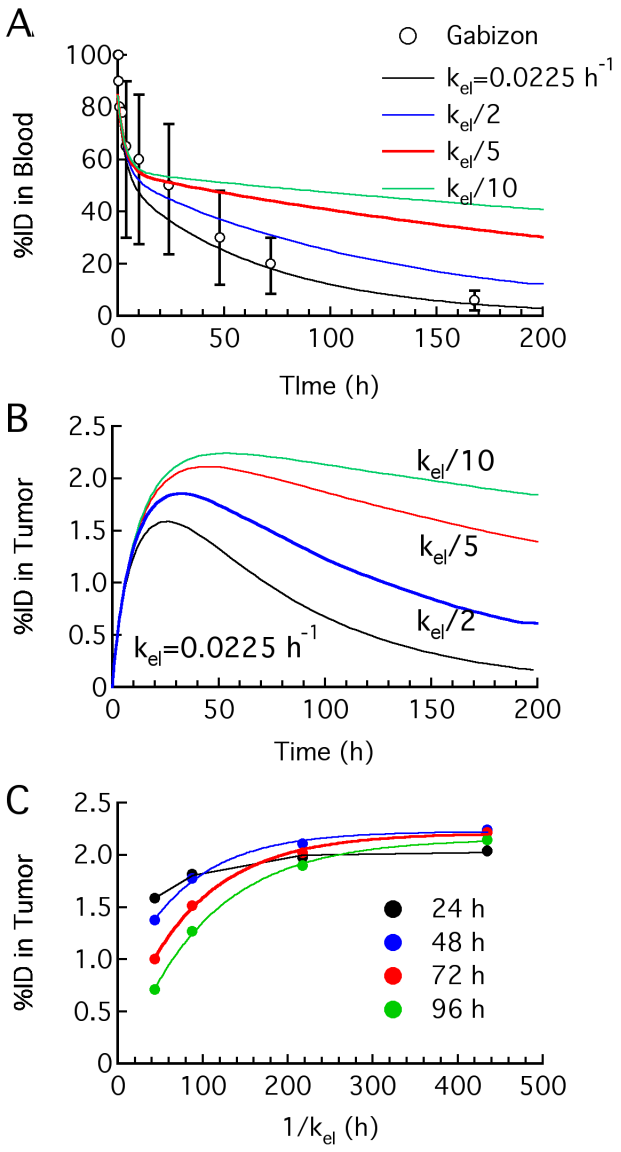

Figure 3-6. Impact of altering k_{el} for liposomal doxorubicin in humans.
(a) The concentration in blood is increased as the elimination rate constant, k_{el}, decreases. (b) The increase in blood concentration leads to increased tumor accumulation over time. (c) Tumor accumulation change with respect to change in k_{el} highlighted at 24 h, 48 h, 72 h, and 96 h.

The impact of the reduction in the elimination rate constant can also be seen in the model to the murine data (Figure 3-7). The trends between fitting to murine and human data are highly similar due to the fits being obtained with the same model.

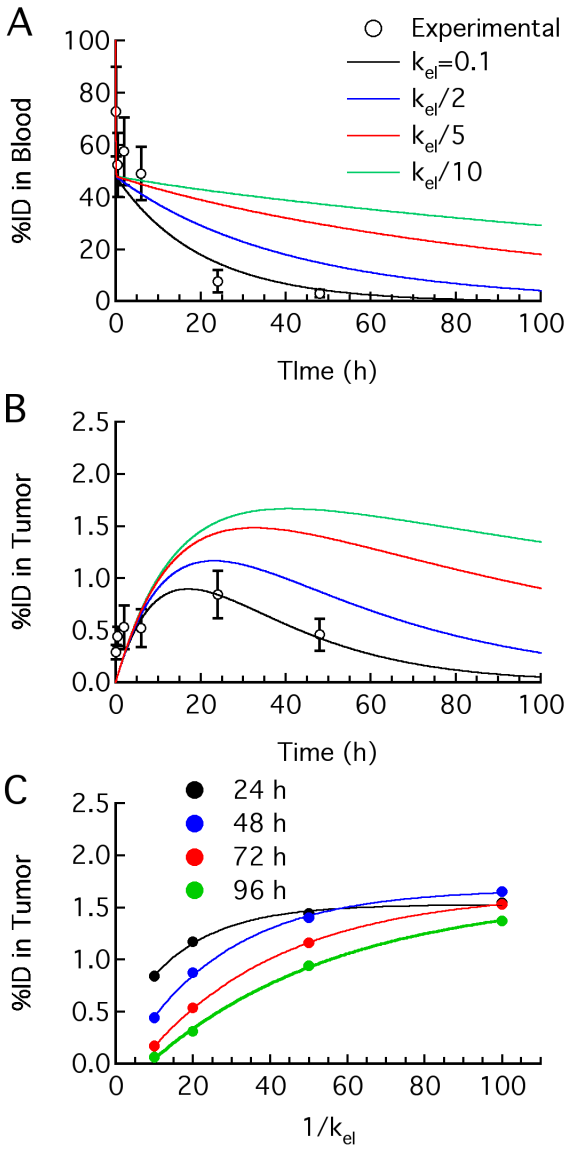

Figure 3-7. Impact of altering k_{el} for liposomal doxorubicin in mice.
(a) As k_{el} decreases, the elimination half-time is increased, leading to higher amounts of liposomal doxorubicin in blood at longer time points. (b) The increase in blood concentration leads to increased tumor accumulation over time. (c) Tumor accumulation change with respect to change in k_{el} highlighted at 24 h, 48 h, 72 h, and 96 h.

3.3.4 Impact of altering k_{epr}

As the tumor microenvironment changes, one common difference between tumors is the extent of vascularization. Less vascularized tumors may be represented in this model with a decrease in k_{epr} (Figure 3-8). In fact, we have shown in Chapter 2 that varying a tumor model can be approximated in this model by altering k_{epr}. In this clinical trial, patients had 6 different tumor types: breast cancer, non-small cell lung carcinoma, ovarian cancer, mesothelioma, soft tissue sarcoma, and pancreatic cancer. The result shown in Figure 3-8 demonstrates that the pharmacokinetic data obtained from blood samples will be minimally impacted by the variation in tumor type. However, this result, taken with the result comparing tumor types from Chapter 2 indicates that the liposome delivery may have varied greatly for patients with different types of tumors. As a consequence, efficacy in patients may additionally have been impacted.

To harness the fact that k_{epr} will vary to an experimental advantage, it is first important to acknowledge that different tumors will be better candidates for nanomedicine therapy than others. For tumors that are candidates, it may be useful to examine the extent of nanomedicine extravasation for a patient in order to personalize nanomedicine dosage information. This could be accomplished with whole body imaging of an inert nanoparticle (Chapter 4).

Finally, k_{epr} could potentially be altered by temporarily increasing a patient's systemic blood pressure. This has been investigated for nanomedicine delivery to lesser-vascularized tumors, for example pancreatic tumors.[184] In modeling, it would be important to note that increasing the blood pressure may additionally impact other rate constants in this 3-compartment model. Transport into healthy, peripheral tissues would also be increased, modeled by k_p. In this instance, tumor accumulation may even be further increased by a decrease in k_b.

3.4 Summary

By altering the rate constants associated with nanomedicine pharmacokinetics, tumor accumulation will be altered (Table 3-1). Reducing k_{epr} similarly reduces tumor accumulation. Reducing k_b will increase tumor accumulation as less of the nanomedicine is transported from the tumor back into circulation. A reduction in k_{el} will increase tumor accumulation, slightly at first and more substantially at longer time points. A reduction in k_p will also increase tumor accumulation at shorter time points, yet at longer times tumor accumulation is reduced.

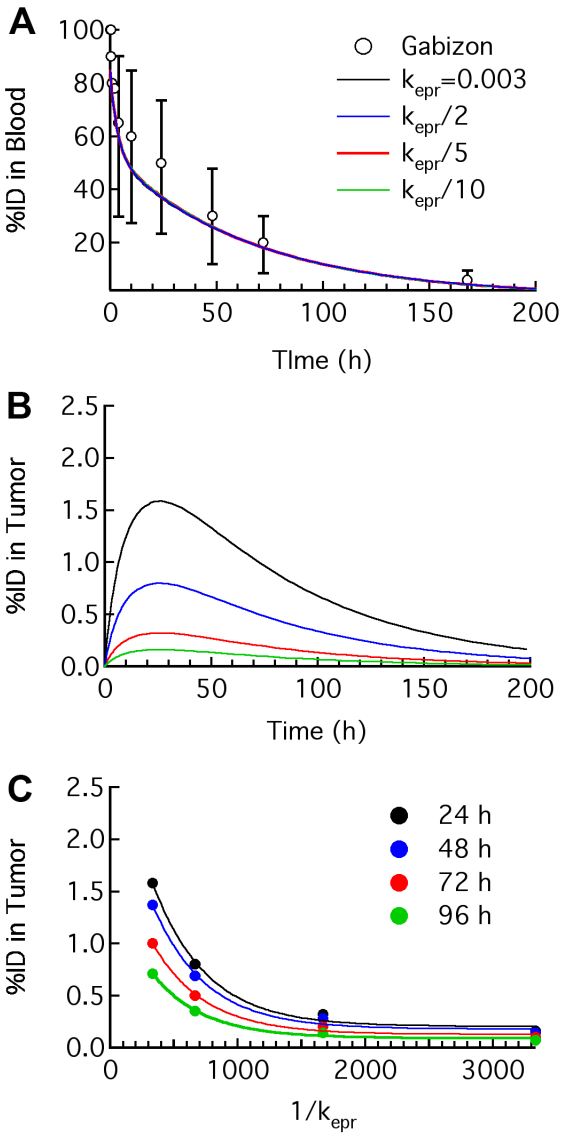

Figure 3-8. Impact of altering k_{epr} for liposomal doxorubicin in human.
(a) As k_{epr} decreases, the amount of liposomal doxorubicin in circulation is not significantly altered. (b) The tumor accumulation decreases with decreasing k_{epr}. (c) Tumor accumulation change with respect to change in k_{epr} highlighted at 24 h, 48 h, 72 h, and 96 h.

Rate constant	Action	Δ Accumulation at 24 h
k_{epr}	÷ 5	x 0.28
k_b	÷ 5	x 1.6
k_{el}	÷ 5	x 1.2
k_p	÷ 5	x 1.2

Table 3-1. Effect of altering the rate constants on tumor accumulation at 24 h.
Variations in k_{epr} are indicate variations in tumor "leakiness." Decreasing k_b by 5 shows the highest increase in tumor accumulation at 24 h, indicating that increasing tumor targeting will aid in nanoparticle retention in the tumor. At 24 h, the increase in tumor accumulation for decreasing k_{el} and k_p are identical; however, at longer time points, k_{el} will give greater tumor accumulation.

3.5 Future Directions

Based on the predictions above, it is logical to focus the first step of nanomedicine optimization on improving (i.e. reducing) the rate constant of elimination. The-state-of-the-art for MPS evasion is pegylation. Pegylated liposomes have relatively long clearance half-time, typically 1 - 4 days in patients.[16, 147, 149, 168] Pegylation is inexpensive and FDA-approved, but delays rather than suppresses opsonization and clearance by the MPS, and can eventually stimulate antibody generation.[17, 185]

Various alternative strategies for increasing circulation time have been explored, such as the use of exosomes created from host red blood cells[186-189] and marker-of-self proteins such as CD47 or CD200.[190-192] CD47 binds to the immune inhibitory receptor SIRPα (signal inhibitory protein) found on macrophages and is exploited by host red blood cells and invading cells, such as leukemia cells, melanoma cells, and leukocytes, that are known to avoid the immune system.[193-195] The ability of CD47 to facilitate evasion of the immune system could provides an excellent metric with which to explore a potential decrease in k_{el} and confirm the impact that may have on the pharmacokinetics and tumor accumulation of a particle and use these to confirm the applicability of the model.

This data also demonstrates that inclusion of active targeting will provide an advantage for tumor accumulation. Evaluation of how the pharmacokinetic parameters change with the addition of active targeting ligands, for example antibodies or aptamers, will provide insight into the extent of their impact on targeting efficiency.

Another future direction is expansion of this model to include other parameters, for example direct clearance from the tumor. At present, our understanding of the tumor microenvironment is not extensive enough to evaluate this parameter independently. In the 3-compartment model, clearance from the tumor is lumped into k_b. Improving imaging and understanding of nanomedicines in the tumor microenvironment will allow for better modeling of this behavior. For example, to

what extent are nanomedicines cleared by the lymphatic system? Additionally, how are nanomedicines digested within the tumor? Answers to these questions may be found with further imaging and chemical analysis of the tumor after administration of nanomedicines. Improving our understanding of clearance from the tumor will enable further refinement of the 3-compartment model.

Chapter 4 : Evaluation of the Impact of Pharmacokinetic Parameters on the EPR Effect

4.1 Motivation

4.1.1 Improved nanomedicine evaluation

Information regarding a nanomedicine's ability to arrive at the tumor and sustain presence there over time is important to determine if a nanoparticle is a good candidate for cancer nanomedicine. Unfortunately, this information is expensive and time consuming to obtain. For this reason, many labs shy away from these experiments. It would be advantageous to establish a platform to minimize these costs by facilitating the use of one mouse for the entire time course. The following is a preliminary evaluation of dye-loaded liposomes for evaluation of their affinity for a tumor. This could be used for a more rapid nanoparticle evaluation feedback loop for drug development.

Quantitative tools for analysis of tumor accumulation will accelerate the development and translation of drug delivery systems. If dye-loaded liposone could be used to test predictions of how pharmacokinetic parameters (e.g. distribution volume or clearance half-time) modulate tumor accumulation, it would allow researchers to make more rapid rational decisions on platform design.

To accelerate optimization of drug and gene delivery platforms, we will assess the feasibility of pharmacokinetic imaging. For delivery platforms where an IR dye can be incorporated into the platform (e.g. liposomes), information on tumor accumulation and other pharmacokinetic parameters can be obtained from whole body imaging. We will explore the limits of this approach as a tool to accelerate the development of drug delivery systems. As a proof-of-principle, we will examine the correlation between the pharmacokinetics and tumor accumulation of dye-loaded liposomes with the quantitative data from doxorubicin-loaded liposomes. The use of these dye-loaded liposomes could provide insight that is important in guiding the development of nanomedicines in a much more expedient manner, representing a feasible shift from empirical design to a rational design process.

For the criteria of evaluation of alterations in nanoparticle properties on tumor uptake, it will be important to introduce an imaging agent while maintaining the surface properties of the particle. In this instance, the dye cannot be attached to the surface on the chance that it will alter the properties even slightly. Encapsulation of an imaging agent within the particle may allow for determination of a nanoparticle's biodistribution and tumor accumulation via whole body imaging. Then, by altering the surface properties of said nanoparticle, it will be possible to visualize the variations that occur as a direct result of that property's change.

4.1.2 Improved patient dosing parameters

The scientific insight and quantitative models of tumor accumulation developed thus far could be implemented in the clinic as part of the shift towards individualized medicine. For example, imaging of an inert tracer (e.g. liposome containing a contrast agent) could be used to assess the leakiness of a patient's tumor and models used to design the dosing regimen for that patient to optimize tumor accumulation and minimize unwanted side effects.

Extravasation from circulation and tumor accumulation are mediated by the Enhanced Permeability and Retention (EPR) effect. Evidence from intravital microscopy studies suggests that the "leakiness" of tumor vasculature in mice is tumor specific.[61, 175, 196] While a correlation has not been established, these studies suggest that the accumulation of a drug delivery platform is tumor specific. A consequence of the hypothesis that tumor accumulation is tumor specific is that dosing of chemotherapeutic should be based, in part, on the "leakiness" of the tumor.

Every tumor develops in a unique manner, yielding one further reason that *in vivo* imaging could prove useful. Each patient's tumor may vary in vascularization, hence they may have varied levels of leakiness and varied response to treatment. If an individual's tumor could be evaluated prior to treatment to determine the efficiency of nanomedicine delivery, then a more exact understanding of doses necessary for

efficacy could be determined. This could be accomplished with an analogous nanomedicine with inert imaging ability.

4.2 Materials and Methods

4.2.1 Cell culture

LS 174T colorectal adenocarcinoma cells were purchased from American Type Cell Culture (ATCC) and cultured according to the corresponding guidelines. LS 174T cells were grown in Eagle's Minimum Essential Medium (EMEM) (Quality Biological) with 10% fetal bovine serum (FBS) (Life Technologies) and 1% penicillin streptomycin (P/S) (Life Technologies). Cells were maintained at 5% CO_2 and 37°C in a humidified incubator.

4.2.2 Animal models

All experiments were approved by and performed in accordance with the guidelines and regulations of the Animal Care and Use Committee for Johns Hopkins University. Athymic nu/nu female mice 4-6 weeks old were purchased from Charles River.

4.2.3 Xenograft

Subcutaneous xenografts were inoculated in the right flanks of nude, female mice. Approximately 5 million cells were suspended in 100 μL of 50% growth media and 50% growth-factor-reduced Matrigel (Corning). Cell suspensions were maintained on ice until subcutaneous inoculation. Xenografts were grown to 8-10 mm in diameter or approximately 0.2 g in weight prior to use in exeriments.

4.2.4 Liposome synthesis

Pegylated liposomes will be synthesized from 90 mol% hydrogenated soybean phosphatidylcholine (HSPC) and 10 mol% 1,2-distearoyl-sn-glycero-3-phosphoethanolamine-N-[amino(polyethylene glycol)-2000] (DSPE-mPEG2k), with a 1.6:1 lipid to cholesterol ratio, corresponding to the composition of Doxil liposomes. Briefly, lipids are mixed and dried under vacuum. Then, 0.5 mL of 0.1 mg/mL near-IR dye (ADS740WS) is added to the dry lipids for encapsulation within the liposomes. This solution is then subjected to 10 freeze-thaw cycles where the vial is dunked in alternating liquid nitrogen and room temperature water with intermittent agitation to loosen the lipids from the vial. The resulting solution is mechanically extruded 10 times back and forth through a 100 nm filter to form liposomes of a more uniform size distribution. The liposomes are then purified by gel chromatography using a Sepharose CL-4B column equilibrated in phosphate buffered saline (PBS) to remove all free dye molecules that have not been loaded into the liposomes.

4.2.5 Liposome administration

NIR-dye loaded liposomes are injected in 200 μL volume via lateral tail vein injection.

4.2.6 Animal imaging

Following administration of NIR-dye loaded liposomes, individual mice are sedated with isoflurane gas anesthesia at time points corresponding to tumor accumulation data for doxorubicin-loaded liposomes (Chapter 2). This is at 5 min, 30 min, 1 h, 6 h, 24 h, and 48 h post injection. Mice are then imaged on the LI-COR Pearle Impulse NIR Imager. Each mouse undergoes two single mouse scans, one on the dorsal side and one on the ventral side. All images for either the dorsal or ventral side of a single mouse are linked together to normalize intensity for direct comparison of fluorescent intensity.

4.2.7 Analysis

Fluorescence intensity is obtained from two regions of interest corresponding to: (1) the tumor and (2) the uppermost region of the mouse's tail in order to obtain fluorescence from the same tail vein portion on each mouse. These data will be compared to the tumor accumulation of doxorubicin-loaded liposomes from resected tumors at the same time points (Chapter 2) to assess the feasibility of pharmacokinetic imaging. The objective is to obtain the correlation coefficient

between tumor accumulation of doxorubicin-loaded liposomes obtained from HPLC analysis of resected tumors and tumor accumulation obtained from fluorescence imaging.

4.3 Results

4.3.1 NIR imaging data

Mice bearing LS 174T subcutaneous xenografts were injected via the lateral tail vein with near-infrared (NIR) dye loaded liposomes and imaged at 6 time points post-injection (5 min, 30 min, 2 h, 6 h, 24 h, and 48 h). These time points were chosen so that data can be compared with quantitative data from doxorubicin-loaded liposomes (Chapter 2). Two mice were imaged, the dorsal and ventral images for both mice are included in Figure 4-1. From analysis of the images (Figure 4-1), the signal-to-noise ratio at the shortest time point (≈ 0.3 %ID) is about 30, indicating that the resolution is sufficient for semi-quantitative analysis.

Comparing this data with the quantitative data for doxorubicin-loaded liposomes (Figure 2-6), we realize several similarities. By only five minutes post-injection we had already seen a drop in circulating liposomes. Whole body imaging reveals that by this point, a significant portion of the liposomes have already accumulated in the body, shedding light on the liposome biodistribution.

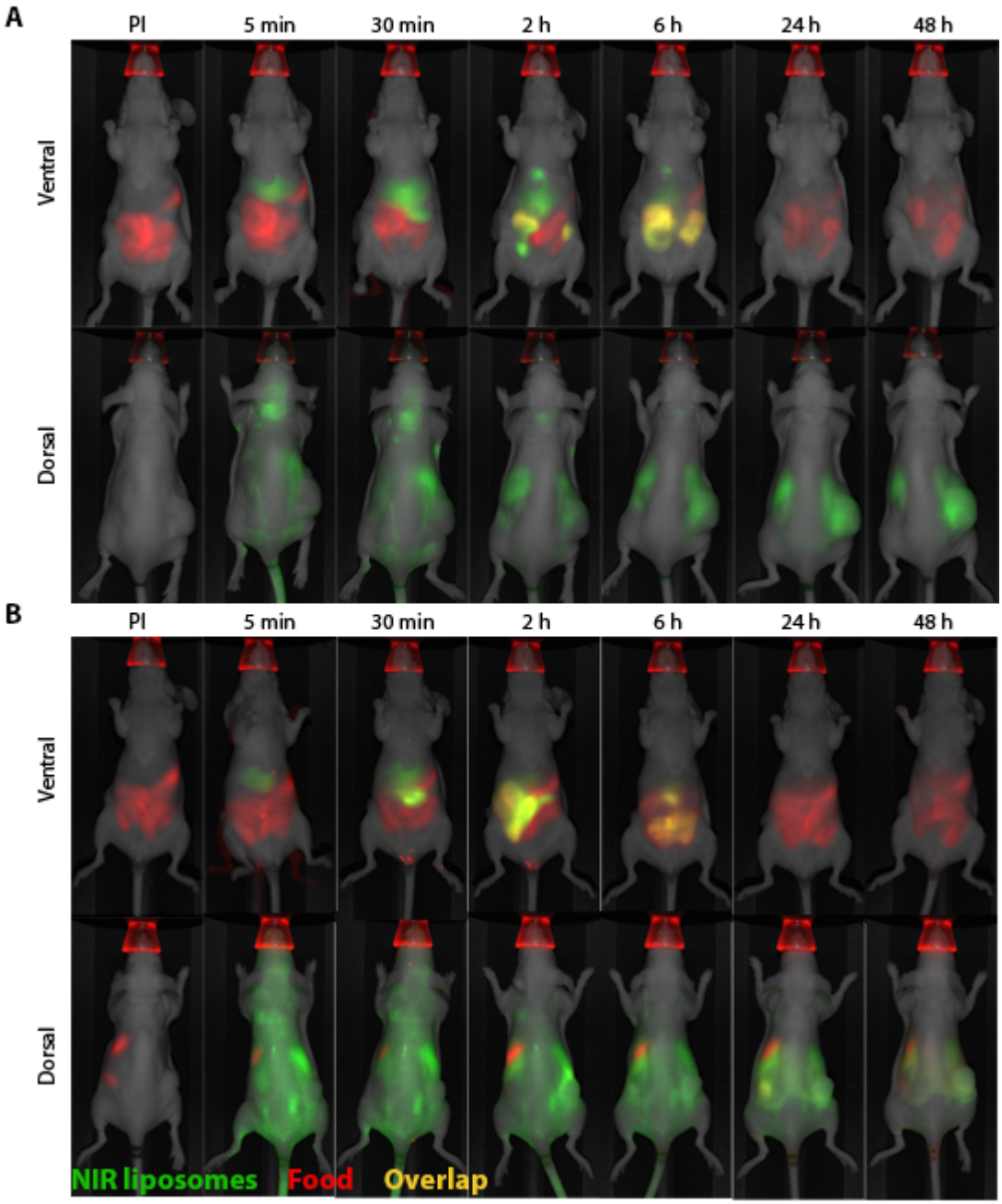

Figure 4-1. NIR dye loaded liposomes in mice over 48 h.
Semi-quantitative real-time pharmacokinetics. Whole body fluorescence imaging of a mouse with one subcutaneous LS174T flank xenograft in the right flank following administration of liposomes loaded with a near-IR dye. Data shown for (a) mouse 1 and (b) mouse 2. Near-IR dye (green), autofluorescence (red).

Looking ahead in the imaging to six hours post-injection reveals that the liposomes have colocalized in the stomach and intestines. At 24 h and 48 h post-injection, liposome concentration has decreased greatly, but the liposomes are still present in organs including liver, spleen, and intestines.

Tumor accumulation is not identical between the mice, indicative of variations in tumor architecture. The tumors are on the right flank, seen on the ventral side of each mouse. In the mouse seen in Figure 4-1A, the accumulation in the tumor increases to a maximum at 48 h, while in Figure 4-1B, the maximum tumor accumulation is seen at 2 h. In both instances, tumor accumulation at 48 h is still observable and significant.

The main deterrent seen in these images is the renal accumulation that can be visualized on the mid-left region of each mouse's ventral side. Renal accumulation does not occur in liposomes as large as 100 nm, so uptake in the kidneys is a possible indication of dye leakage from the liposomes.

Overall, whole body imaging sheds light on the liposomes' biodistribution. While tumor accumulation will vary for different tumors, but the biodistribution trends seen in each mouse are similar.

4.3.2 Correlation of NIR imaging to HPLC analysis of doxorubicin-loaded liposomes

For each mouse, the intensity in the tail region and in the tumor region was determined at each time point and normalized to 1 at the maximum for each. These values were averaged at each time point and then re-normalized at the maximum to provide the trends shown in Figure 4-2. These intensities follow the same general trends as for the pharmacokinetics and tumor accumulation of doxorubicin-loaded liposomes determined from HPLC analysis of doxorubicin in resected tumors (Figure 2-6).

The tail region is selected to ensure it is sufficiently far from the tail vein injection site so as not to have interference from residues left from any injection abnormalities. The tail is a region with a large vein and as such this region is representative of the concentration of liposome in blood (Figure 4-2A). Similar to the trend for liposomal doxorubicin determined in Chapter 2, this sees an initial decrease to roughly half at 2 h followed by a more gradual decrease through the elimination phase.

Similarly, the total intensity from the tumor (Figure 4-2B) follows the same general trend as for the tumor accumulation of liposomal doxorubicin (Chapter 2). Here, the accumulation at 30 min is roughly half of the accumuation reached at 24 h with the maximum seeming to appear between 6 h and 24 h.

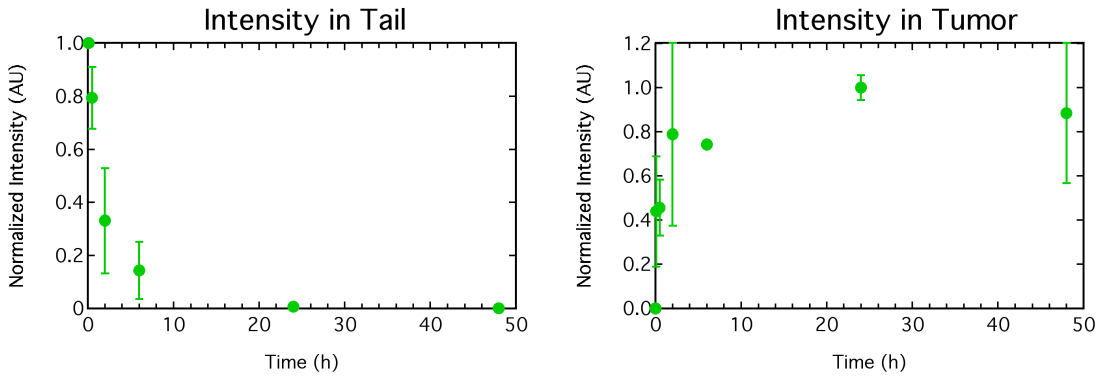

Figure 4-2. Evaluation of NIR liposome intensity in mice over 48 h.
(a) The intensity in the tail of the mice normalized to 1 at 5 min. (b) The intensity in the tumor normalized to 1 at the maximum intensity. Data represents mean ± SE, n=2.

At each time point, the NIR-liposome intensity is plotted vs. the anticipated quantitative data for the pharmacokinetic/tail image data (Figure 4-3A) and the tumor accumulation data (Figure 4-3B). In each case, the a linear fit is calculated with an intercept at zero, as would be expected for an ideal correlation between the semi-quantitative imaging data for NIR-dye loaded liposomes and the quantitative data from doxorubicin-loaded liposomes. The Pearson correlation coefficient between the fluorescence intensity obtained from whole body imaging and tumor accumulation from HPLC (Figure 4-3) is 0.95, suggesting that tumor accumulation can be obtained from imaging.

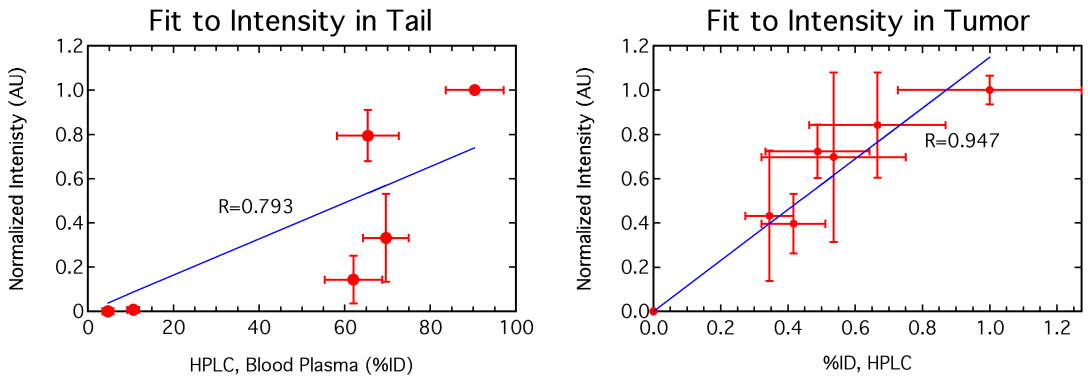

Figure 4-3. Calibration of NIR liposome data to quantitative HPLC data obtained from doxorubicin-loaded liposomes.

4.4 Future Work

This semi-quantiative imaging data provides a foundation for the use of dye-loaded nanoparticles for assessing tumor accumulation variations in nanomedicine optimization. This can provide a relatively expedient method to facilitate systematic nanomedicine development.

The next step in this work is to use dye-loaded liposomes to assess how liposome modification will affect nanomedicine efficiency. For example, in Chapter 3, we discussed the benefits of functionalizing liposomes with CD47 to aide the liposomes with evasion of the immune system. To rapidly test this theory *in vivo*, we recommend assessing biodistribution and tumor uptake of NIR-dye loaded liposomes with and without incorporation of CD47 in the lipid bilayer. If the CD47

does in fact facilitate immune system evasion, fluorescent intensity in the liver may be noticeably decreased while tumor intensity over time will be increased.

Additionally, whole body imaging has proven useful for comprehension of tumor variations. As discussed previously, this information would prove valuable in identifying a patient's tumor "leakiness" and consequently identifying the correct dosage for the patient. At present, NIR-dye is not FDA-approved; however, there are FDA-approved radiolabel-imaging agents. By adapting this model to incorporate a radiolabel in place of the dye, this platform could be used to identify patient-specific dosages for liposomal nanomedicines.

BIBLIOGRAPHY

1. Minchinton, A.I. and I.F. Tannock, *Drug penetration in solid tumours.* Nat Rev Cancer, 2006. **6**(8): p. 583-92.
2. Fang, J., H. Nakamura, and H. Maeda, *The EPR effect: Unique features of tumor blood vessels for drug delivery, factors involved, and limitations and augmentation of the effect.* Adv Drug Deliv Rev, 2011. **63**(3): p. 136-51.
3. Maeda, H., et al., *Tumor vascular permeability and the EPR effect in macromolecular therapeutics: a review.* Journal of Controlled Release, 2000. **65**(1-2): p. 271-284.
4. Matsumura, Y. and H. Maeda, *A new concept for macromolecular therapeutics in cancer chemotherapy: mechanism of tumoritropic accumulation of proteins and the antitumor agent smancs.* Cancer Res, 1986. **46**(12 Pt 1): p. 6387-92.
5. Dawidczyk, C.M., et al., *State-of-the-art in design rules for drug delivery platforms: lessons learned from FDA-approved nanomedicines.* J Control Release, 2014. **187**: p. 133-44.
6. Mullard, A., *Maturing antibody-drug conjugate pipeline hits 30.* Nat Rev Drug Discov, 2013. **12**(5): p. 329-32.
7. Sassoon, I. and V. Blanc, *Antibody-drug conjugate (ADC) clinical pipeline: a review.* Methods Mol Biol, 2013. **1045**: p. 1-27.
8. Sievers, E.L. and P.D. Senter, *Antibody-drug conjugates in cancer therapy.* Annu Rev Med, 2013. **64**: p. 15-29.
9. Lu, D., et al., *Drug interaction potential of trastuzumab emtansine (T-DM1) combined with pertuzumab in patients with HER2-positive metastatic breast cancer.* Curr Drug Metab, 2012. **13**(7): p. 911-22.
10. Verma, S., et al., *Trastuzumab emtansine for HER2-positive advanced breast cancer.* N Engl J Med, 2012. **367**(19): p. 1783-91.
11. Dawidczyk, C.M., L.M. Russell, and P.C. Searson, *Nanomedicines for cancer therapy: state-of-the-art and limitations to pre-clinical studies that hinder future developments.* Front Chem, 2014. **2**: p. 69.
12. Barenholz, Y., *Doxil(R)--the first FDA-approved nano-drug: lessons learned.* J Control Release, 2012. **160**(2): p. 117-34.
13. Furger, K.A., et al., *Beta(3) integrin expression increases breast carcinoma cell responsiveness to the malignancy-enhancing effects of osteopontin.* Mol Cancer Res, 2003. **1**(11): p. 810-9.
14. Gabizon, A., et al., *Prolonged circulation time and enhanced accumulation in malignant exudates of doxorubicin encapsulated in polyethylene-glycol coated liposomes.* Cancer Res, 1994. **54**(4): p. 987-92.
15. Lasic, D.D., et al., *Gelation of liposome interior. A novel method for drug encapsulation.* FEBS Lett, 1992. **312**(2-3): p. 255-8.

16. Immordino, M.L., F. Dosio, and L. Cattel, *Stealth liposomes: review of the basic science, rationale, and clinical applications, existing and potential.* Int J Nanomedicine, 2006. **1**(3): p. 297-315.
17. Vllasaliu, D., R. Fowler, and S. Stolnik, *PEGylated nanomedicines: recent progress and remaining concerns.* Expert Opinion on Drug Delivery, 2014. **11**(1): p. 139-154.
18. Seynhaeve, A.L.B., et al., *Intact Doxil is taken up intracellularly and released doxorubicin sequesters in the lysosome: Evaluated by in vitro/in vivo live cell imaging.* Journal of Controlled Release, 2013. **172**(1): p. 330-340.
19. Bellott, R., et al., *Pharmacokinetics of liposomal daunorubicin [DaunoXome] during a phase I-II study in children with relapsed acute lymphoblastic leukaemia.* Cancer Chemotherapy and Pharmacology, 2001. **47**(1): p. 15-21.
20. Gill, P.S., et al., *Randomized phase III trial of liposomal daunorubicin versus doxorubicin, bleomycin, and vincristine in AIDS-related Kaposi's sarcoma.* J Clin Oncol, 1996. **14**(8): p. 2353-2364.
21. Lowis, S., et al., *A phase I study of intravenous liposomal daunorubicin (DaunoXome) in paediatric patients with relapsed or resistant solid tumours.* Br J Cancer, 2006. **95**(5): p. 571-80.
22. Bedikian, A.Y., et al., *Pharmacokinetics and Safety of Marqibo (Vincristine Sulfate Liposomes Injection) in Cancer Patients With Impaired Liver Function.* Journal of Clinical Pharmacology, 2011. **51**(8): p. 1205-1212.
23. Silverman, J.A. and S.R. Deitcher, *Marqibo(R) (vincristine sulfate liposome injection) improves the pharmacokinetics and pharmacodynamics of vincristine.* Cancer Chemother Pharmacol, 2013. **71**(3): p. 555-564.
24. Miele, E., et al., *Albumin-bound formulation of paclitaxel (Abraxane ABI-007) in the treatment of breast cancer.* Int J Nanomedicine, 2009. **4**: p. 99-105.
25. Yardley, D.A., *nab-Paclitaxel mechanisms of action and delivery.* J Control Release, 2013. **170**(3): p. 365-72.
26. Bradley, A.M., M. Devine, and D. DeRemer, *Brentuximab vedotin: An anti-CD30 antibody-drug conjugate.* American Journal of Health-System Pharmacy, 2013. **70**(7): p. 589-597.
27. Girish, S., et al., *Clinical pharmacology of trastuzumab emtansine (T-DM1): an antibody-drug conjugate in development for the treatment of HER2-positive cancer.* Cancer Chemotherapy and Pharmacology, 2012. **69**(5): p. 1229-1240.
28. LoRusso, P.M., et al., *Trastuzumab Emtansine: A Unique Antibody-Drug Conjugate in Development for Human Epidermal Growth Factor Receptor 2-Positive Cancer.* Clinical Cancer Research, 2011. **17**(20): p. 6437-6447.
29. Younes, A., et al., *Brentuximab vedotin (SGN-35) for relapsed CD30-positive lymphomas.* N Engl J Med, 2010. **363**(19): p. 1812-21.
30. Hamilton, A., et al., *EORTC 10968: a phase I clinical and pharmacokinetic study of polyethylene glycol liposomal doxorubicin (Caelyx, Doxil) at a 6-week interval in patients with metastatic breast cancer. European Organization for Research and Treatment of Cancer.* Ann Oncol, 2002. **13**(6): p. 910-8.
31. Hong, R.L. and Y.L. Tseng, *Phase I and pharmacokinetic study of a stable, polyethylene-glycolated liposomal doxorubicin in patients with solid tumors:*

the relation between pharmacokinetic property and toxicity. Cancer, 2001. **91**(9): p. 1826-33.
32. Hubert, A., et al., *Doxil (Caelyx): an exploratory study with pharmacokinetics in patients with hormone-refractory prostate cancer.* Anticancer Drugs, 2000. **11**(2): p. 123-7.
33. Lyass, O., et al., *Correlation of toxicity with pharmacokinetics of pegylated liposomal doxorubicin (Doxil) in metastatic breast carcinoma.* Cancer, 2000. **89**(5): p. 1037-47.
34. Ando, M., et al., *Phase I and pharmacokinetic study of nab-paclitaxel, nanoparticle albumin-bound paclitaxel, administered weekly to Japanese patients with solid tumors and metastatic breast cancer.* Cancer Chemother Pharmacol, 2012. **69**(2): p. 457-65.
35. Sparreboom, A., et al., *Comparative preclinical and clinical pharmacokinetics of a cremophor-free, nanoparticle albumin-bound paclitaxel (ABI-007) and paclitaxel formulated in Cremophor (Taxol).* Clin Cancer Res, 2005. **11**(11): p. 4136-43.
36. Erttmann, R., et al., *Pharmacokinetics of doxorubicin in man: dose and schedule dependence.* J Cancer Res Clin Oncol, 1988. **114**(5): p. 509-13.
37. Jacquet, J.M., et al., *Doxorubicin and doxorubicinol: intra- and inter-individual variations of pharmacokinetic parameters.* Cancer Chemother Pharmacol, 1990. **27**(3): p. 219-225.
38. Piscitelli, S.C., et al., *Pharmacokinetics and pharmacodynamics of doxorubicin in patients with small cell lung cancer.* Clin Pharmacol Ther, 1993. **53**(5): p. 555-561.
39. Krogh-Madsen, M., et al., *Population pharmacokinetics of cytarabine, etoposide, and daunorubicin in the treatment for acute myeloid leukemia.* Cancer Chemother Pharmacol, 2012. **69**(5): p. 1155-63.
40. Hanahan, D. and R.A. Weinberg, *Hallmarks of cancer: the next generation.* Cell, 2011. **144**(5): p. 646-74.
41. Huynh, N.T., et al., *The rise and rise of stealth nanocarriers for cancer therapy: passive versus active targeting.* Nanomedicine (Lond), 2010. **5**(9): p. 1415-33.
42. Arruebo, M., M. Valladares, and A. Gonzalez-Fernandez, *Antibody-Conjugated Nanoparticles for Biomedical Applications.* Journal of Nanomaterials, 2009.
43. Chames, P., et al., *Therapeutic antibodies: successes, limitations and hopes for the future.* British Journal of Pharmacology, 2009. **157**(2): p. 220-233.
44. Dill, K., et al., *Antibody-Antigen Binding Constants Determined in Solution-Phase with the Threshold Membrane-Capture System - Binding Constants for Antifluorescein, Anti-Saxitoxin, and Anti-Ricin Antibodies.* Analytical Biochemistry, 1994. **217**(1): p. 128-138.
45. Holliger, P. and P.J. Hudson, *Engineered antibody fragments and the rise of single domains.* Nature Biotechnology, 2005. **23**(9): p. 1126-1136.
46. Hu, M. and K. Zhang, *The application of aptamers in cancer research: an up-to-date review.* Future Oncology, 2013. **9**(3): p. 369-376.
47. Keefe, A.D., S. Pai, and A. Ellington, *Aptamers as therapeutics.* Nature Reviews Drug Discovery, 2010. **9**(7): p. 537-550.

48. Jain, R.K., *Normalization of tumor vasculature: An emerging concept in antiangiogenic therapy.* Science, 2005. **307**(5706): p. 58-62.
49. Lupold, S.E., et al., *Identification and Characterization of Nuclease-Stabilized RNA Molecules That Bind Human Prostate Cancer Cells via the Prostate-Specific Membrane Antigen.* Cancer Research, 2002. **62**(14): p. 4029-4033.
50. Banerjee, S.R., et al., *Synthesis and evaluation of technetium-99m-and rhenium-labeled inhibitors of the prostate-specific membrane antigen (PSMA).* Journal of Medicinal Chemistry, 2008. **51**(15): p. 4504-4517.
51. Hsu, C.W., et al., *Comparative Therapeutic Efficacy of Rhenium-188 Radiolabeled-Liposome and 5-Fluorouracil in LS-174T Human Colon Carcinoma Solid Tumor Xenografts.* Cancer Biotherapy and Radiopharmaceuticals, 2012. **27**(8): p. 481-489.
52. Sun, X.L., et al., *Self-illuminating Cu-64-Doped CdSe/ZnS Nanocrystals for in Vivo Tumor Imaging.* Journal of the American Chemical Society, 2014. **136**(5): p. 1706-1709.
53. Penate Medina, O., et al., *Liposomal Tumor Targeting in Drug Delivery Utilizing MMP-2- and MMP-9-Binding Ligands.* J Drug Deliv, 2011. **2011**: p. 160515.
54. Morales-Avila, E., et al., *Multimeric system of 99mTc-labeled gold nanoparticles conjugated to c[RGDfK(C)] for molecular imaging of tumor alpha(v)beta(3) expression.* Bioconjug Chem, 2011. **22**(5): p. 913-22.
55. Cekanova, M. and K. Rathore, *Animal models and therapeutic molecular targets of cancer: utility and limitations.* Drug Des Devel Ther, 2014. **8**: p. 1911-21.
56. Denayer, T., T. Stöhr, and M. VanRoy, *Animal models in translational medicine: Validation and prediction.* New Horizons in Translational Medicine, 2014. **2**: p. 5-11.
57. Aulino, P., et al., *Molecular, cellular and physiological characterization of the cancer cachexia-inducing C26 colon carcinoma in mouse.* BMC Cancer, 2010. **10**: p. 363.
58. Masters, J.R., *False cell lines: The problem and a solution.* Cytotechnology, 2002. **39**(2): p. 69-74.
59. Dupre, S.A., D. Redelman, and K.W. Hunter, *Microenvironment of the murine mammary carcinoma 4T1: Endogenous IFN-gamma affects tumor phenotype, growth, and metastasis.* Experimental and Molecular Pathology, 2008. **85**(3): p. 174-188.
60. Pulaski, B.A. and S. Ostrand-Rosenberg, *Mouse 4T1 Breast Tumor Model*, in *Current Protocols in Immunology*. 2000, John Wiley & Sons, Inc. p. 20.2.1-16.
61. Hobbs, S.K., et al., *Regulation of transport pathways in tumor vessels: Role of tumor type and microenvironment.* Proceedings of the National Academy of Sciences of the United States of America, 1998. **95**(8): p. 4607-4612.
62. Folkman, J., *What Is the Evidence That Tumors Are Angiogenesis Dependent.* Journal of the National Cancer Institute, 1990. **82**(1): p. 4-6.
63. Adiseshaiah, P.P., J.B. Hall, and S.E. McNeil, *Nanomaterial standards for efficacy and toxicity assessment.* Wiley Interdiscip Rev Nanomed Nanobiotechnol, 2010. **2**(1): p. 99-112.

64. Hall, J.B., et al., *Characterization of nanoparticles for therapeutics.* Nanomedicine, 2007. **2**(6): p. 789-803.
65. McNeil, S.E., *Nanotechnology for the biologist.* J Leukoc Biol, 2005. **78**(3): p. 585-94.
66. Kobayashi, H., Y. Takemura, and T. Ohnuma, *Relationship between tumor cell density and drug concentration and the cytotoxic effects of doxorubicin or vincristine: mechanism of inoculum effects.* Cancer Chemother Pharmacol, 1992. **31**(1): p. 6-10.
67. Agarwal, R., et al., *Mammalian cells preferentially internalize hydrogel nanodiscs over nanorods and use shape-specific uptake mechanisms.* Proc Natl Acad Sci USA, 2013. **110**(43): p. 17247-52.
68. Barua, S., et al., *Particle shape enhances specificity of antibody-displaying nanoparticles.* Proc Natl Acad Sci USA, 2013. **110**(9): p. 3270-5.
69. Furumoto, K., et al., *Hepatic uptake of negatively charged particles in rats: possible involvement of serum proteins in recognition by scavenger receptor.* J Control Release, 2004. **97**(1): p. 133-41.
70. Ogawara, K., et al., *Hepatic uptake of polystyrene microspheres in rats: effect of particle size on intrahepatic distribution.* J Control Release, 1999. **59**(1): p. 15-22.
71. Ogawara, K., et al., *Mechanisms of hepatic disposition of polystyrene microspheres in rats: effects of serum depend on the sizes of microspheres.* J Control Release, 1999. **61**(3): p. 241-50.
72. Yokoyama, M., et al., *Selective delivery of adiramycin to a solid tumor using a polymeric micelle carrier system.* Journal of Drug Targeting, 1999. **7**(3): p. 171-186.
73. Hoang, B., et al., *Noninvasive Monitoring of the Fate of In-111-Labeled Block Copolymer Micelles by High Resolution and High Sensitivity MicroSPECT/CT Imaging.* Molecular Pharmaceutics, 2009. **6**(2): p. 581-592.
74. Robinson, J.T., et al., *In Vivo Fluorescence Imaging in the Second Near-Infrared Window with Long Circulating Carbon Nanotubes Capable of Ultrahigh Tumor Uptake.* Journal of the American Chemical Society, 2012. **134**(25): p. 10664-10669.
75. Balogh, L., et al., *Significant effect of size on the in vivo biodistribution of gold composite nanodevices in mouse tumor models.* Nanomedicine-Nanotechnology Biology and Medicine, 2007. **3**(4): p. 281-296.
76. Paraskar, A., et al., *Rationally designed oxaliplatin-nanoparticle for enhanced antitumor efficacy.* Nanotechnology, 2012. **23**(7).
77. Sumitani, S., M. Oishi, and Y. Nagasaki, *Carborane confined nanoparticles for boron neutron capture therapy: Improved stability, blood circulation time and tumor accumulation.* Reactive & Functional Polymers, 2011. **71**(7): p. 684-693.
78. Zhu, H., et al., *Design, Synthesis and Evaluation of Dual-Modality Glyco-Nanoparticles for Tumor Imaging.* Molecules, 2013. **18**(6): p. 6425-6438.
79. Zhao, J., et al., *Dual-Modal Tumor Imaging via Long-Circulating Biodegradable Core-Cross-Linked Polymeric Micelles.* Acs Macro Letters, 2012. **1**(1): p. 150-153.

80. Rijcken, C.J., et al., *Hydrolysable core-crosslinked thermosensitive polymeric micelles: Synthesis, characterisation and in vivo studies.* Biomaterials, 2007. **28**(36): p. 5581-5593.
81. Coimbra, M., et al., *Antitumor efficacy of dexamethasone-loaded core-crosslinked polymeric micelles.* Journal of Controlled Release, 2012. **163**(3): p. 361-367.
82. Chen, M., et al., *Polypyrrole nanoparticles for high-performance in vivo near-infrared photothermal cancer therapy.* Chemical Communications, 2012. **48**(71): p. 8934-8936.
83. Yang, K., et al., *Multimodal Imaging Guided Photothermal Therapy using Functionalized Graphene Nanosheets Anchored with Magnetic Nanoparticles.* Advanced Materials, 2012. **24**(14): p. 1868-1872.
84. Rong, P.F., et al., *Photosensitizer Loaded Nano-Graphene for Multimodality Imaging Guided Tumor Photodynamic Therapy.* Theranostics, 2014. **4**(3): p. 229-239.
85. Ohno, K., et al., *Fabrication of Contrast Agents for Magnetic Resonance Imaging from Polymer-Brush-Afforded Iron Oxide Magnetic Nanoparticles Prepared by Surface-Initiated Living Radical Polymerization.* Biomacromolecules, 2013. **14**(10): p. 3453-3462.
86. Harrington, K.J., et al., *Influence of tumour size on uptake of In-111-DTPA-labelled pegylated liposomes in a human tumour xenograft model.* British Journal of Cancer, 2000. **83**(5): p. 684-688.
87. Huang, F.Y.J., et al., *Imaging, Autoradiography, and Biodistribution of Re-188-Labeled PEGylated Nanoliposome in Orthotopic Glioma Bearing Rat Model.* Cancer Biotherapy and Radiopharmaceuticals, 2011. **26**(6): p. 717-725.
88. Zheng, J., D. Jaffray, and C. Allien, *Quantitative CT Imaging of the Spatial and Temporal Distribution of Liposomes in a Rabbit Tumor Model.* Molecular Pharmaceutics, 2009. **6**(2): p. 571-580.
89. Chen, L.C., et al., *Pharmacokinetics, dosimetry and comparative efficacy of Re-188-liposome and 5-FU in a CT26-luc lung-metastatic mice model.* Nuclear Medicine and Biology, 2012. **39**(1): p. 35-43.
90. Soundararajan, A., et al., *[Re-186]Liposomal doxorubicin (Doxil): in vitro stability, pharmacokinetics, imaging and biodistribution in a head and neck squamous cell carcinoma xenograft model.* Nuclear Medicine and Biology, 2009. **36**(5): p. 515-524.
91. Kheirolomoom, A., et al., *Copper-Doxorubicin as a Nanoparticle Cargo Retains Efficacy with Minimal Toxicity.* Molecular Pharmaceutics, 2010. **7**(6): p. 1948-1958.
92. Mahakian, L.M., et al., *Comparison of PET Imaging with Cu-64-Liposomes and F-18-FDG in the 7,12-Dimethylbenz[a]anthracene (DMBA)-Induced Hamster Buccal Pouch Model of Oral Dysplasia and Squamous Cell Carcinoma.* Molecular Imaging and Biology, 2014. **16**(2): p. 284-292.
93. Wang, H.E., et al., *Internal radiotherapy and dosimetric study for In-111/Lu-177-pegylated liposomes conjugates in tumor-bearing mice.* Nuclear Instruments & Methods in Physics Research Section a-Accelerators

Spectrometers Detectors and Associated Equipment, 2006. **569**(2): p. 533-537.
94. Di Pasqua, A.J., et al., *Tumor accumulation of neutron-activatable holmium-containing mesoporous silica nanoparticles in an orthotopic non-small cell lung cancer mouse model.* Inorganica Chimica Acta, 2012. **393**: p. 334-336.
95. Blanco, E., et al., *beta-Lapachone Micellar Nanotherapeutics for Non-Small Cell Lung Cancer Therapy.* Cancer Research, 2010. **70**(10): p. 3896-3904.
96. Reddy, L.H., R.K. Sharma, and R.R. Murthy, *Enhanced delivery of etoposide to Dalton's lymphoma in mice through polysorbate 20 micelles.* Acta Pharm, 2006. **56**(2): p. 143-55.
97. Wang, M. and A.L. Gartel, *Micelle-Encapsulated Thiostrepton as an Effective Nanomedicine for Inhibiting Tumor Growth and for Suppressing FOXM1 in Human Xenografts.* Molecular Cancer Therapeutics, 2011. **10**(12): p. 2287-2297.
98. Miller, T., et al., *Premature drug release of polymeric micelles and its effects on tumor targeting.* International Journal of Pharmaceutics, 2013. **445**(1-2): p. 117-124.
99. Kawano, K., et al., *Enhanced antitumor effect of camptothecin loaded in long-circulating polymeric micelles.* Journal of Controlled Release, 2006. **112**(3): p. 329-332.
100. Hainfeld, J.F., et al., *Gold nanoparticles: a new X-ray contrast agent.* British Journal of Radiology, 2006. **79**(939): p. 248-253.
101. Ujiie, K., et al., *Preparation of highly dispersible and tumor-accumulative, iron oxide nanoparticles Multi-point anchoring of PEG-b-poly(4-vinylbenzylphosphonate) improves performance significantly.* Colloids and Surfaces B-Biointerfaces, 2011. **88**(2): p. 771-778.
102. von Maltzahn, G., et al., *Computationally Guided Photothermal Tumor Therapy Using Long-Circulating Gold Nanorod Antennas.* Cancer Research, 2009. **69**(9): p. 3892-3900.
103. Puvanakrishnan, P., et al., *In vivo tumor targeting of gold nanoparticles: effect of particle type and dosing strategy.* International Journal of Nanomedicine, 2012. **7**: p. 1251-1258.
104. Tinkov, S., et al., *New doxorubicin-loaded phospholipid microbubbles for targeted tumor therapy: In-vivo characterization.* Journal of Controlled Release, 2010. **148**(3): p. 368-372.
105. Kim, S.H., et al., *Local and systemic delivery of VEGF siRNA using polyelectrolyte complex micelles for effective treatment of cancer.* Journal of Controlled Release, 2008. **129**(2): p. 107-116.
106. Le Garrec, D., et al., *Optimizing pH-responsive polymeric micelles for drug delivery in a cancer photodynamic therapy model.* Journal of Drug Targeting, 2002. **10**(5): p. 429-437.
107. Shiraishi, K., et al., *Preparation and in vivo imaging of PEG-poly(L-lysine)-based polymeric micelle MRI contrast agents.* Journal of Controlled Release, 2009. **136**(1): p. 14-20.

108. Liu, X.W., et al., *Optimization of surface chemistry on single-walled carbon nanotubes for in vivo photothermal ablation of tumors.* Biomaterials, 2011. **32**(1): p. 144-151.
109. Hong, H., et al., *In vivo targeting and imaging of tumor vasculature with radiolabeled, antibody-conjugated nanographene.* ACS Nano, 2012. **6**(3): p. 2361-70.
110. Cornelissen, B., et al., *Nanographene oxide-based radioimmunoconstructs for in vivo targeting and SPECT imaging of HER2-positive tumors.* Biomaterials, 2013. **34**(4): p. 1146-54.
111. Shi, S., et al., *Tumor vasculature targeting and imaging in living mice with reduced graphene oxide.* Biomaterials, 2013. **34**(12): p. 3002-9.
112. Melancon, M.P., et al., *In vitro and in vivo targeting of hollow gold nanoshells directed at epidermal growth factor receptor for photothermal ablation therapy.* Mol Cancer Ther, 2008. **7**(6): p. 1730-9.
113. Lu, W., et al., *Targeted photothermal ablation of murine melanomas with melanocyte-stimulating hormone analog-conjugated hollow gold nanospheres.* Clin Cancer Res, 2009. **15**(3): p. 876-86.
114. Lu, W., et al., *Tumor site-specific silencing of NF-kappaB p65 by targeted hollow gold nanosphere-mediated photothermal transfection.* Cancer Res, 2010. **70**(8): p. 3177-88.
115. Petersen, A.L., et al., *Positron emission tomography evaluation of somatostatin receptor targeted 64Cu-TATE-liposomes in a human neuroendocrine carcinoma mouse model.* J Control Release, 2012. **160**(2): p. 254-63.
116. Iyer, A.K., et al., *The effect of internalizing human single chain antibody fragment on liposome targeting to epithelioid and sarcomatoid mesothelioma.* Biomaterials, 2011. **32**(10): p. 2605-13.
117. Helbok, A., et al., *Targeting properties of peptide-modified radiolabeled liposomal nanoparticles.* Nanomedicine, 2012. **8**(1): p. 112-8.
118. Chen, F., et al., *In vivo tumor targeting and image-guided drug delivery with antibody-conjugated, radiolabeled mesoporous silica nanoparticles.* ACS Nano, 2013. **7**(10): p. 9027-39.
119. Fonge, H., et al., *Influence of formulation variables on the biodistribution of multifunctional block copolymer micelles.* J Control Release, 2012. **157**(3): p. 366-74.
120. Hu, Z., et al., *Arg-Gly-Asp (RGD) peptide conjugated poly(lactic acid)-poly(ethylene oxide) micelle for targeted drug delivery.* J Biomed Mater Res A, 2008. **85**(3): p. 797-807.
121. Zhang, R., et al., *Peptide-conjugated polymeric micellar nanoparticles for Dual SPECT and optical imaging of EphB4 receptors in prostate cancer xenografts.* Biomaterials, 2011. **32**(25): p. 5872-9.
122. Zhang, R., et al., *Annexin A5-conjugated polymeric micelles for dual SPECT and optical detection of apoptosis.* J Nucl Med, 2011. **52**(6): p. 958-64.
123. Zhan, C., et al., *Cyclic RGD conjugated poly(ethylene glycol)-co-poly(lactic acid) micelle enhances paclitaxel anti-glioblastoma effect.* J Control Release, 2010. **143**(1): p. 136-42.

124. Poon, Z., et al., *Highly stable, ligand-clustered "patchy" micelle nanocarriers for systemic tumor targeting.* Nanomedicine, 2011. **7**(2): p. 201-9.
125. Xiao, Y., et al., *Multifunctional unimolecular micelles for cancer-targeted drug delivery and positron emission tomography imaging.* Biomaterials, 2012. **33**(11): p. 3071-82.
126. Cheng, K., et al., *Construction and Validation of Nano Gold Tripods for Molecular Imaging of Living Subjects.* Journal of the American Chemical Society, 2014. **136**(9): p. 3560-3571.
127. Ohguchi, Y., et al., *Selective delivery of folate-PEG-linked, nanoemulsion-loaded aclacinomycin A to KB nasopharyngeal cells and xenograft: effect of chain length and amount of folate-PEG linker.* J Drug Target, 2008. **16**(9): p. 660-7.
128. Oyewumi, M.O., et al., *Comparison of cell uptake, biodistribution and tumor retention of folate-coated and PEG-coated gadolinium nanoparticles in tumor-bearing mice.* J Control Release, 2004. **95**(3): p. 613-26.
129. Benezra, M., et al., *Multimodal silica nanoparticles are effective cancer-targeted probes in a model of human melanoma.* J Clin Invest, 2011. **121**(7): p. 2768-80.
130. Kumar, M., et al., *Image-guided breast tumor therapy using a small interfering RNA nanodrug.* Cancer Res, 2010. **70**(19): p. 7553-61.
131. Chanda, N., et al., *Bombesin functionalized gold nanoparticles show in vitro and in vivo cancer receptor specificity.* Proc Natl Acad Sci U S A, 2010. **107**(19): p. 8760-5.
132. Choi, C.H., et al., *Mechanism of active targeting in solid tumors with transferrin-containing gold nanoparticles.* Proc Natl Acad Sci U S A, 2010. **107**(3): p. 1235-40.
133. Tang, L., et al., *Aptamer-functionalized, ultra-small, monodisperse silica nanoconjugates for targeted dual-modal imaging of lymph nodes with metastatic tumors.* Angew Chem Int Ed Engl, 2012. **51**(51): p. 12721-6.
134. Chattopadhyay, N., et al., *Role of antibody-mediated tumor targeting and route of administration in nanoparticle tumor accumulation in vivo.* Mol Pharm, 2012. **9**(8): p. 2168-79.
135. Kunjachan, S., et al., *Passive versus active tumor targeting using RGD- and NGR-modified polymeric nanomedicines.* Nano Lett, 2014. **14**(2): p. 972-81.
136. Gao, J., et al., *In vivo tumor-targeted fluorescence imaging using near-infrared non-cadmium quantum dots.* Bioconjug Chem, 2010. **21**(4): p. 604-9.
137. Rossin, R., et al., *64Cu-labeled folate-conjugated shell cross-linked nanoparticles for tumor imaging and radiotherapy: synthesis, radiolabeling, and biologic evaluation.* J Nucl Med, 2005. **46**(7): p. 1210-8.
138. Khemtong, C., et al., *In vivo off-resonance saturation magnetic resonance imaging of alphavbeta3-targeted superparamagnetic nanoparticles.* Cancer Res, 2009. **69**(4): p. 1651-8.
139. Yang, X., et al., *cRGD-functionalized, DOX-conjugated, and (6)(4)Cu-labeled superparamagnetic iron oxide nanoparticles for targeted anticancer drug delivery and PET/MR imaging.* Biomaterials, 2011. **32**(17): p. 4151-60.

140. Natarajan, A., et al., *NanoFerrite particle based radioimmunonanoparticles: binding affinity and in vivo pharmacokinetics.* Bioconjug Chem, 2008. **19**(6): p. 1211-8.
141. Bangham, A.D. and R.W. Horne, *Negative staining of phospholipids and their structural modification by surface-active agents as observed in the electron microscope.* J Mol Biol, 1964. **8**: p. 660-8.
142. Bangham, A.D., M.M. Standish, and J.C. Watkins, *Diffusion of univalent ions across the lamellae of swollen phospholipids.* J Mol Biol, 1965. **13**(1): p. 238-52.
143. Klibanov, A.L., et al., *Amphipathic polyethyleneglycols effectively prolong the circulation time of liposomes.* FEBS Lett, 1990. **268**(1): p. 235-7.
144. Gibaldi, M. and D. Perrier, *Pharmacokinetics.* 3rd ed. Drugs and the Pharmaceutical Sciences, ed. J. Swarbrick. 2006: Marcel Dekker, Inc.
145. Gordon, A.N., et al., *Recurrent epithelial ovarian carcinoma: a randomized phase III study of pegylated liposomal doxorubicin versus topotecan.* J Clin Oncol, 2001. **19**(14): p. 3312-22.
146. Jiang, W., R. Lionberger, and L.X. Yu, *In vitro and in vivo characterizations of PEGylated liposomal doxorubicin.* Bioanalysis, 2011. **3**(3): p. 333-44.
147. Barenholz, Y., *Doxil(R)-the first FDA-approved nano-drug: lessons learned.* J Control Release, 2012. **160**(2): p. 117-34.
148. Gabizon, A., et al., *Prolonged Circulation Time and Enhanced Accumulation in Malignant Exudates of Doxorubicin Encapsulated in Polyethylene-Glycol Coated Liposomes.* Cancer Research, 1994. **54**(4): p. 987-992.
149. Gabizon, A., H. Shmeeda, and Y. Barenholz, *Pharmacokinetics of pegylated liposomal doxorubicin - Review of animal and human studies.* Clinical Pharmacokinetics, 2003. **42**(5): p. 419-436.
150. Gabizon, A., et al., *Development of liposomal anthracyclines: from basics to clinical applications.* Journal of Controlled Release, 1998. **53**(1-3): p. 275-279.
151. Torchilin, V., *Tumor delivery of macromolecular drugs based on the EPR effect.* Adv Drug Deliv Rev, 2011. **63**(3): p. 131-5.
152. Torchilin, V.P., *Recent advances with liposomes as pharmaceutical carriers.* Nature Reviews Drug Discovery, 2005. **4**(2): p. 145-160.
153. Cheng, W.W. and T.M. Allen, *The use of single chain Fv as targeting agents for immunoliposomes: an update on immunoliposomal drugs for cancer treatment.* Expert Opinion on Drug Delivery, 2010. **7**(4): p. 461-478.
154. Drummond, D.C., et al., *Optimizing liposomes for delivery of chemotherapeutic agents to solid tumors.* Pharmacological Reviews, 1999. **51**(4): p. 691-743.
155. Harrington, K.J., et al., *Effective targeting of solid tumors in patients with locally advanced cancers by radiolabeled pegylated liposomes.* Clinical Cancer Research, 2001. **7**(2): p. 243-254.
156. Paszko, E. and M.O. Senge, *Immunoliposomes.* Curr Med Chem, 2012. **19**(31): p. 5239-77.
157. Saltzman, W.M., *Drug Delivery: Engineering Principles for Drug Therapy*. Topics in Chemical Engineering, ed. K.E. Gubbins. 2001, 198 Madison Avenue, New York, New York 10016: Oxford University Press.
158. Wong, A.D., et al., *Quantitative Analysis of the Enhanced Permeation and Retention (EPR) Effect.* PLoS One, 2015. **10**(5): p. e0123461.

159. Chabner, B.A. and T.G. Roberts, Jr., *Timeline: Chemotherapy and the war on cancer.* Nat Rev Cancer, 2005. **5**(1): p. 65-72.
160. DeVita, V.T., Jr. and E. Chu, *A history of cancer chemotherapy.* Cancer Res, 2008. **68**(21): p. 8643-53.
161. Brigger, I., C. Dubernet, and P. Couvreur, *Nanoparticles in cancer therapy and diagnosis.* Adv Drug Deliv Rev, 2002. **54**(5): p. 631-51.
162. Cheng, Z., et al., *Multifunctional nanoparticles: cost versus benefit of adding targeting and imaging capabilities.* Science, 2012. **338**(6109): p. 903-10.
163. Davis, M.E., Z. Chen, and D.M. Shin, *Nanoparticle therapeutics: an emerging treatment modality for cancer.* Nature Reviews Drug Discovery, 2008. **7**(9): p. 771-782.
164. Peer, D., et al., *Nanocarriers as an emerging platform for cancer therapy.* Nat Nanotechnol, 2007. **2**(12): p. 751-60.
165. Shen, B.Q., et al., *Conjugation site modulates the in vivo stability and therapeutic activity of antibody-drug conjugates.* Nat Biotechnol, 2012. **30**(2): p. 184-9.
166. Yu, M.K., J. Park, and S. Jon, *Targeting strategies for multifunctional nanoparticles in cancer imaging and therapy.* Theranostics, 2012. **2**(1): p. 3-44.
167. Gibaldi, M. and D. Perrier, *Pharmacokinetics*. 3rd ed. Drugs and the pharmaceutical sciences. 2006, New York: Dekker.
168. Dawidczyk, C.M., et al., *State-of-the-art in design rules for drug delivery platforms: Lessons learned from FDA-approved nanomedicines.* Journal of Controlled Release, 2014. **187**: p. 133-144.
169. Wong, A.D., et al., *Quantitative analysis of the enhanced ermeation and retention (EPR) effect.* PLoS One, 2015. **10**(5): p. e0123461.
170. Jain, R.K., *Transport of Molecules in the Tumor Interstitium - a Review.* Cancer Research, 1987. **47**(12): p. 3039-3051.
171. Jain, R.K., *Determinants of Tumor Blood-Flow - A Review.* Cancer Research, 1988. **48**(10): p. 2641-2658.
172. Maeda, H., H. Nakamura, and J. Fang, *The EPR effect for macromolecular drug delivery to solid tumors: Improvement of tumor uptake, lowering of systemic toxicity, and distinct tumor imaging in vivo.* Adv Drug Deliv Rev, 2013. **65**(1): p. 71-9.
173. Maeda, H. and Y. Matsumura, *EPR effect based drug design and clinical outlook for enhanced cancer chemotherapy.* Adv Drug Deliv Rev, 2011. **63**(3): p. 129-30.
174. Maeda, H., G.Y. Bharate, and J. Daruwalla, *Polymeric drugs for efficient tumor-targeted drug delivery based on EPR-effect.* Eur J Pharm Biopharm, 2009. **71**(3): p. 409-19.
175. Yuan, F., et al., *Vascular permeability in a human tumor xenograft: molecular size dependence and cutoff size.* Cancer Res, 1995. **55**(17): p. 3752-6.
176. Peer, D., et al., *Nanocarriers as an emerging platform for cancer therapy.* Nature Nanotechnology, 2007. **2**(12): p. 751-760.
177. Folkman, J. and P.A. DAmore, *Blood vessel formation: What is its molecular basis?* Cell, 1996. **87**(7): p. 1153-1155.

178. Yuan, F., et al., *Microvascular permeability and interstitial penetration of sterically stabilized (stealth) liposomes in a human tumor xenograft.* Cancer Res, 1994. **54**(13): p. 3352-6.
179. Yuan, F., et al., *Vascular permeability and microcirculation of gliomas and mammary carcinomas transplanted in rat and mouse cranial windows.* Cancer Res, 1994. **54**(17): p. 4564-8.
180. Dreher, M.R., et al., *Tumor vascular permeability, accumulation, and penetration of macromolecular drug carriers.* Journal of the National Cancer Institute, 2006. **98**(5): p. 335-344.
181. Swenson, C.E., et al., *Pharmacokinetics of doxorubicin administered i.v. as Myocet (TLC D-99; liposome-encapsulated doxorubicin citrate) compared with conventional doxorubicin when given in combination with cyclophosphamide in patients with metastatic breast cancer.* Anticancer Drugs, 2003. **14**(3): p. 239-46.
182. Longmire, M., P.L. Choyke, and H. Kobayashi, *Clearance properties of nano-sized particles and molecules as imaging agents: considerations and caveats.* Nanomedicine (Lond), 2008. **3**(5): p. 703-17.
183. Yu, M. and J. Zheng, *Clearance Pathways and Tumor Targeting of Imaging Nanoparticles.* ACS Nano, 2015. **9**(7): p. 6655-74.
184. Maeda, H., *Vascular permeability in cancer and infection as related to macromolecular drug delivery, with emphasis on the EPR effect for tumor-selective drug targeting.* Proc Jpn Acad Ser B Phys Biol Sci, 2012. **88**(3): p. 53-71.
185. Knop, K., et al., *Poly(ethylene glycol) in Drug Delivery: Pros and Cons as Well as Potential Alternatives.* Angewandte Chemie-International Edition, 2010. **49**(36): p. 6288-6308.
186. Hu, C.-M.J., et al., *Polymeric nanotherapeutics: clinical development and advances in stealth functionalization strategies.* Nanoscale, 2013. **6**(1): p. 65-75.
187. Hu, C.-M.J., et al., *Erythrocyte membrane-camouflaged polymeric nanoparticles as a biomimetic delivery platform.* Proceedings of the National Academy of Sciences, 2011.
188. Kevin, N., *'Marker-of-self'functionalization of nanoscale particles through a top-down cellular membrane coating approach.* Nanoscale, 2013. **5**(7): p. 2664-2668.
189. Gao, W., et al., *Surface functionalization of gold nanoparticles with red blood cell membranes.* Advanced Materials, 2013. **25**(26): p. 3549-3553.
190. Petros, R.A. and J.M. DeSimone, *Strategies in the design of nanoparticles for therapeutic applications.* Nature Reviews Drug Discovery, 2010. **9**(8): p. 615-627.
191. Oldenborg, P.-A., et al., *Role of CD47 as a marker of self on red blood cells.* Science, 2000. **288**(5473): p. 2051-2054.
192. Rodriguez, P.L., et al., *Minimal" Self" peptides that inhibit phagocytic clearance and enhance delivery of nanoparticles.* Science, 2013. **339**(6122): p. 971-975.
193. Brown, E.J. and W.A. Frazier, *Integrin-associated protein (CD47) and its ligands.* Trends Cell Biol, 2001. **11**(3): p. 130-5.

194. Wang, Y., et al., *Intravenous delivery of siRNA targeting CD47 effectively inhibits melanoma tumor growth and lung metastasis.* Molecular Therapy, 2013. **21**(10): p. 1919-1929.
195. Yoo, J.-W., E. Chambers, and S. Mitragotri, *Factors that control the circulation time of nanoparticles in blood: challenges, solutions and future prospects.* Current pharmaceutical design, 2010. **16**(21): p. 2298-2307.
196. Jain, R.K., *Determinants of tumor blood flow: a review.* Cancer Res, 1988. **48**(10): p. 2641-58.

Vita

Education

July 2009-Present JOHNS HOPKINS UNIVERSITY Baltimore, MD
Ph.D. - Materials Science and Engineering
Thesis: Synthesis of nanoparticles for quantitative evaluation of the enhanced permeability and retention (EPR) effect in vivo
GPA 3.87/4.0

May 2009 TEXAS A&M UNIVERSITY College Station, TX
M.S. - Mechanical Engineering
Thesis*: Antimicrobial activity of cationic antiseptics in Layer-by-Layer thin film assemblies*
GPA 3.812/4.0

May 2007 ROSE-HULMAN INSTITUTE OF TECHNOLOGY Terre Haute, IN
B.S. - Mechanical Engineering, *Summa Cum Laude*
Minors: Spanish, Language & Literature
GPA 3.92/4.0

Research Experience

Johns Hopkins University July 2009 – Present

- Evaluation of nanoparticles for delivery of drugs and imaging agents to solid tumors.
- Analysis of the effect of a tumor on the pharmacokinetics of liposomal doxorubicin.
- Performed a macro study of nanoparticles for targeting solid tumors in order to create a standardized protocol for nanoparticle comparison.
- Synthesis and characterization of nanoparticles including quantum dots and liposomes.
- Tailoring of nanoparticle surface by altering the charge, pegylation, and active groups for subsequent conjugation to various ligands for active tumor targeting.
- Research responsibilities include analysis of nanoparticle size, zeta potential, targeting efficacy both *in vitro* and targeting to solid tumors *in vivo*, including pharmacokinetic and biodistribution studies.

Texas A&M University August 2007 - June 2009

- Developed antimicrobial thin films to be used as a coating to improve sterility of medical devices, bandaging, and other products.
- Characterization of antimicrobial thin films prepared using layer-by-layer (LbL) assembly.
- Analysis of the effects of ionic strength, pH, and antimicrobial agents on inhibition against both gram-negative and gram-positive bacteria.

Los Alamos National Laboratory, Los Alamos, NM Summer 2007

- Worked in a larger team investigating a novel AuZn alloy.
- Mechanical characterization and analysis with tensile testing and other methods.

NASA-John Glenn Research Center, Cleveland, OH Summers 2004-2006

- 2006: Modeling of foam cells used in shuttle missions.
- 2006: Failure analysis via optical and electron microscopy.
- 2004-2005: Mechanical testing of polymers composites.

Awards and Honors

- MVP for leadership role in Thread, a local nonprofit, *2014*
- Donald S. Rodbell Memorial Graduate Research Fellowship in Materials Science and Engineering, *2011-present*
- National Science Foundation (NSF) Graduate Research Fellowship, *2008-2011*
- Texas A&M University Graduate Diversity Fellowship Recipient *August 2007 – 2009*
- Steinhauser award for the top mechanical engineering sophomore, *2005.*

Leadership Activities

Thread (formerly Incentive Mentoring Program)

- Program Coordinator: Support project managers as they lead teams to build up a "family" of mentors to a struggling high school student.
- Work with the site director and project managers to develop project plans and timelines.
- Develop new and current leaders and supports division morale.

Johns Hopkins University

- Organized, hosted, and led a symposium for scientific presentations and discussions, *2014*.
- Led laboratory graduate level courses in synthesis of gold nanoparticles.
- Planned and conducted summer workshops for high school teachers on nanoparticle synthesis and applications.
- Planned, organized, and operated an exhibit on the National Mall for the USA Science and Engineering Festival, *2010*.

Texas A&M University

- Led laboratories and grading for a junior level materials and manufacturing course and grading for a senior level polymer properties course.

Rose-Hulman Institute of Technology

- Learning Center. Responsibilities included tutoring and preparing review packets for finals. Beginning September 2006, responsibilities also included supervision.
- Served as the student representative on the ethics committee where I helped draft amendments to Rose-Hulman's Institute Policies, Rules and Regulations.

Publications

1. **Dawidczyk, C.M.**; Russell, L.M.; Searson, P.C. Nanomedicines for cancer therapy: state-of-the-art and limitations to pre-clinical studies that hinder future developments. *Front. Chem.* **2014**, *2*, 1-13.
2. **Dawidczyk, C.M.**; Kim, C.; Park, J.H.; Russell, L.M.; Lee, K.H.; Pomper, M.G.; Searson, P.C. State-of-the-art in design rules for drug delivery platforms: lessons learned from FDA-approved nanomedicines. *J Control Release.* **2014**. *187,* 133-144.
3. Lee, K.H.; Galloway, J.F.; Park, J.; **Dvoracek, C.M.**; Dallas, M.; Konstantopoulos, K.; Maitra, A.; Searson, P.C. Quantitative molecular profiling and multiplexing of biomarkers for cancer with functionalized quantum dots. *Nanomed.-Nanotech. Bio. and Med.* **2012**, *8,* 1043-1051.
4. Galloway, J.; Winter, A.; Lee, K.H.; Park, J.; **Dvoracek, C.M.**; Devreotes, P.; Searson, P.C. Quantitative characterization of the lipid encapsulation of quantum dots for biomedical applications. *Nanomed.-Nanotech. Bio. and Med.* **2012**, *8,* 1190-1199.
5. Park, J.; **Dvoracek, C.M.;** Lee, K.H.; Galloway, J.F.; Bhang, H.C.; Pomper, M.G. Searson, P.C.CuInSe/ZnS core/shell NIR-quantum dots for biomedical imaging. *Small*, **2011**, *7*, 3148-3152.
6. **Dvoracek, C.M;** Sukhonosova, G.; Benedik, M.J.; and Grunlan, J.C. Antimicrobial behavior of polyelectrolyte-surfactant thin film assemblies. Langmuir, **2009**, *25*, 10322-10328.